The Thesis Committee for Can Ceyhan
Certifies that this is the approved version of the following thesis:

Interplay of Salt-Influenced Structural Deformation and Submarine Channel Evolution in the Campos Basin, Offshore Brazil

APPROVED BY
SUPERVISING COMMITTEE:

Supervisor: _____
William L. Fisher

Co-supervisor: _____
Jacob A. Covault

_____
David Mohrig

_____
Michael R. Hudec

Interplay of Salt-Influenced Structural Deformation and Submarine Channel Evolution in the Campos Basin, Offshore Brazil

by

Can Ceyhan, B.S.

Thesis

Presented to the Faculty of the Graduate School of

The University of Texas at Austin

in Partial Fulfillment

of the Requirements

for the Degree of

Master of Science in Geological Sciences

The University of Texas at Austin

August 2017

To my beloved family…

Acknowledgements

The 3D seismic-reflection dataset used herein was provided by PGS Investigação Petrolífera Limitada. The PGS logo is placed on all illustrations derived from this dataset. Interpretations are mine unless indicated otherwise. Landmark provided the Decision Space and Geoprobe software for the 3D seismic interpretation. I express my gratitude to both organizations.

I would like to express my deepest gratitude to my supervisors, Dr. William Fisher and Dr. Jacob Covault, for their thoughtful guidance and support throughout my research. It has been a great honor to work with them. My gratitude also goes to my committee members, Dr. David Mohrig and Dr. Michael Hudec.

I am very thankful to Dr. Zoltan Sylvester for our discussions and his valuable suggestions.

I cannot thank enough Dallas Dunlap, for his support, encouragement and endless patience.

I also thank Dr. Daniel Carruthers for providing his previous interpretations of the same dataset that I used for my research.

This research was accomplished with assistance from the Turkish Petroleum Corporation. I thank them for providing my scholarship, and for sponsoring my graduate study at the University of Texas at Austin.

Last but not least, I thank my wife, Ecenur Ceyhan, for her valuable support, patience, and love, both as a colleague and as a life partner. I would also like to thank my family members for their endless support during my research.

Abstract

Interplay of Salt-Influenced Structural Deformation and Submarine Channel Evolution in the Campos Basin, Offshore Brazil

Can Ceyhan, MSGeoSci

The University of Texas at Austin, 2017

Supervisors: William L. Fisher, Jacob A. Covault

The Campos Basin, located on the southeastern Brazil passive margin, is one of the most productive basins in the western South Atlantic. The development of many siliciclastic turbidite reservoirs in the southeastern Brazilian margin provided a great interest in submarine channel systems of the Campos Basin for hydrocarbon exploration purposes. Prior research highlights the variation of sediment supply, sea-level fluctuations and tectonic activity as the most critical controls on channel development within the Campos Basin. The Campos Basin is structurally complex as a result of salt movement, and it is an ideal setting in which to investigate the influences of structural deformation on channel evolution and architecture.

I investigated the interaction between development of a post-Miocene submarine channel system and structural deformation related to salt tectonics by using structural and stratigraphic analysis of 3D seismic-reflection data, which covers an area of approximately 1750 km^2. I produced detailed maps and cross sections of the submarine channel system, and compared them to structural maps in order to interpret the control of

structural deformation on evolution and architecture of the submarine channel system. I interpreted that a regionally mapped seismic-reflection horizon approximates the paleobathymetry at the time of channel formation and correlated with the trend of the channel system. The paleobathymetry mainly dictated the transport pathway of the submarine channel system, as channels within the system mainly stayed in salt-withdrawal basins and avoided salt-influenced structural highs. However, the submarine channel system was diverted to flow directly on the top of a salt diapir within the southeastern part of the study area, rather than staying within salt-withdrawal basins. I explained this anomaly by two uplift stages of the salt diapir. Aggradation smoothed out much of the paleobathymetry associated with the first growth stage of the salt diapir, and the salt-influenced structural high was not able to divert the submarine channel system. The basal surfaces of channels within the system are deformed as a result of the growth of the salt diapir, which suggests that the salt diapir became active again when the submarine channel system started to develop.

Table of Contents

List of Figures

CHAPTER 1. INTRODUCTION

Geologic Overview of the Campos Basin

The Campos Basin is located on the southeastern Brazil passive margin. It lies beneath the coastal plain, continental shelf and slope of the southwestern portion of the South Atlantic Ocean (Bruhn et al., 2003).

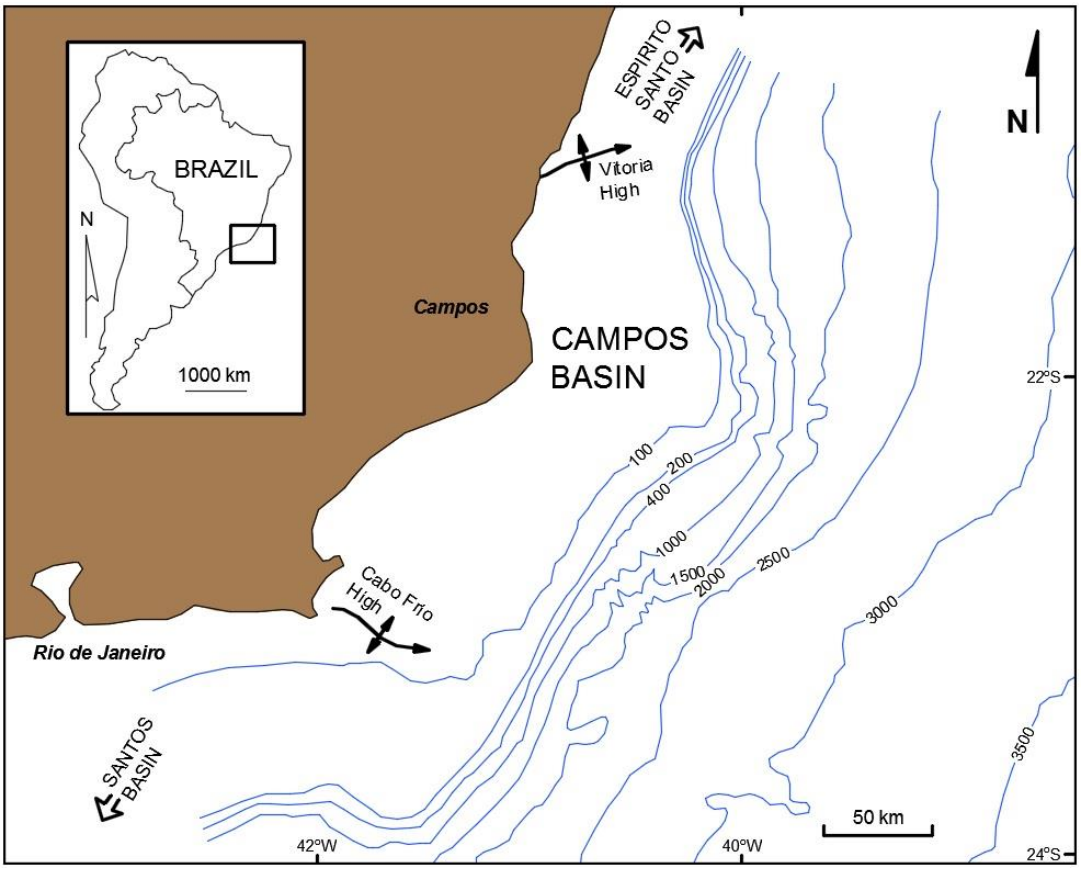

Figure 1: Location map of the Campos Basin (modified from Peres, 1993).

The basin is located between the geographic parallels of 21°S and 24°S, and extends roughly from 15 km inland to the 3400 m isobath (Rangel et al., 2003). More than 70% of the basin is at water depths greater than 200 m (Carminatti & Scarton, 1991).

The Campos Basin is separated from adjacent basins by basement highs that strike transverse to the continental margin. It is separated from the Espírito Santo Basin to the north by the Vitoria high, and from the Santos Basin to the south by the Cabo Frio high (Figure 1) (Guardado et al., 2000).

TECTONO-STRATIGRAPHIC EVOLUTION OF THE CAMPOS BASIN

The tectono-stratigraphic evolution of the Campos Basin was initiated during the late Jurassic breakup of Gondwana and subsequent opening of the South Atlantic Ocean (Guardado et al., 1990). Considering different tectonosedimentary stages of basin evolution, Bruhn (1998) subdivided the sedimentary fill of the Campos Basin into five megasequences, which are, from oldest to youngest: a continental rift megasequence, a transitional evaporitic megasequence, a shallow carbonate platform megasequence, a marine transgressive megasequence, and a marine regressive megasequence (Figure 2 & Figure 3). A megasequence is a lithostratigraphic sequence that covers a complete marine transgressive or regressive cycle (Sloss, 1964).

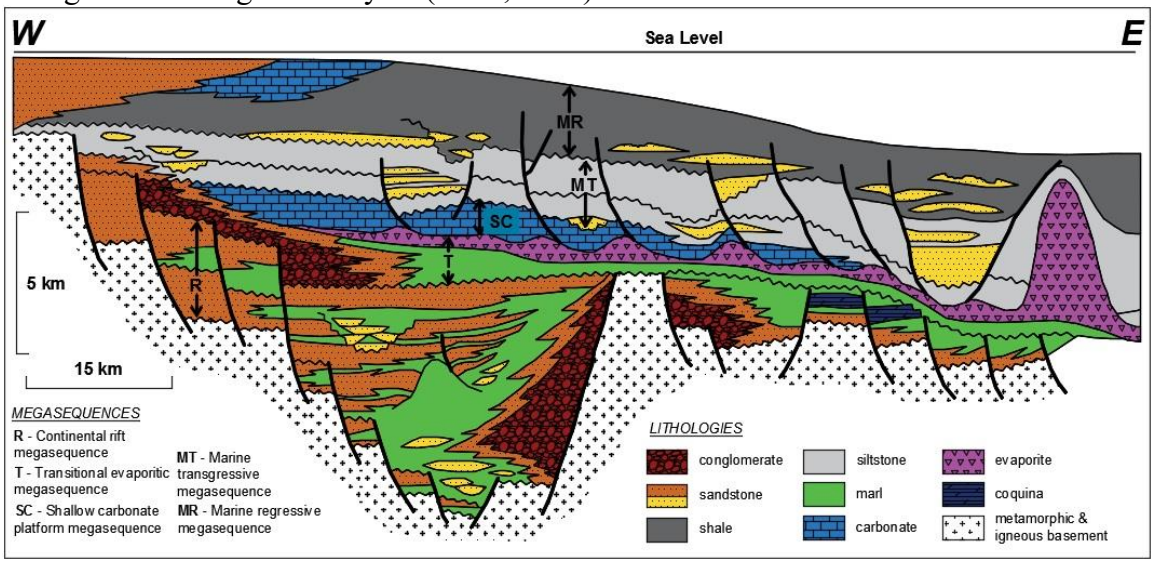

Figure 2: Principal stratigraphic units of the Campos Basin (modified from Bruhn, 1998).

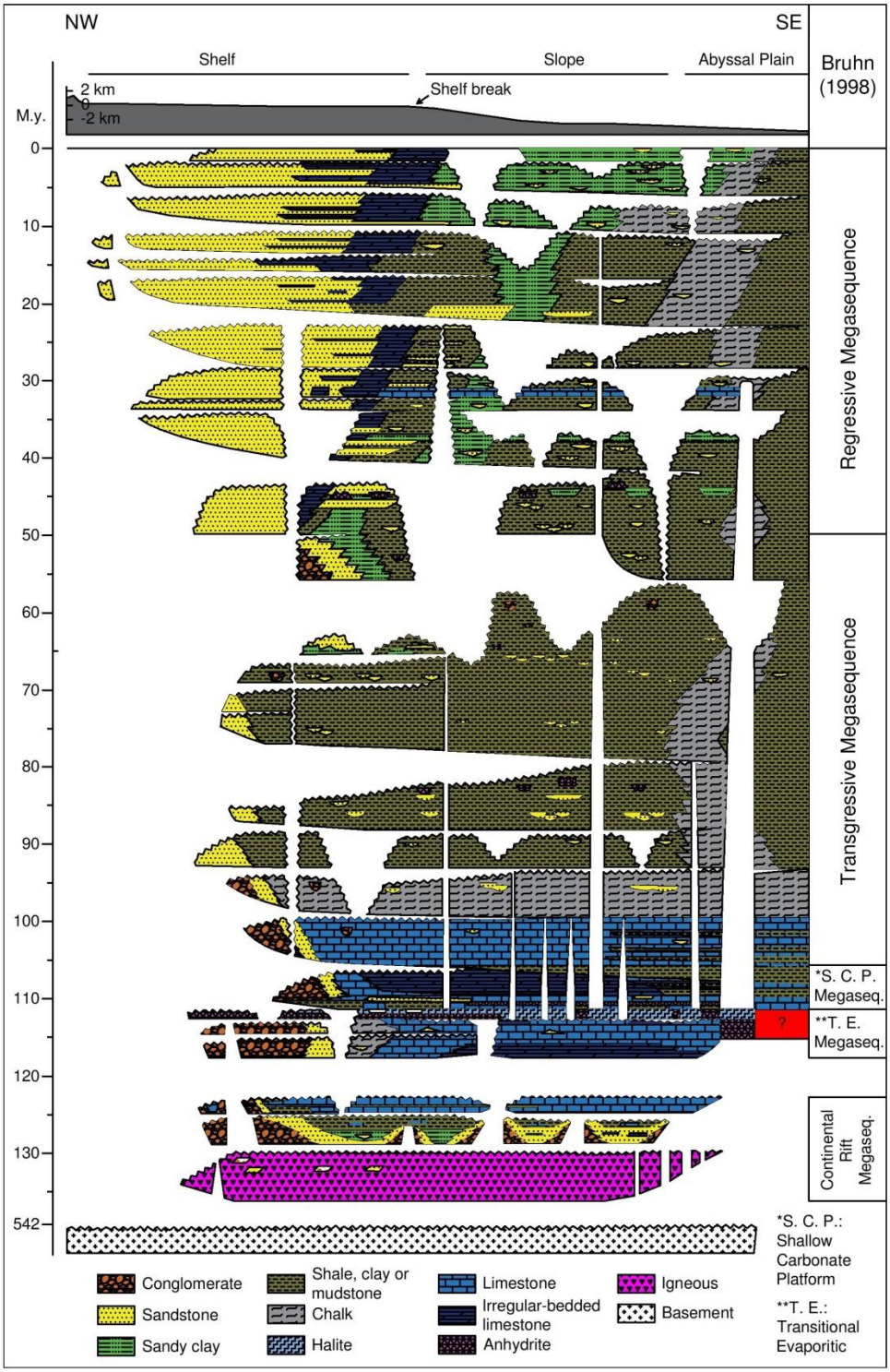

Figure 3: Stratigraphic chart of the Campos Basin (modified from De Gasperi & Catuneanu, 2014, who modified from Winter et al., 2007).

The continental rift megasequence is characterized by fault-related subsidence as a result of the continental crust stretching that preceded the emplacement of oceanic crust (Bruhn, 1998). This succession has diversity in facies, which range from siliciclastic sediments to lacustrine coquinas and volcanic rocks (Bruhn, 1998). It records the lacustrine and fluvial-deltaic environments formed within rift valleys from the Neocomian to the early Aptian (Winter et al., 2007).

The transitional evaporitic megasequence accumulated during the middle Aptian to the early Albian in a transitional marine and nonmarine environment (Bruhn, 1998). It includes basal siliciclastic deposits and microbial limestones, overlain by evaporites. This evaporite succession played an important role in shaping the architecture of the Campos Basin, as the salt movement molded the seafloor. The stratigraphic architecture of this megasequence is dominated by horizontal layering, and is different from the stratigraphic and structural architecture of the underlying unit that is dominantly characterized by tilted blocks (Bruhn, 1998). These two megasequences are separated by an angular unconformity (Guardado et al., 1990).

The shallow carbonate platform megasequence was deposited during the early to the middle Albian, and it marks the establishment of fully marine conditions across the basin (Bruhn, 1998). During the deposition of this megasequence, the regional eastward tilting of the basin induced the downslope gliding of the underlying evaporites (Bruhn, 1998). The carbonate deposits of this succession have a gradational contact with the evaporites of the previous megasequence (Winter et al., 2007).

The marine transgressive megasequence lasts from the late Albian to the middle Eocene and represents progressively deeper water facies, from calcilutites to marls, shales, and turbidites (Bruhn, 1998). This succession marks the progressive drowning of the shallow carbonate platform (Bruhn, 1998).

The marine regressive megasequence accumulated from the middle Eocene to the Holocene and represents a variety of continental, shallow-marine siliciclastic and carbonate environments, and deep-water depositional environments (Bruhn, 1998). This unit records a general transition in depositional trend, from retrogradational to progradational (De Gasperi & Catuneanu, 2014).

Like the most prolific sedimentary basins in South America, North America, Europe and Africa, the Campos Basin is rich in salt and sedimentation interaction (Mohriak et al., 2012). The overall structural style of the basin is characterized by a detachment surface at the base of Aptian salt (Fetter, 2009). Below the detachment, the main structural features in the basement are horsts and grabens limited by steep normal faults active during the rift phase in the early Cretaceous (Chang et al., 1992). Following the opening of the South Atlantic Ocean during the early Albian, the Campos Basin tilted to the east and the formation of the divergent continental margin resulted in salt movement (De Gasperi & Catuneanu, 2014). Above the Aptian detachment, salt tectonics with extensional and compressional domains has been active since the Albian (Demercian et al., 1993). The salt tectonic domains within the Campos Basin are mainly controlled by the basement structure, with an upslope domain of horizontal extension to the west including extensional diapirs, an extensional to compressional intermediate domain of downhill translation with shortened salt diapirs, and a downslope domain of strong horizontal contraction to the east with thrusts and folds (Figure 4) (Mohriak et al., 2012).

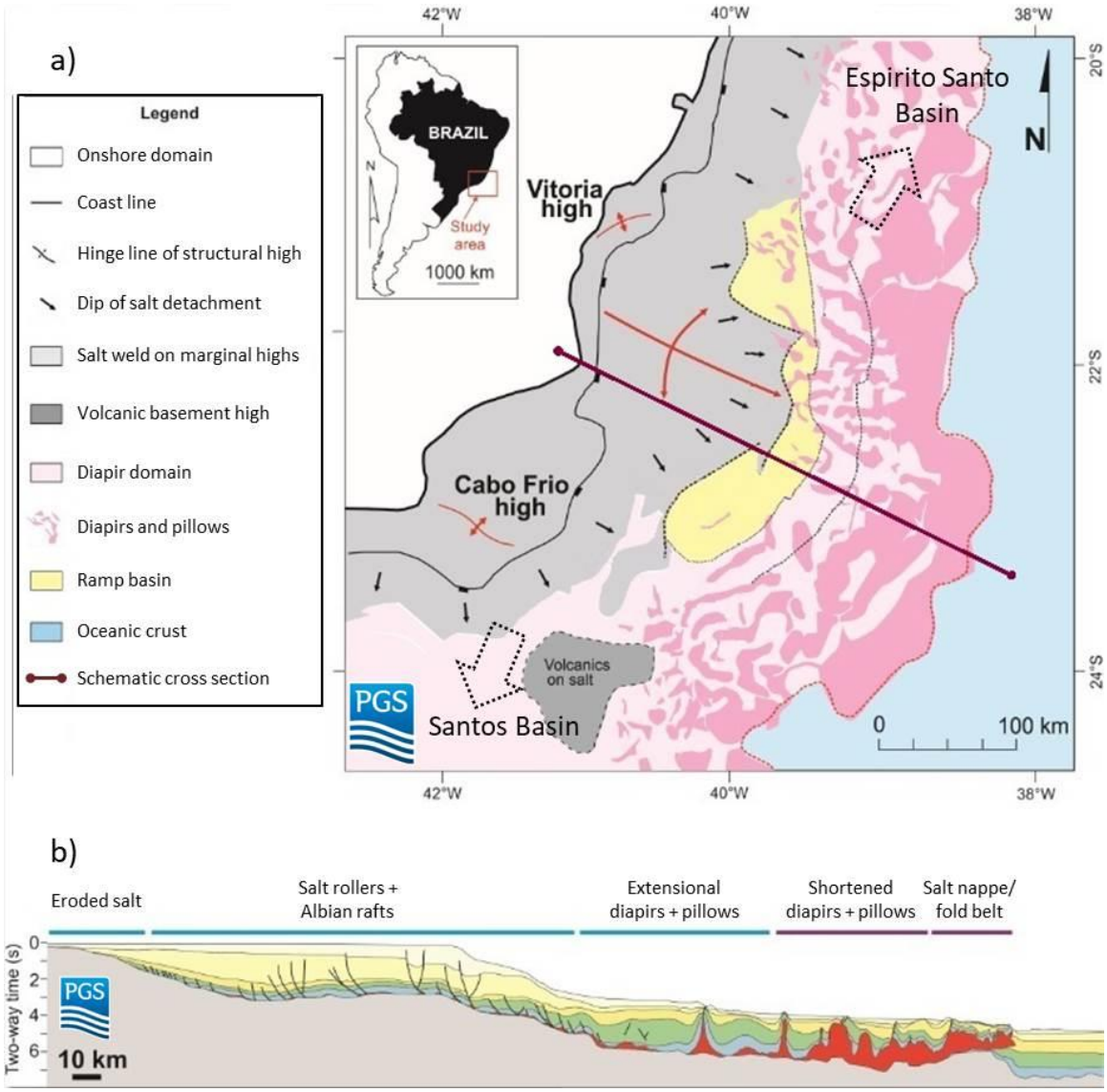

Figure 4: (a) Structural map, (b) schematic cross section of the Campos Basin (courtesy of Dr. Daniel Carruthers).

PETROLEUM SYSTEMS OF THE CAMPOS BASIN

The Campos Basin is one of the most productive hydrocarbon-bearing basins in the South Atlantic (Mohriak et al., 1990). Approximately 85% of the total Brazilian oil and natural gas production is provided from its reservoirs (Guardado et al., 2000). As of May 2017, total daily production in the Campos Basin was 1.3 million barrels of oil and 25 million cubic meters of natural gas (Palmigiani, 2017). Offshore oilfields of the Campos Basin under water depths between 80 m and 2400 m produce from a variety of reservoirs, including Neocomian fractured basalts, Barremian porous bioclastic limestones (coquinas), early to middle Albian calcarenites and calcirudites, and late Albian to early Miocene siliciclastic turbidites (Figure 5) (Mohriak et al., 1990).

Two source rock systems are present in the Campos Basin, which are lower Neocomian black shales and marls deposited in a lacustrine environment ranging from brackish to hypersaline water, and an upper Neocomian system comprising mainly calcareous black shales and marls deposited in lacustrine saline water environment of alkaline affinities (Barros, 1980). Petroleum generation began in Santonian-Coniacian time, reached its peak during the late Miocene and continues until the present day (Guardado et al., 2000). Hydrocarbon accumulations within the Campos Basin have both structural and stratigraphic controls, and they are associated with migration through normal faults and regional unconformities in the evaporitic layers (Mohriak et al., 1990). All essential processes and petroleum system elements have resulted in one of the most prolific hydrocarbon provinces within the western South Atlantic sedimentary basin system.

Siliciclastic turbidites are by far the most prolific reservoir rocks of the Campos Basin (Bacoccoli & Toffoli, 1988; Bruhn et al., 2003). Oil accumulations in turbidite reservoirs mainly have a structural control by listric normal faults, which are soling out

on underlying Aptian evaporites or are attached to the Precambrian basement (Bruhn et al., 2003). These faults may also provided pathways for oil migration from underlying rift-phase Neocomian source rocks (Bruhn et al., 2003). Most of the turbidite oilfields also have some degree of stratigraphic control, either by reservoir pinchout and/or partial reservoir erosion by younger, mud-filled channels (Bruhn et al., 2003).

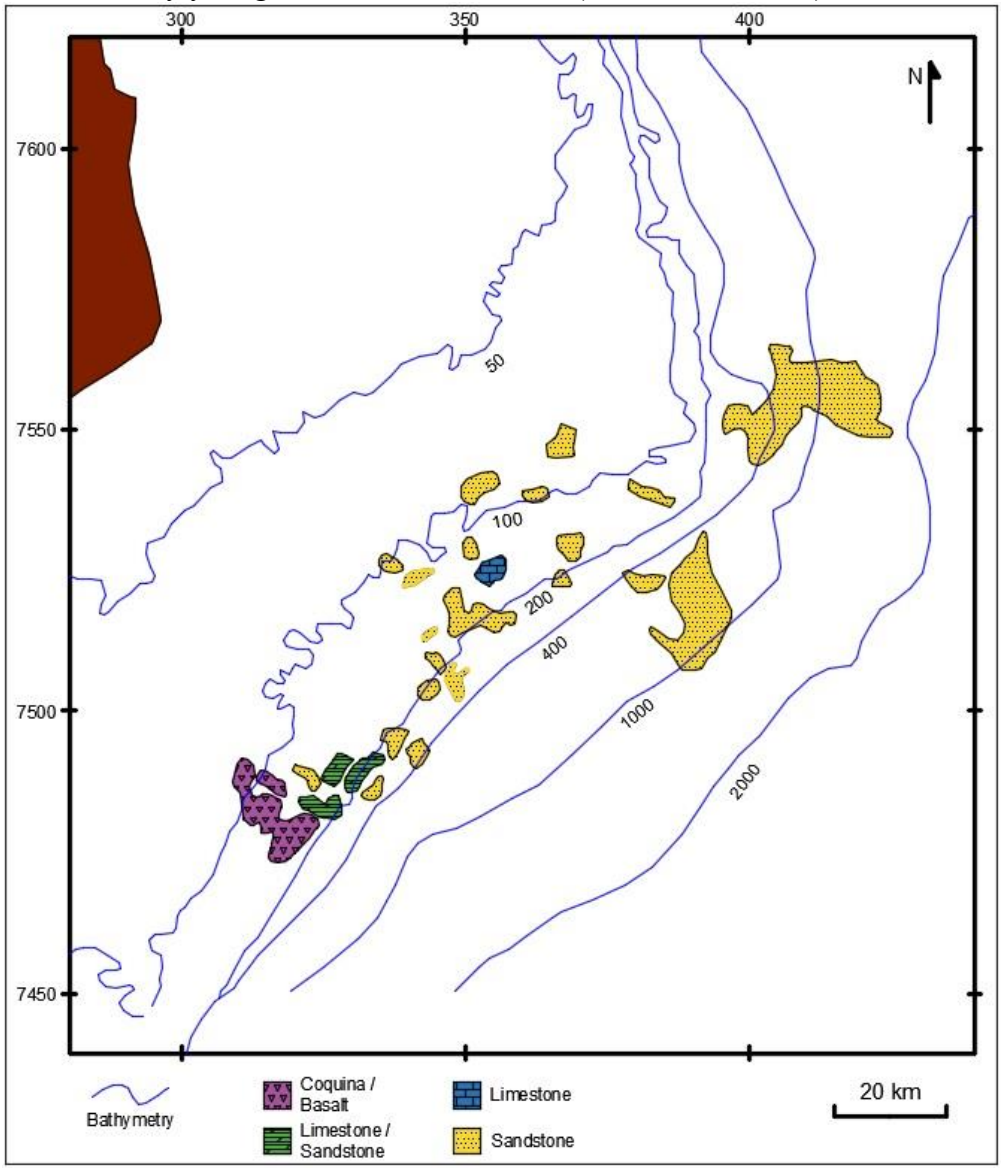

Figure 5: Reservoir types of the main hydrocarbon accumulations in the Campos Basin (modified from Mohriak et al., 1990).

Objective

Many hydrocarbon-bearing basins in the world are associated with salt tectonics (e.g., Gulf of Mexico, North Sea, Saudi Arabia, Iran, Iraq and Angola), and numerous studies focused on their tectono-stratigraphic evolution (e.g., Rowan & Weimer, 1998; Anderson et al., 2000; Broucke et al., 2004; Smith, 2004; Rowan & Vendeville, 2006). Sedimentological studies of the control of salt-influenced topography on submarine sediment gravity flow deposits have interpreted that structural deformation can control the location, pathway and architecture of channel, lobe and levee deposits (e.g., Rowan & Weimer, 1998; Anderson et al., 2000; Broucke et al., 2004; Huyghe et al., 2004; Smith, 2004; Gee & Gawthorpe, 2007; Mayall et al., 2010; Clark & Cartwright, 2011; Gamboa et al., 2012; Oluboyo et al., 2013). Sediment gravity flow is a general term for a sediment-water mixture in which the sediment component pulls interstitial water downslope by gravity (Middleton & Hampton, 1973).

As described in previous sections, an Aptian salt succession accumulated in the Campos Basin. The overall structural style of the basin is a result of salt movement (Fetter, 2009). The basin is structurally complex, including salt diapirs, salt-withdrawal basins between them and numerous listric normal faults detaching on the Aptian salt (Fetter, 2009).

The Campos Basin is one of the most prolific hydrocarbon-bearing basins in the South Atlantic, and sand-rich turbidite systems are the most productive reservoirs rocks within the basin (Bacoccoli & Toffoli, 1988). A turbidite system is defined as a body of genetically related mass-flow sediments deposited in stratigraphic continuity (Mutti & Normark, 1987). Submarine channels are one of the primary erosional and/or depositional elements within turbidite systems (Mutti & Normark, 1987, 1991; Normark

et al., 1993; Piper & Normark, 2001). A channel is defined as the expression of negative relief produced by turbidity current flow, and represents a major, long-term pathway for sediment transport (Mutti & Normark, 1987). Channels can reach up to a kilometer in erosional depth and 10 kilometers in width (Mutti & Normark, 1987). Understanding the controls on submarine channel evolution is crucial for establishing a model for the development of turbidite systems (e.g., Mayall et al., 2006). Existing deep-water depositional models explaining the development and evolution of submarine channels within the Campos Basin are focused on the controls of sediment supply, relative sea-level fluctuations and tectonic activity (e.g., Mohriak et al., 1990; Peres, 1993; Bruhn & Walker, 1995; Rangel et al., 2003; Fetter et al., 2009; Albertâo et al., 2011; De Gasperi & Catuneanu, 2014). The basic framework for the development of submarine channel systems within the Campos Basin is represented as starting with deposition of a large volume of clastics during the buildup of a delta that constructs a thick, wide shelf sedimentary unit (Peres, 1993; Albertâo et al., 2011; De Gasperi & Catuneanu, 2014). This shelf sedimentary unit forms the main source of sediment for the deep-water turbidite system (Peres, 1993; Albertâo et al., 2011; De Gasperi & Catuneanu, 2014). Localized tectonic pulses (for example, salt tectonics) deform the outer shelf, leading to sediment failure and triggering sediment gravity flows (Peres, 1993; Fetter et al., 2009; De Gasperi & Catuneanu, 2014). Falls of relative sea-level result in the subaerial exposure of shelf sediments, which causes downcutting and erosion of shelf by rivers draining out to the receding shoreline, and reworking in a shallow, high-energy marine environment (Mohriak et al., 1990; Peres, 1993; Bruhn & Walker, 1995; Rangel et al., 2003; De Gasperi & Catuneanu, 2014).

Despite the extensive literature about the mechanisms controlling the development and evolution of submarine channel systems within the Campos Basin, few

studies are focused on the influence of salt-induced structural deformation on submarine channel system evolution. Submarine channels may be confined, diverted, deflected or blocked by the salt-cored growth of folds and diapirs within compressional and diapiric settings (Rowan & Weimer, 1998; Clark & Cartwright, 2009; Mayall et al., 2010; Oluboyo et al., 2013). The main purpose of this study is to demonstrate the relationship between salt-influenced structural deformation and submarine channel evolution within the Campos Basin.

Methodology

This study is based on a dataset, comprising a Kirchoff post-stack depth migrated 3D seismic-reflection volume. It is a mixed phase data covering an area of approximately 1750 km^2, to a depth of 9 km. Data were originally acquired in 2001 and reprocessed in 2011 by PGS Investigação Petrolífera Limitada. The 3D seismic-reflection volume has a bin spacing of 25 x 25 m, with a vertical sampling rate of 5 m. There are approximately 25 peaks along a vertical distance of 1000 m within the seismic dataset. Therefore, 3D seismic-reflection volume has a wavelength (λ) of 40 m, which results in a limit of separability ($\lambda/4$) of 10 m. Within the seismic images shown in this study, the black reflections correspond to positive amplitudes (peaks) whereas the white reflections represent negative amplitudes (troughs).

The study area is located in the central part of the Campos Basin, within the translational domain between compressional and extensional domains, and the middle slope portion of the basin (Figure 4). It is located between water depths of 1907 m and 2585 m (Figure 7). There are no well data within the study area to confirm lithology of seismic reflections and age. I used a previous interpretation by Dr. Daniel Carruthers (a former postdoctoral researcher at the Bureau of Economic Geology) on the same 3D

seismic-reflection dataset to determine the ages of every critical horizon within the study area (Figure 6). The software used to carry out the seismic interpretation was Landmark Decision Space and Geoprobe.

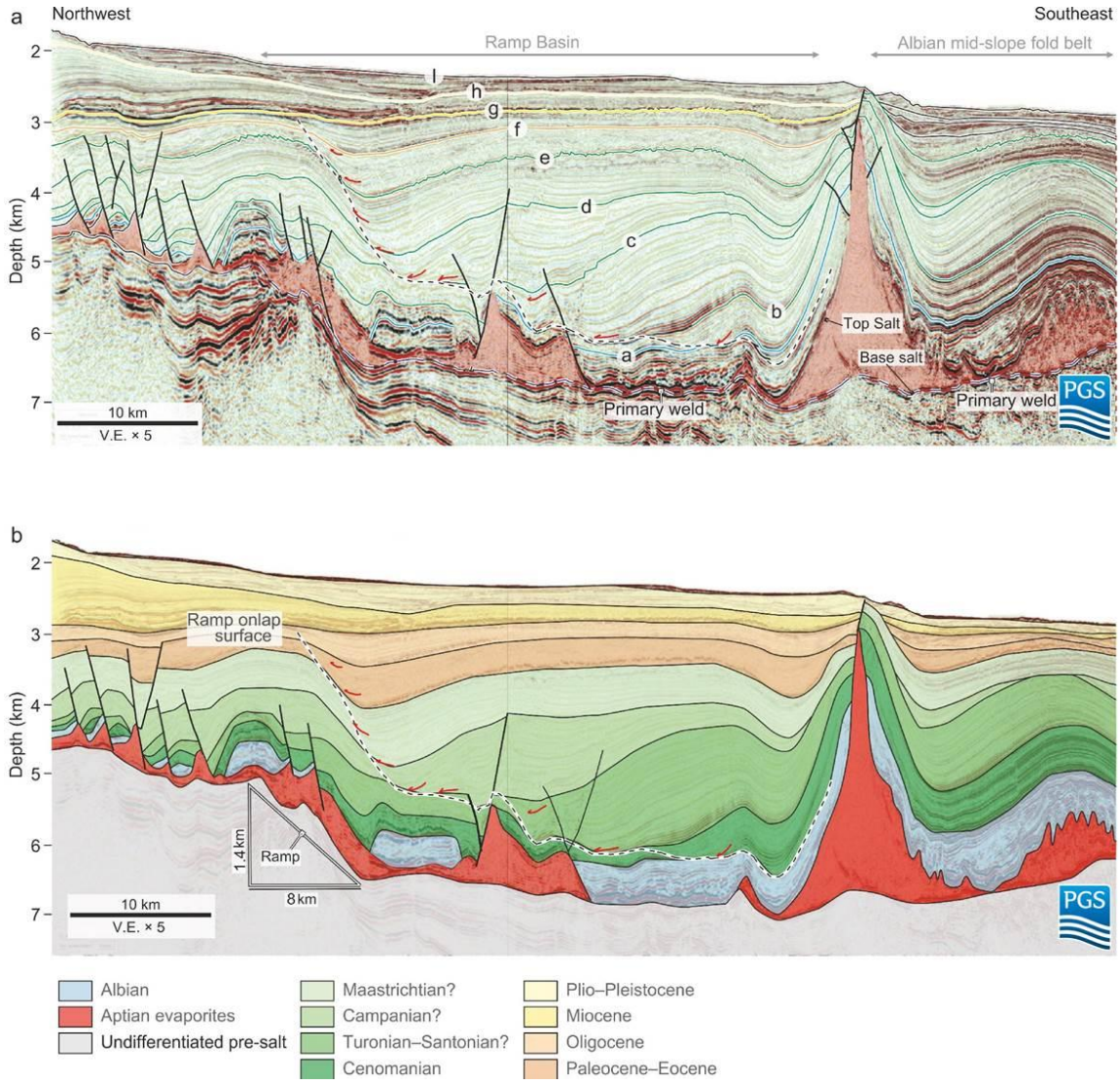

Figure 6: Previous interpretations of key horizons (courtesy of Dr. Daniel Carruthers).

I performed an integrated 3D analysis of structural geology and seismic stratigraphy to investigate the interaction between submarine channel evolution and salt-cored structural deformation. From the late Cretaceous to the Holocene, many submarine channel systems exist within the Campos Basin, sourced from various different points (Peres, 1993). I focused my analysis on a post-Miocene submarine channel system and investigated the structural control on each channel within the system in detail.

I interpreted the structural configuration of the study area by mapping the modern seafloor, the horizon representing a stratigraphic surface approximately coeval with the initiation of the submarine channel system and the top of the salt succession. I mapped channels within the system from the 3D seismic-reflection volume. I defined and interpreted seismic facies within the submarine channel system on the basis of the amplitude, continuity, and architecture of reflections (Mutti & Normark, 1987, 1991; Normark et al., 1993). I characterized each channel within the submarine channel system to document the response of channel pathway and architecture to salt diapirs, salt-withdrawal basins between them and salt-related slope topography.

CHAPTER 2. STRUCTURAL CONFIGURATION

Seafloor

The most striking features at the modern seafloor are structural highs over salt diapirs, the submarine channel system in the southeastern part of the study area, and WNW- and ENE-trending lineaments within the central part of the study area (Figure 7). I interpreted both these lineaments as active fault scarps, because a shallow horizontal slice at the depth of 2424 m (~100 m below the seafloor at the location where lineaments are observed) shows faults and fractures parallel to these lineaments (Figure 8).

Figure 9 is the map of a horizon that I interpret to represent a stratigraphic surface approximately contemporaneous with the formation of the submarine channel system, which is the basal surface of the oldest channel within the system. Like the modern seafloor, salt diapirs mainly shape the paleobathymetry of the submarine channel system, by forming structural reliefs on the seafloor (Figure 7 & Figure 9).

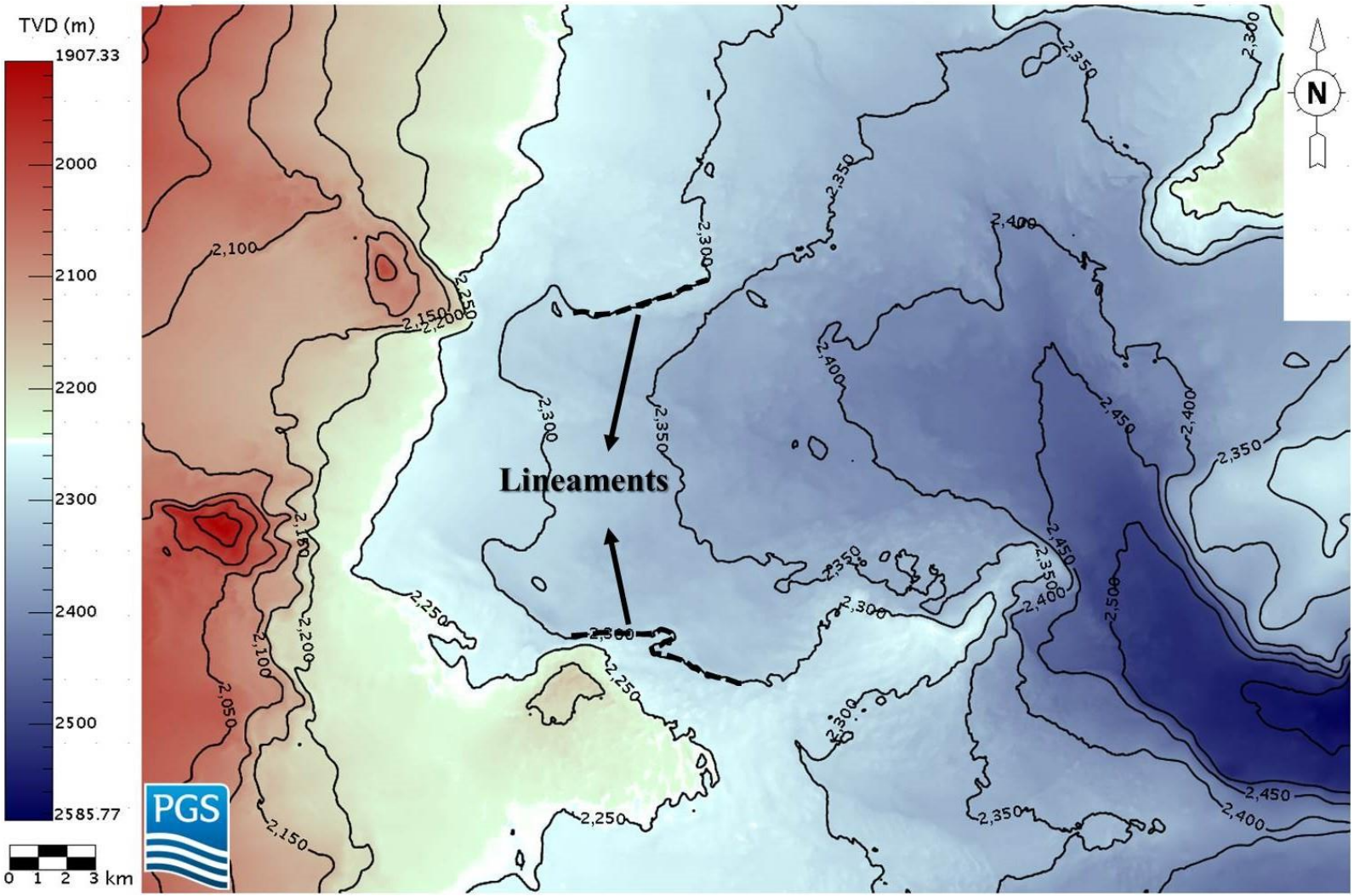

Figure 7: Structural map of the modern seafloor.

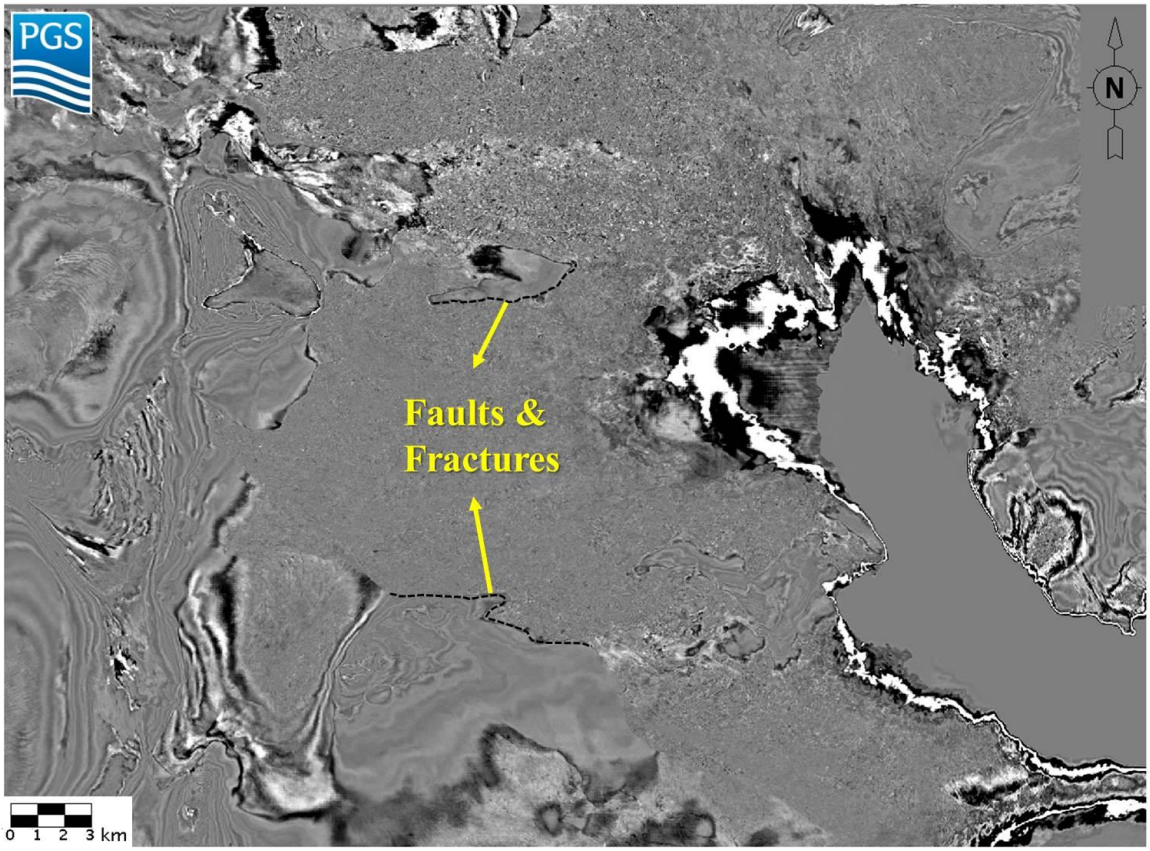

Figure 8: Horizontal slice at the depth of 2424 m showing faults and fractures parallel to the lineaments on the modern seafloor.

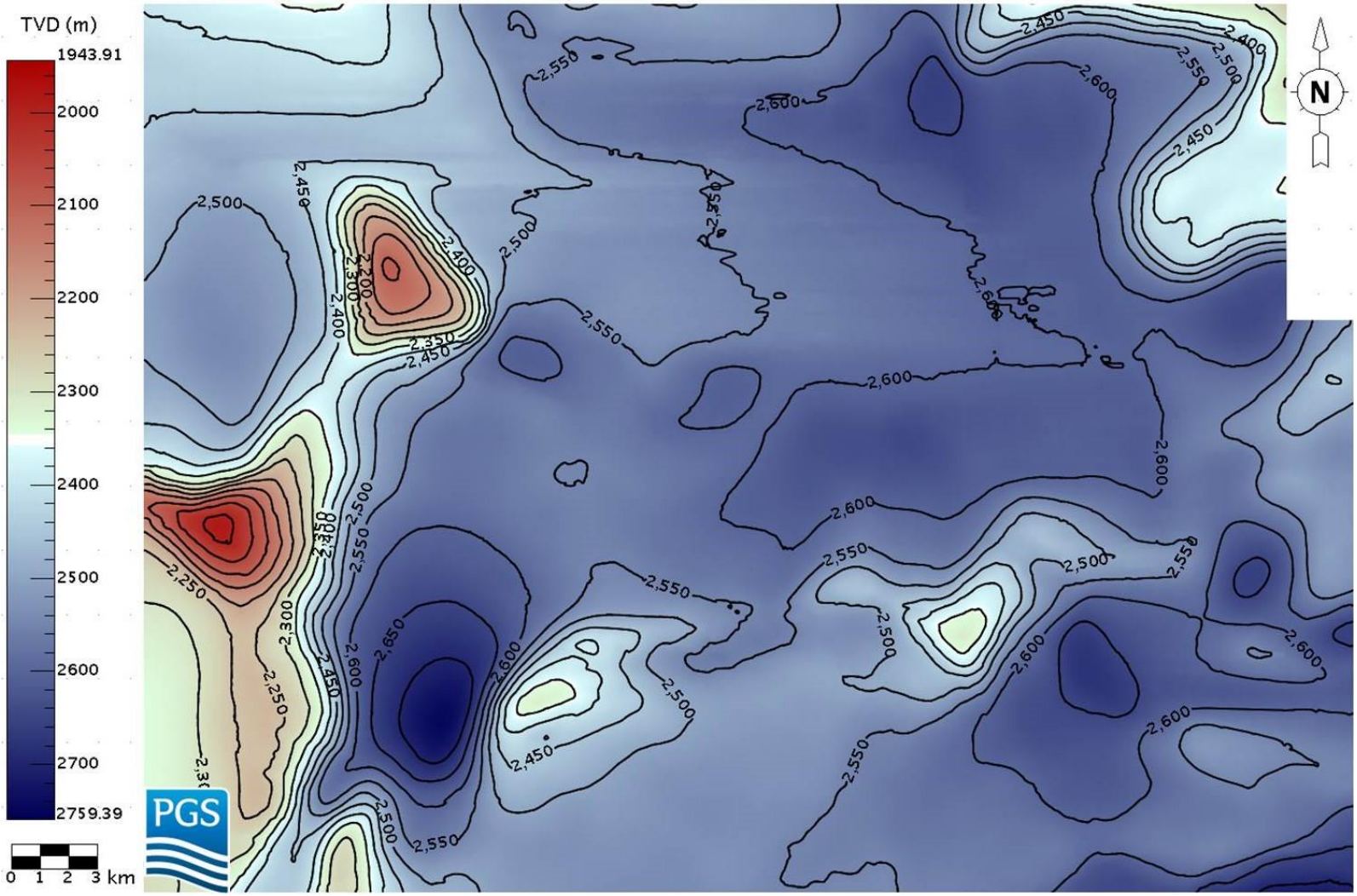

Figure 9: Structural map of the horizon representing a stratigraphic surface approximately coeval with the initiation of the submarine channel system.

Salt Unit

The overall structural configuration of the Campos Basin is a result of the movement of an Aptian evaporite unit (Fetter, 2009). The study area is within the translational domain, where both extensional and compressional structures can be observed (Figure 4). Salt deformation controls the structural configuration by salt diapirism and by creating salt-withdrawal basins between structural highs (Rowan & Weimer, 1998).

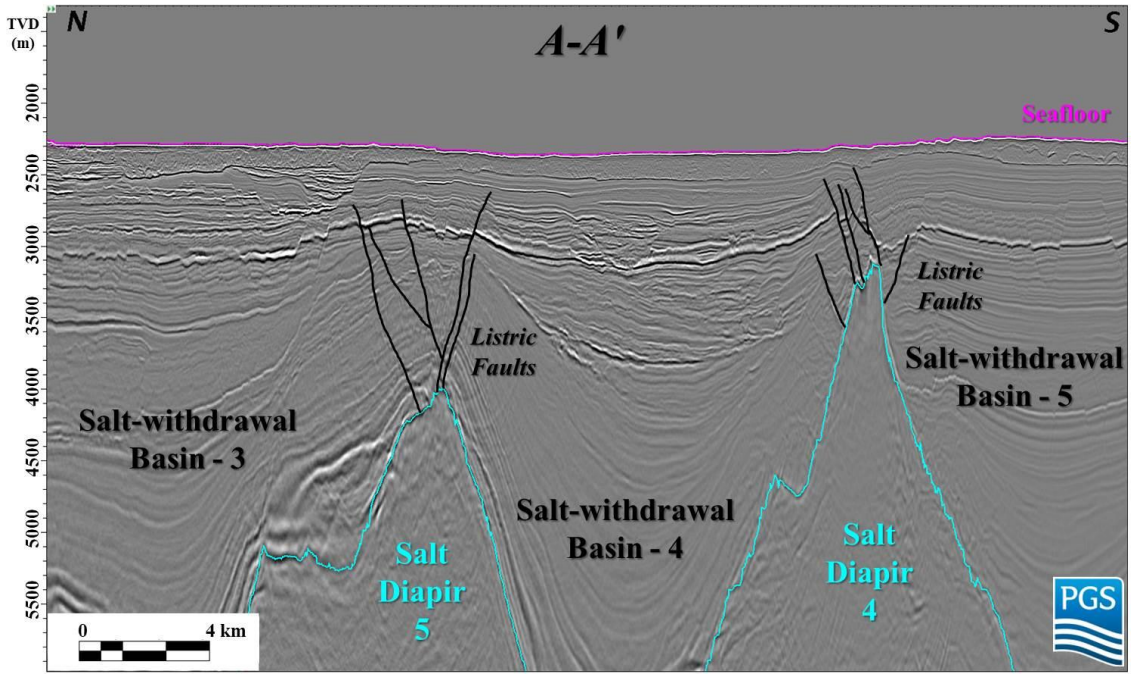

Figure 10: Seismic cross section A-A′ showing typical structures associated with salt movement. Location of the cross section is shown in Figure 11.

Evaporite units are associated with a high impedance contrast in contact with sedimentary deposits (Quirk et al., 2012). Consequently, I interpreted the top of the Aptian salt sequence as a horizon with high-amplitude reflection within the seismic-reflection dataset. My interpretation of the top of salt layer is also based on structures

typically associated with salt movement such as salt diapirs, salt-withdrawal basins, and listric faults that detach on the top of evaporite sequence (Figure 10) (Jackson & Talbot, 1991). A salt diapir is defined as a mass of salt that has flowed in a ductile manner and discordantly pierced or intruded the overburden (Jackson & Talbot, 1991). A salt-withdrawal basin is a depression formed by salt withdrawal from underneath the sediment wedge, where salt withdrawal is defined as mass transfer of salt over time without obvious change in salt area in cross section (Jackson & Talbot, 1991). A listric fault is a normal fault with a curving, concave-up fault plane whose dip decreases with depth (Jackson & Talbot, 1991). I used all these criteria to map the top of salt, where salt-withdrawal basins are represented with blue and structural highs are shown in red in the map of top salt in Figure 11. The top of salt map shows nine salt diapirs (SD-1 to 9) and eight salt-withdrawal basins (WB-1 to 8) between these structural highs. The diapirs are as much as 4800 m in height above the regional level of the Aptian salt layer (Figure 11), reaching to 300 m below the modern seafloor (Figure 12), where they have widths of as much as 5 km. Salt-withdrawal basins are typically 10 to 15 km wide and contain post-salt deposition of as much as 5100 m in thickness (Figure 12).

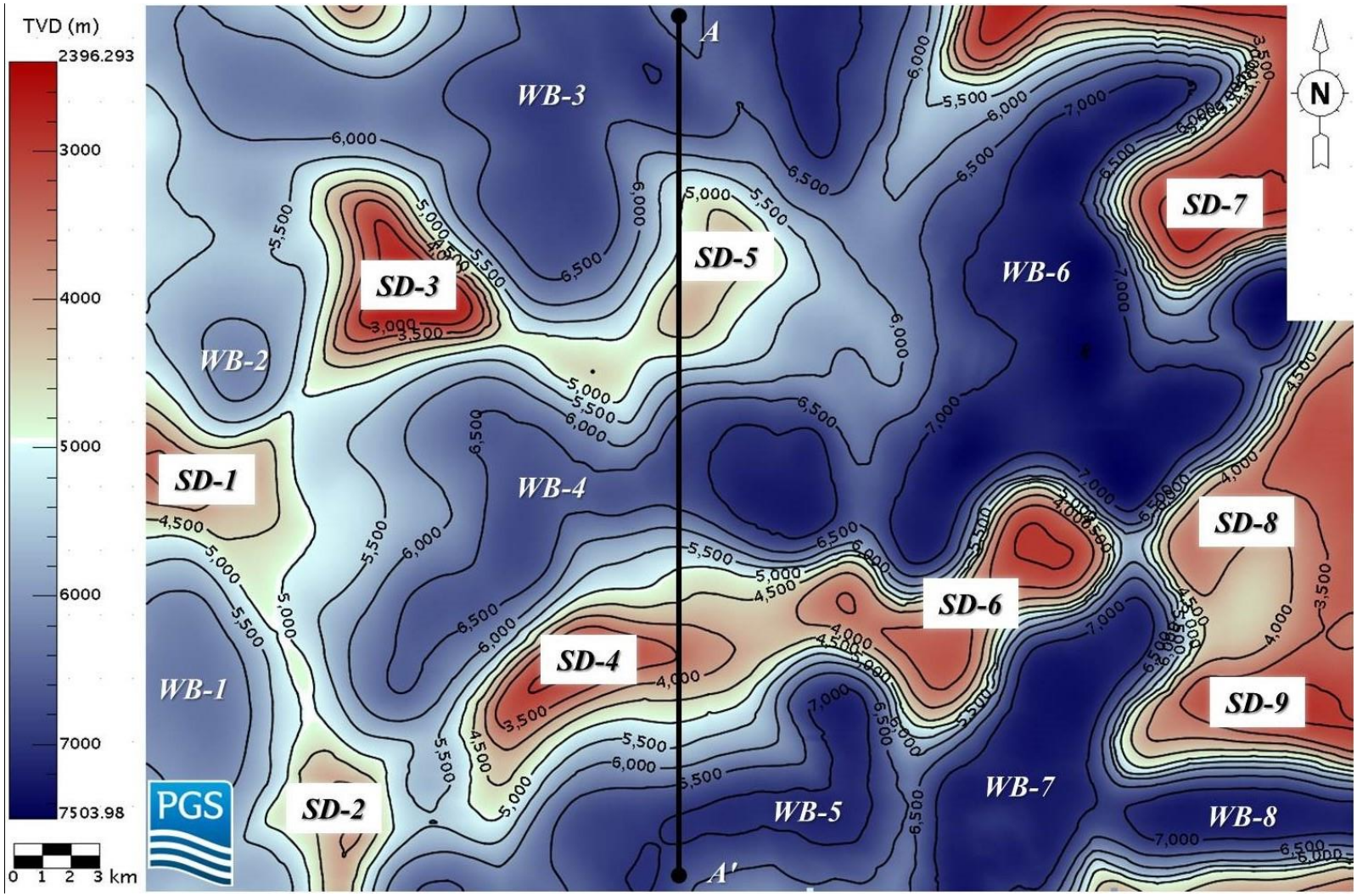

Figure 11: Structural map of the top of salt unit. Map also shows the location of seismic cross section A-A′.

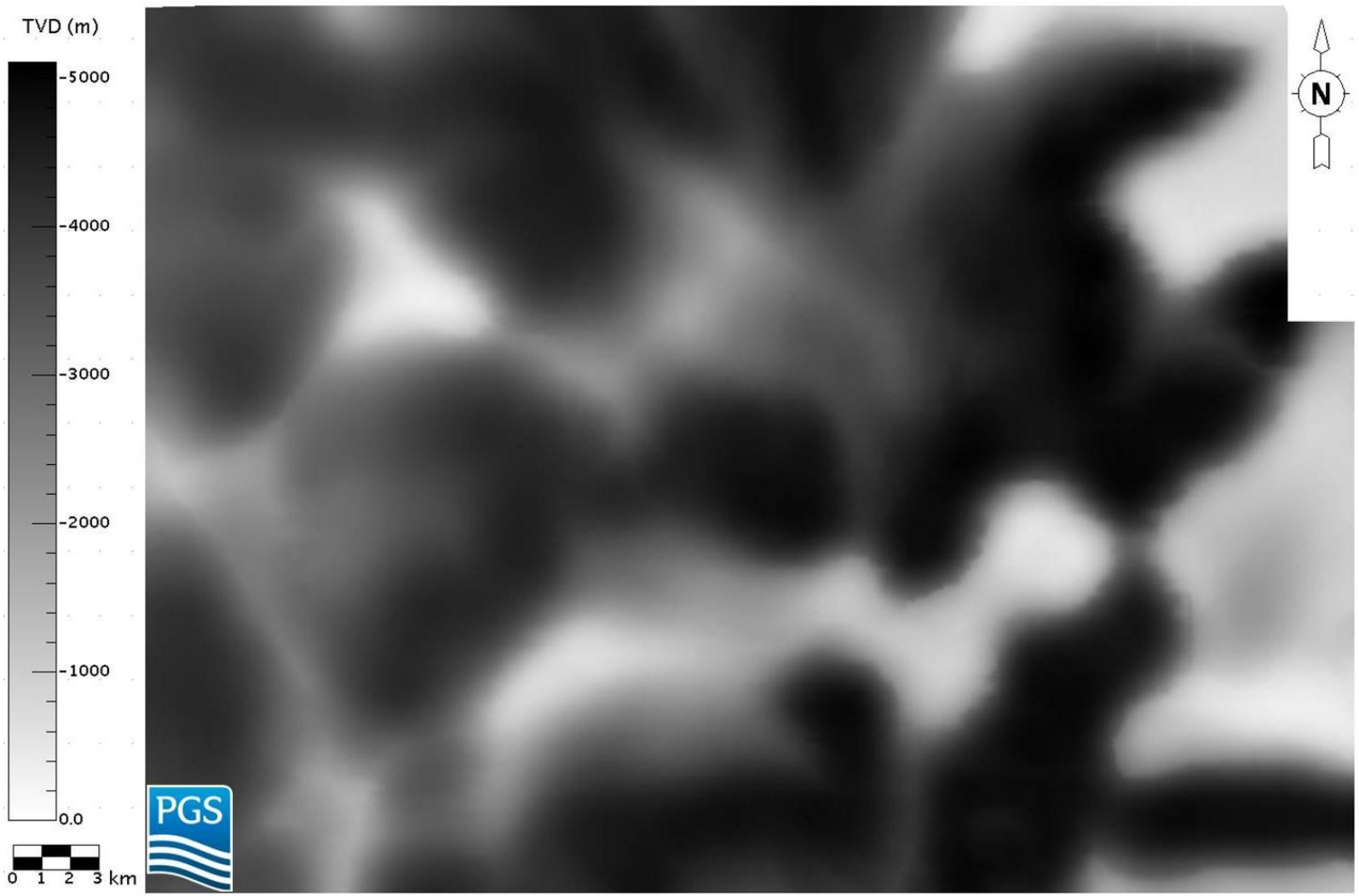

Figure 12: Isochore map of deposits on the top of salt unit.

Interaction Between Salt Diapirism and Bathymetry

Salt diapirism can complicate the topography of the seafloor (e.g., Rowan & Weimer, 1998; Anderson et al., 2000; Broucke et al., 2004; Huyghe et al., 2004; Smith, 2004; Gee & Gawthorpe, 2007; Hudec & Jackson, 2007; Mayall et al., 2010; Clark & Cartwright, 2011; Gamboa et al., 2012; Oluboyo et al., 2013). In order for buried salt to be emplaced into its overburden as a diapir, any rock previously occupying that space must be removed or displaced (Hudec & Jackson, 2007). Emplacement may occur by uplift of the overburden, which results in a positive bathymetric relief (Hudec & Jackson, 2007). Salt emplacement also creates salt-withdrawal basins between diapiric highs (Jackson & Talbot, 1991). Once the growth of a salt diapir is stopped, accommodation within salt-withdrawal basins will be filled and the bathymetric expression of the salt diapir will be smoothed out (Jackson & Talbot, 1991; Prather et al., 1998; Winker & Booth, 2000).

Salt diapirs mainly shape the modern seafloor and the paleobathymetry of the submarine channel system within the study area by creating structural reliefs (Figure 13 & Figure 14). However, both seafloor maps (Figure 7 & Figure 9) show a much smoother topography compared to the map of the top of salt unit (Figure 11), which indicates that paleobathymetric relief associated with salt diapirism is mainly smoothed out by aggradation.

In this study, I determined the timing of salt diapirism relative to the formation of the submarine channel system by investigating the architecture of nearby strata and interpreting pre-, syn- and post-kinematic sequences. Pre-kinematic sediments accumulated on a flat salt unit that has not flowed yet, so these sediments are characterized by uniform thickness and parallel strata that tilted toward the salt dome

(Jackson & Hudec, 2017). Syn-kinematic sediments were deposited during the movement of salt and characterized by strata that thin onto the salt diapir (Jackson & Hudec, 2017). Post-kinematic sediments were deposited after the end of salt flow and, because they are not affected by the movement of salt, they have uniform thickness across salt diapirs (Jackson & Hudec, 2017).

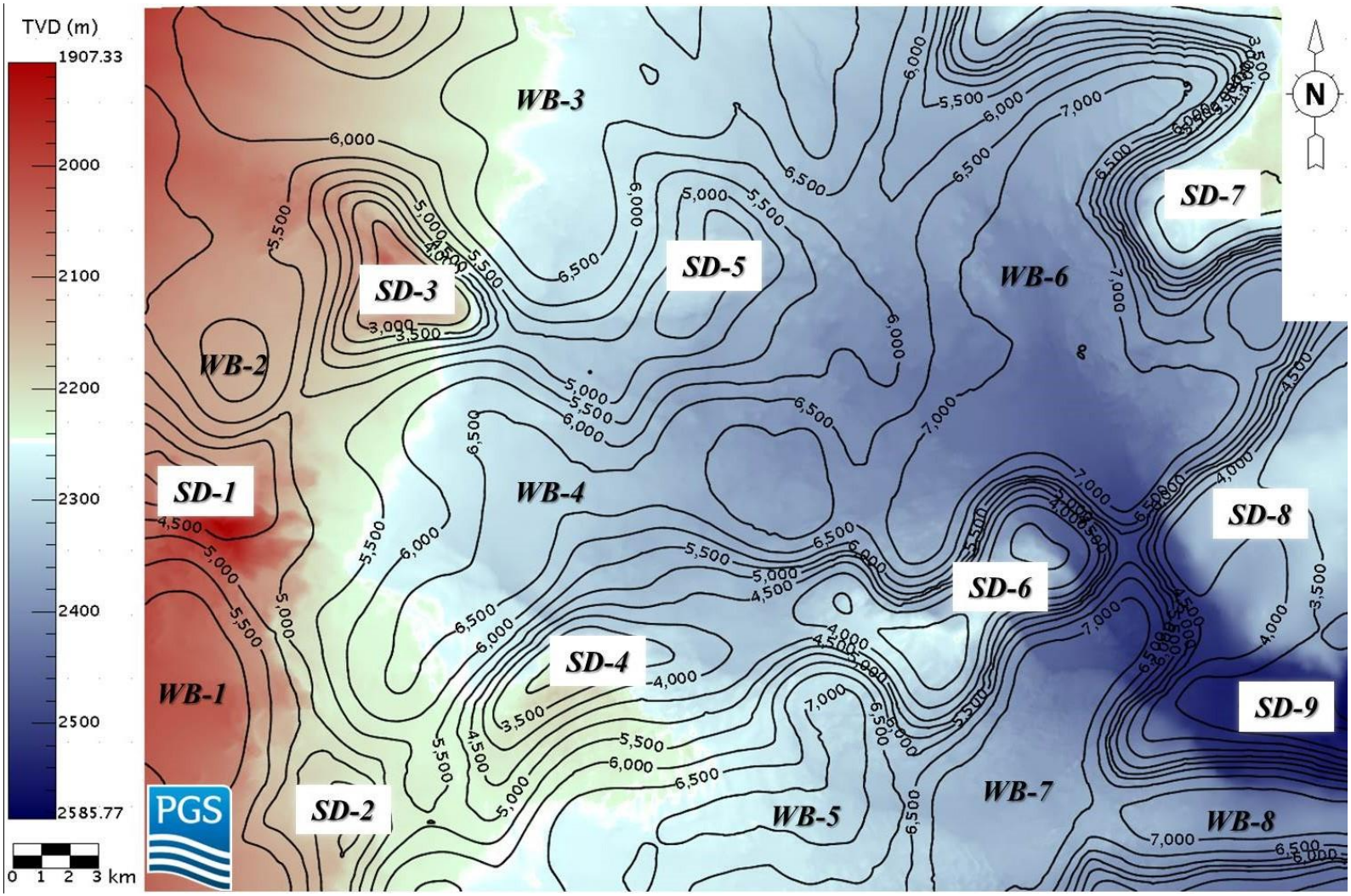

Figure 13: Structural map of the modern seafloor with contours of the top of salt unit.

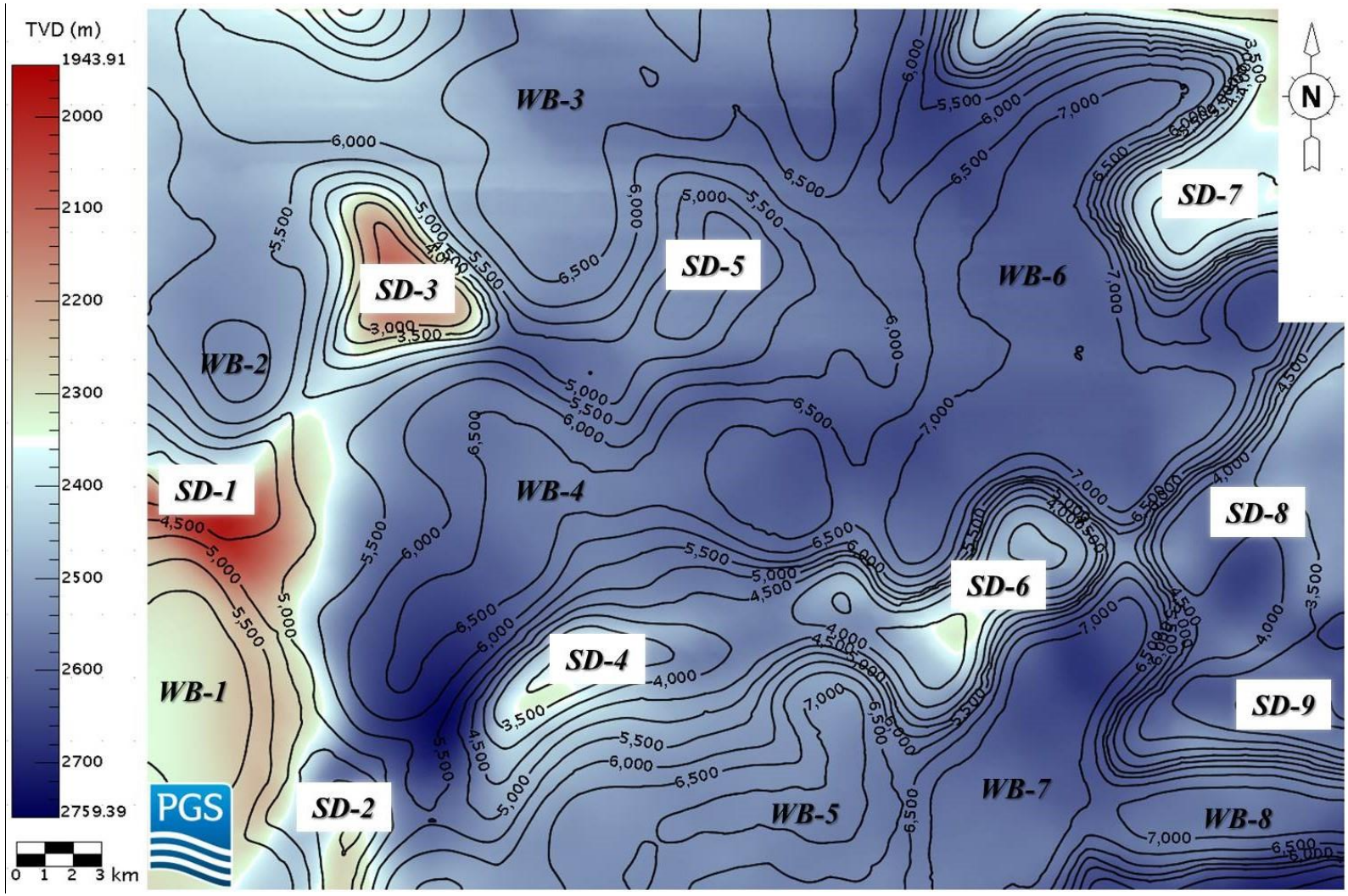

Figure 14: Structural map of the horizon representing a stratigraphic surface contemporaneous with the formation of the submarine channel system, with contours of the top of salt unit.

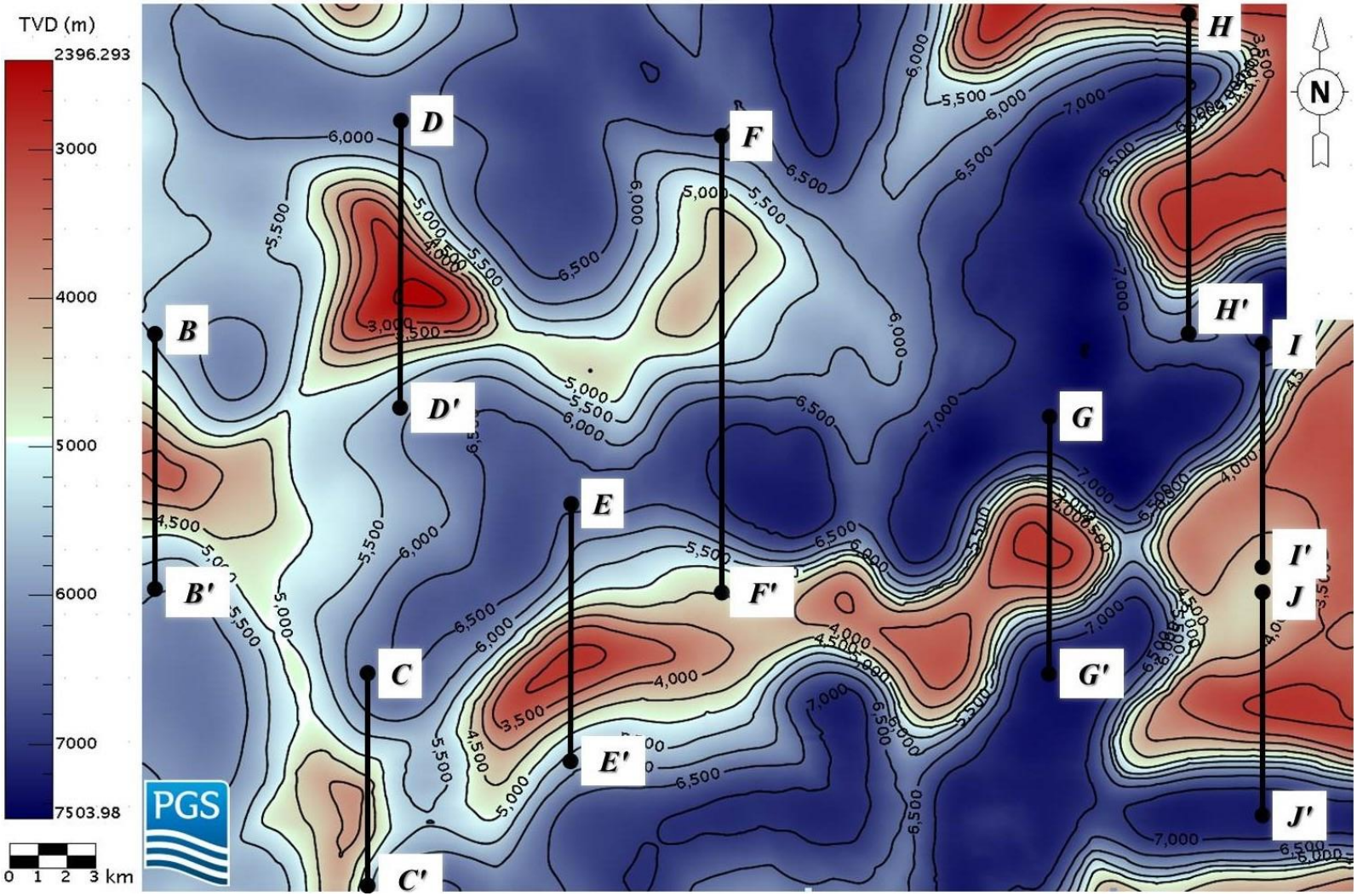

Figure 15: Structural map of the top of salt, showing the locations of cross sections B-B′, C-C′, D-D′, E-E′, F-F′, G-G′, H-H′, I-I′ and J-J′.

SALT DIAPIR 1

I interpreted that both the modern seafloor and the horizon that represents a stratigraphic surface approximately coeval with the formation of the submarine channel system are within the syn-kinematic strata (Figure 16). This indicates that SD-1 was an active salt structure when the submarine channel system started to develop.

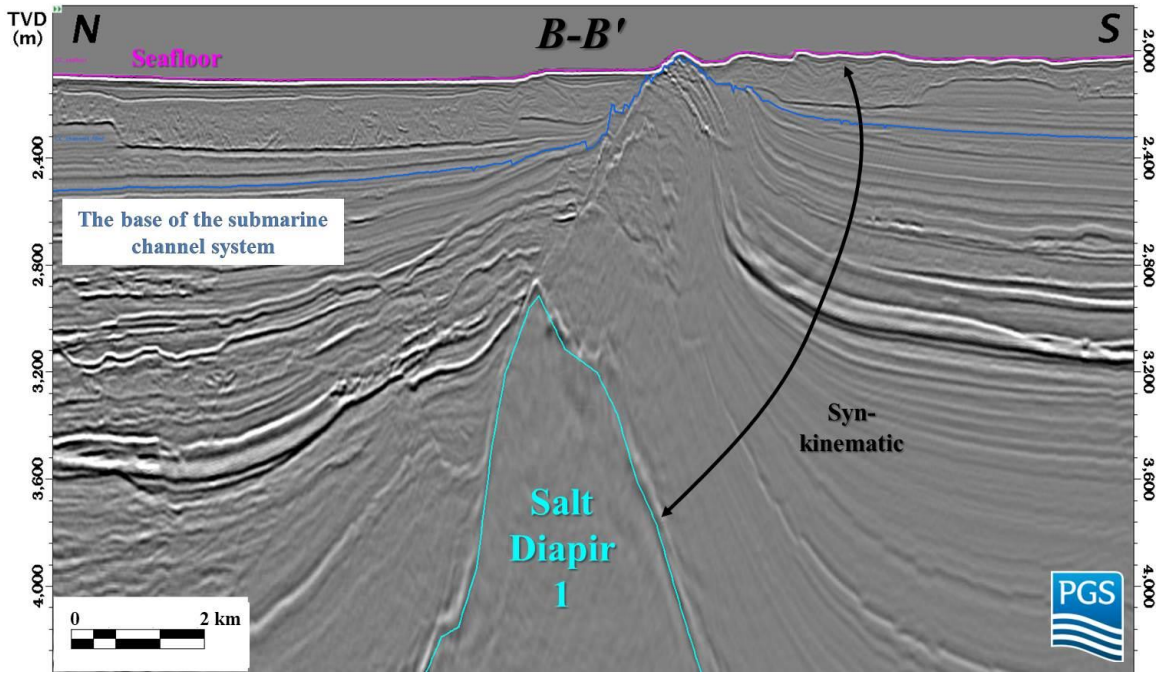

Figure 16: Seismic cross section B-B′ showing the timing of Salt Diapir 1. Location of the cross section is shown in Figure 15.

SALT DIAPIR 2

I interpreted that the horizon that represents a stratigraphic surface approximately contemporaneous with the development of the submarine channel system is within the syn-kinematic strata (Figure 17). Therefore, SD-2 was an active salt structure when the submarine channel system started to form. However, the modern seafloor is within the post-kinematic strata, which suggests that the growth of SD-2 was stopped after the formation of the submarine channel system.

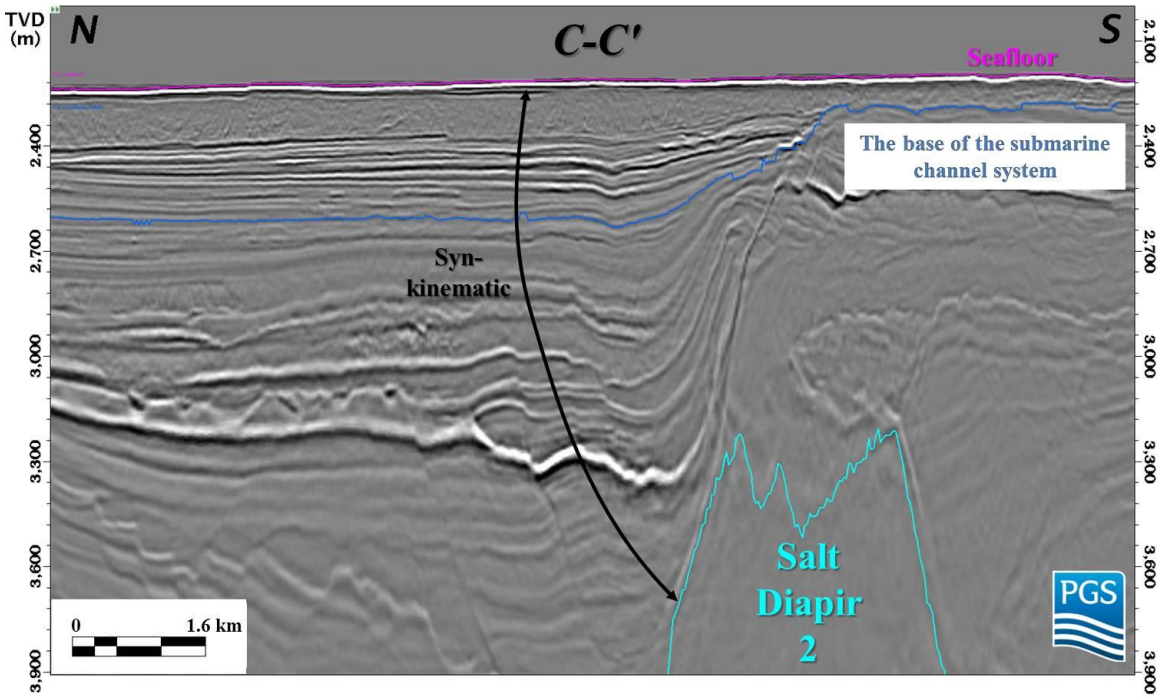

Figure 17: Seismic cross section C-C′ showing the timing of Salt Diapir 2. Location of the cross section is shown in Figure 15.

SALT DIAPIR 3

I interpreted that both the horizon that represents a stratigraphic surface approximately coeval with the formation of the submarine channel system and the modern seafloor are within the syn-kinematic strata (Figure 18). Therefore, SD-3 was an active salt structure when the submarine channel system started to develop.

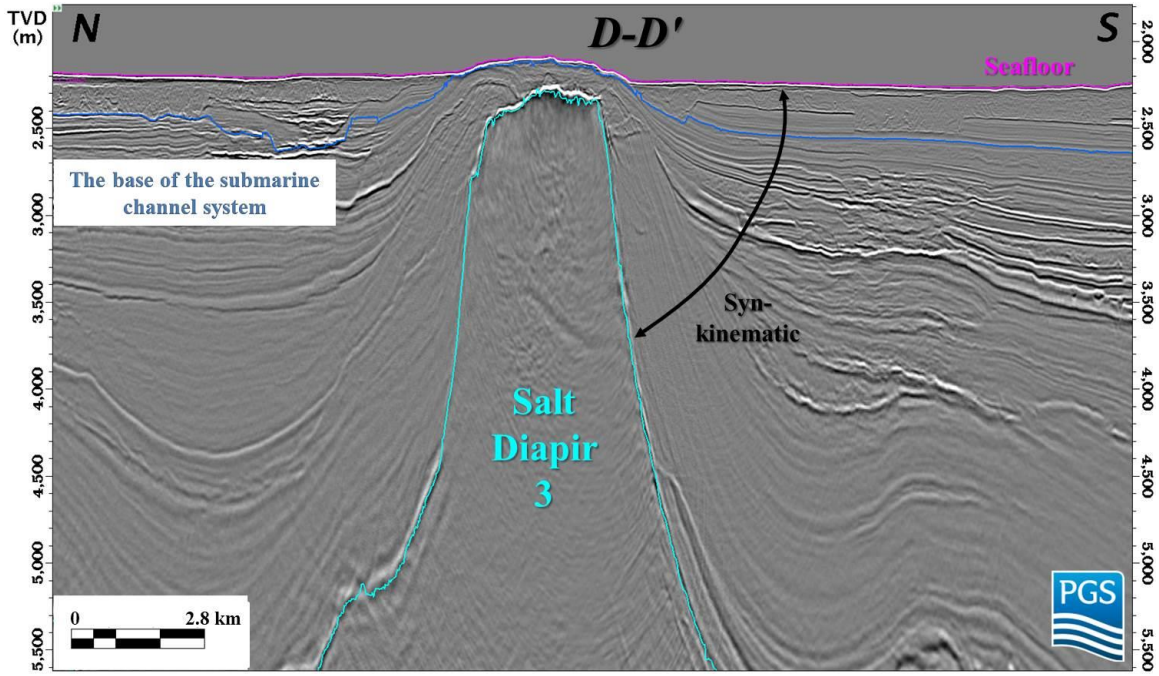

Figure 18: Seismic cross section D-D′ showing the timing of Salt Diapir 3. Location of the cross section is shown in Figure 15.

SALT DIAPIR 4

I interpreted that both the modern seafloor and the horizon that represents a stratigraphic surface approximately contemporaneous with the development of the submarine channel system are within the syn-kinematic strata (Figure 19). This suggests that SD-4 was an active salt structure when the submarine channel system started to form.

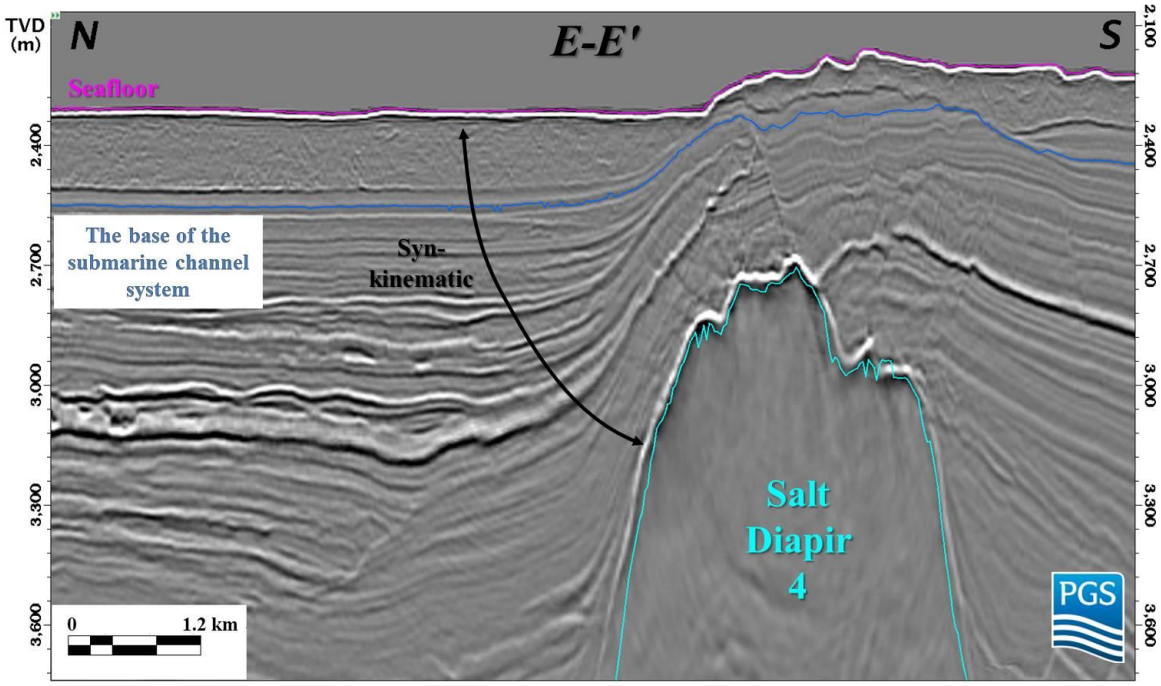

Figure 19: Seismic cross section E-E′ showing the timing of Salt Diapir 4. Location of the cross section is shown in Figure 15.

SALT DIAPIR 5

I interpreted that both the horizon that represents a stratigraphic surface approximately coeval with the formation of the submarine channel system and the modern seafloor are within the syn-kinematic strata (Figure 20). Therefore, SD-5 was an active structure when the submarine channel system started to develop.

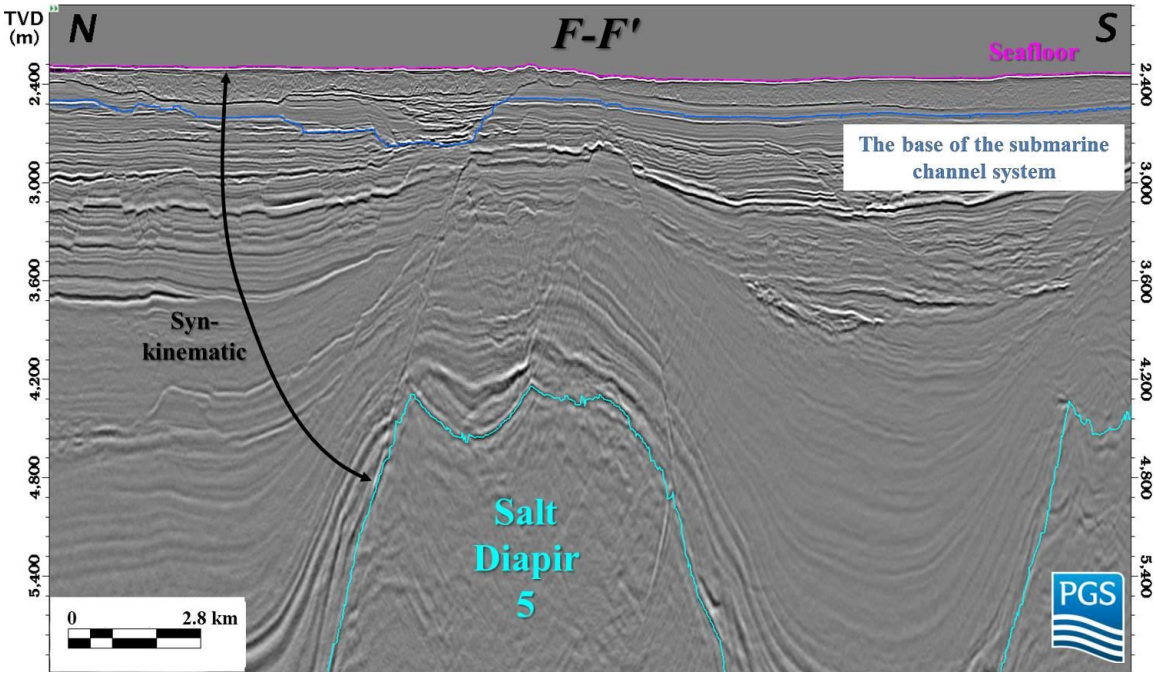

Figure 20: Seismic cross section F-F′ showing the timing of Salt Diapir 5. Location of the cross section is shown in Figure 15.

SALT DIAPIR 6

I interpreted that both the modern seafloor and the horizon that represents a stratigraphic surface approximately contemporaneous with the development of the submarine channel system are within the syn-kinematic strata (Figure 21). This indicates that SD-6 was an active salt structure when the submarine channel system started to form.

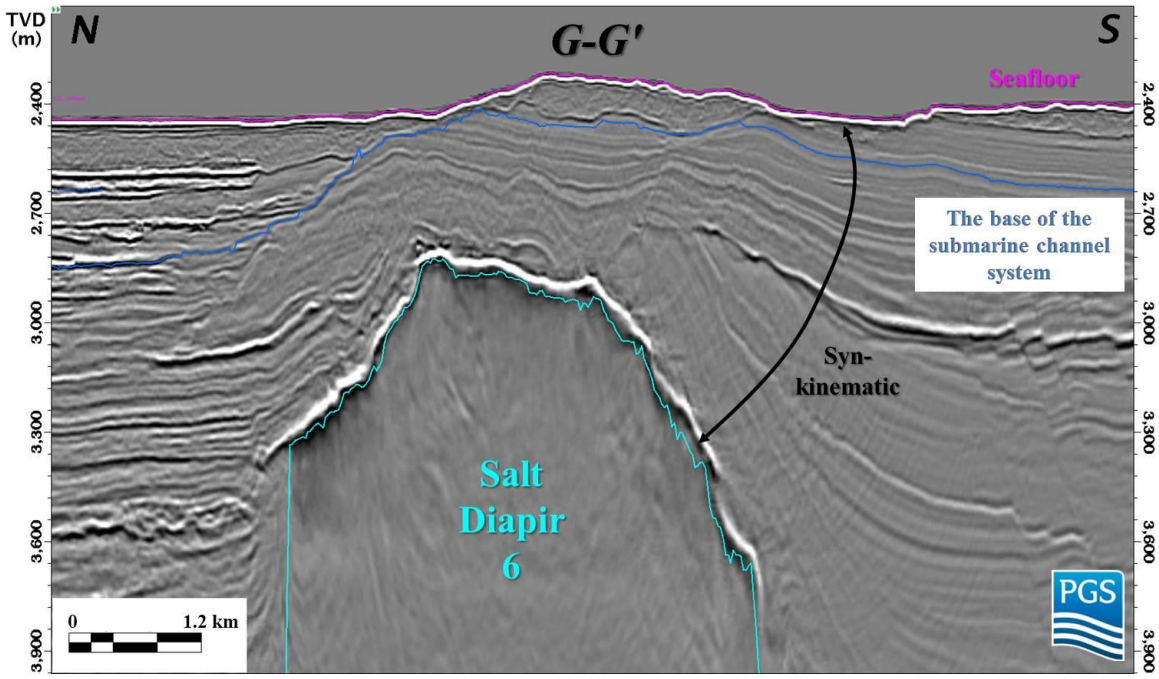

Figure 21: Seismic cross section G-G′ showing the timing of Salt Diapir 6. Location of the cross section is shown in Figure 15.

SALT DIAPIR 7

I interpreted that both the horizon that represents a stratigraphic surface approximately coeval with the formation of the submarine channel system and the modern seafloor are within the syn-kinematic strata (Figure 22). Therefore, SD-7 was an active salt structure when the submarine channel system started to develop.

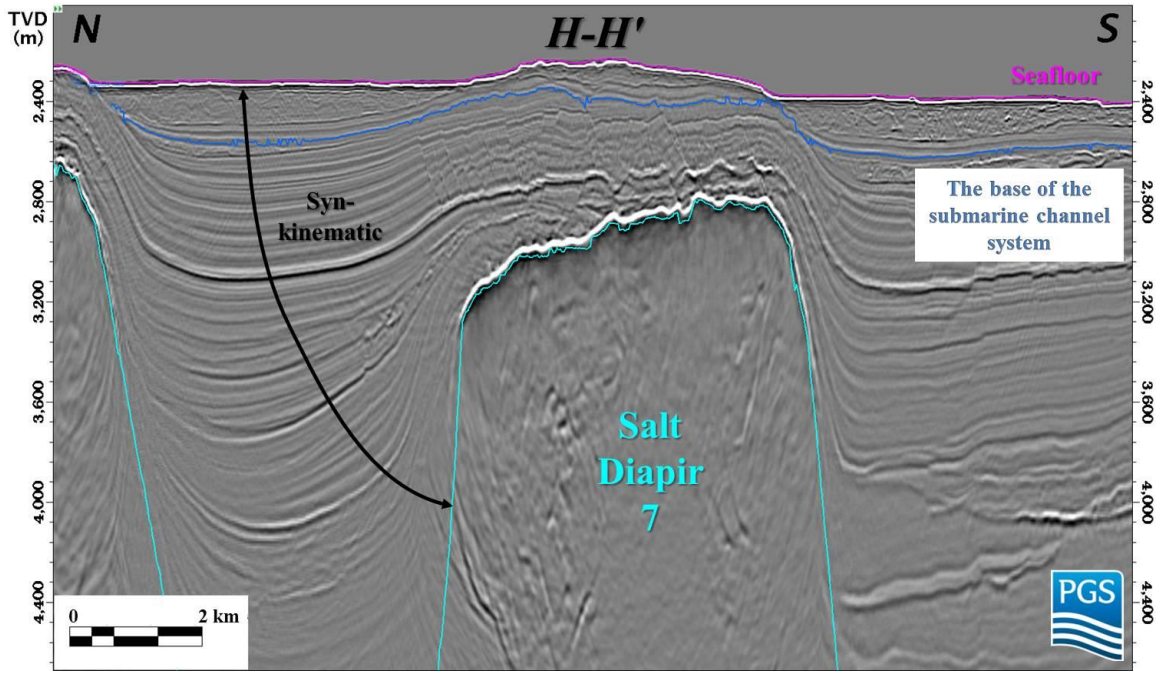

Figure 22: Seismic cross section H-H′ showing the timing of Salt Diapir 7. Location of the cross section is shown in Figure 15.

SALT DIAPIR 8

I interpreted that both the modern seafloor and the horizon that represents a stratigraphic surface approximately contemporaneous with the formation of the submarine channel system are within the syn-kinematic strata (Figure 23). Therefore, SD-8 was an active structure when the submarine channel system started to develop.

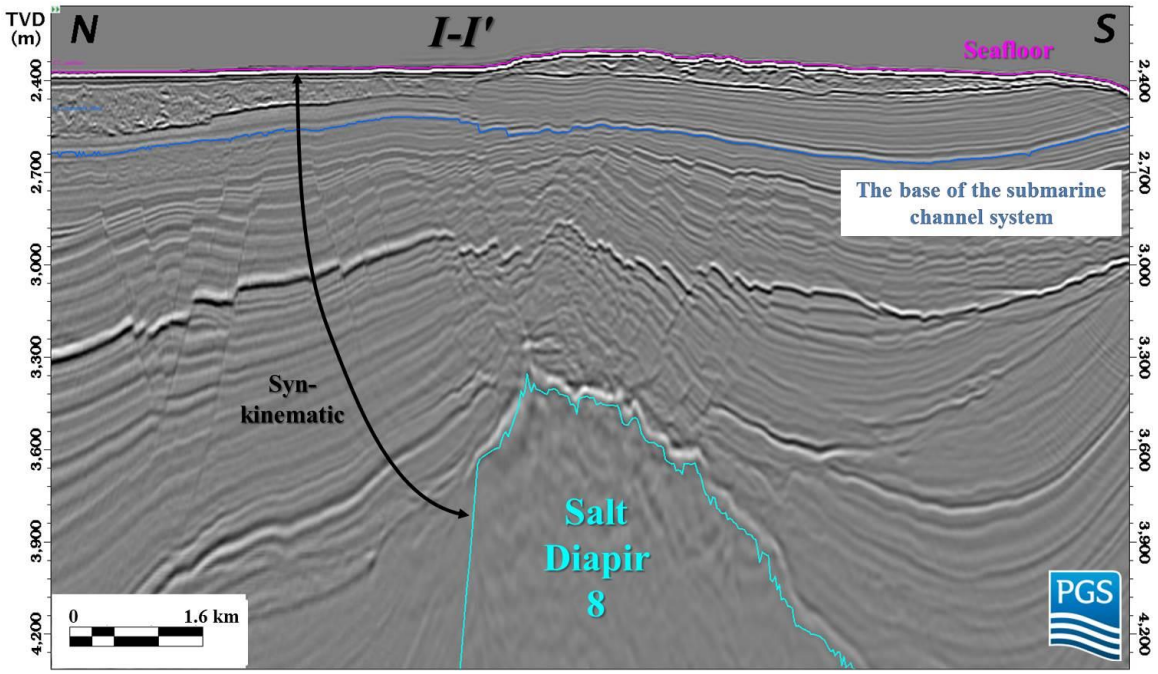

Figure 23: Seismic cross section I-I′ showing the timing of Salt Diapir 8. Location of the cross section is shown in Figure 15.

SALT DIAPIR 9

I interpreted that both the horizon that represents a stratigraphic surface approximately coeval with the development of the submarine channel system and the modern seafloor are within the post-kinematic strata (Figure 24). This indicates that SD-9 predates the formation of the submarine channel system. However, the post-kinematic strata are tilted toward SD-9, which might suggest that another stage of salt movement was started after the accumulation of syn-kinematic strata.

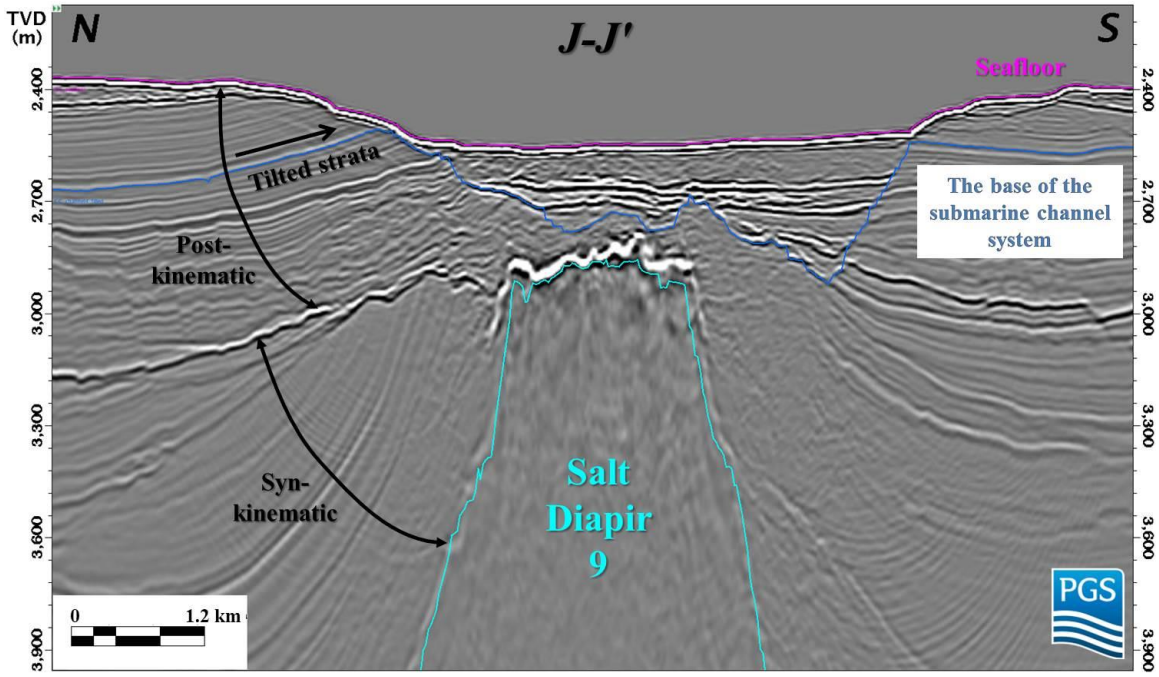

Figure 24: Seismic cross section J-J′ showing the timing of Salt Diapir 9. Location of the cross section is shown in Figure 15.

CHAPTER 3. SUBMARINE CHANNEL SYSTEM

The submarine channel system started to develop after the Miocene. There are no available data for age control of the strata younger than the Miocene. Therefore, I interpreted the age of the submarine channel system as post-Miocene. The stratigraphy of the system is composed of multiple channels and two mass transport complexes. I identified and interpreted these units on the basis of amplitude, internal architecture, cross-sectional continuity and lower bounding surfaces within the 3D seismic-reflection volume (Figure 25) (Mutti & Normark, 1987, 1991; Normark et al., 1993). I interpreted the base of each submarine channel as V or U shaped erosional features on seismic-reflection dataset (Figure 25) (Mayall et al., 2006). The lithology of mass transport complexes generally consists of muddy deposits showing extensive deformation (Shipp et al., 2004). Therefore, I interpreted mass transport complexes by hummocky, chaotic and medium-to-low amplitude reflections within the dataset (Figure 25) (Posamentier & Kolla, 2003). In cross sections, these units are characterized by a sharp, erosional base surface and a locally folded or faulted internal architecture, with high-to-moderate cross-sectional continuity (Figure 25) (Posamentier & Kolla, 2003).

I characterized submarine channels within the system to observe changes in their measured parameters as a result of their interaction with salt-influenced structures. For this purpose, I interpreted structure and isochore maps of each channel. The aim of producing isochore maps is to understand how channel development responds to the underlying salt-influenced slope as a whole. From the structure maps, I measured channel erosional depth, channel width, channel gradient and sinuosity parameters (Figure 26) (e.g., Gee & Gawthorpe, 2007; Clark & Cartwright, 2009; Gamboa et al., 2012). I determined channel erosional depth as the maximum depth of incision into the pre-

channel sequence and measured channel width as the horizontal distance between opposite channel flanks (Figure 26) (Clark & Cartwright, 2009). I measured channel gradient by determining the ratio of drop in the channel elevation per unit horizontal distance and determined sinuosity as the along-channel distance (sinuous length) divided by the straight-line distance between the same two points along the deepest part of the channel horizon (Figure 26) (Clark & Cartwright, 2009). I measured these parameters roughly every 3 km along the sinuous length of each channel in downslope direction, as I observed that this adequately captures variations in channel morphology.

The development of the submarine channel system began after the Miocene, and the system reaches the modern seafloor in the southeastern part of the study area. Four channels exist within the system, which are Channel 1 to Channel 4 from oldest to youngest (Figure 25). Between the development of Channel 3 and Channel 4, an erosive mass transport complex entered the study area and was deposited around the northwestern part of the system. The entire system is covered by another mass transport complex, which mainly shaped the modern seafloor within the study area (Figure 25).

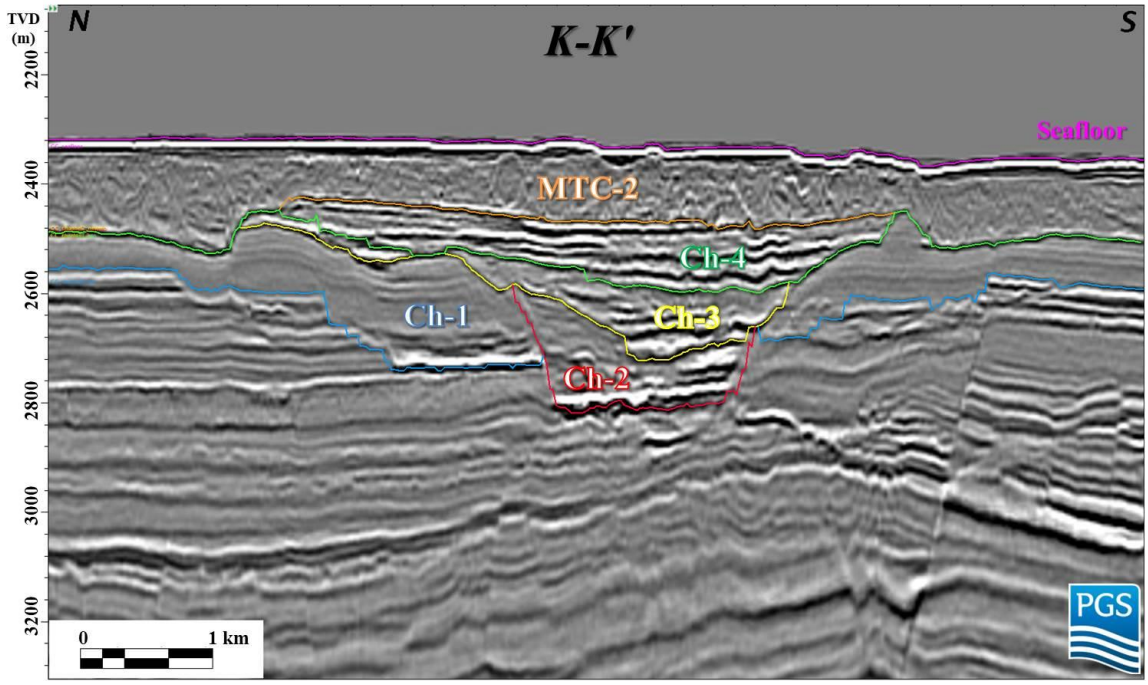

Figure 25: Seismic cross section K-K′ showing individual units within the submarine channel system. Location of the cross section is shown in Figures 27, 39, 51 and 59.

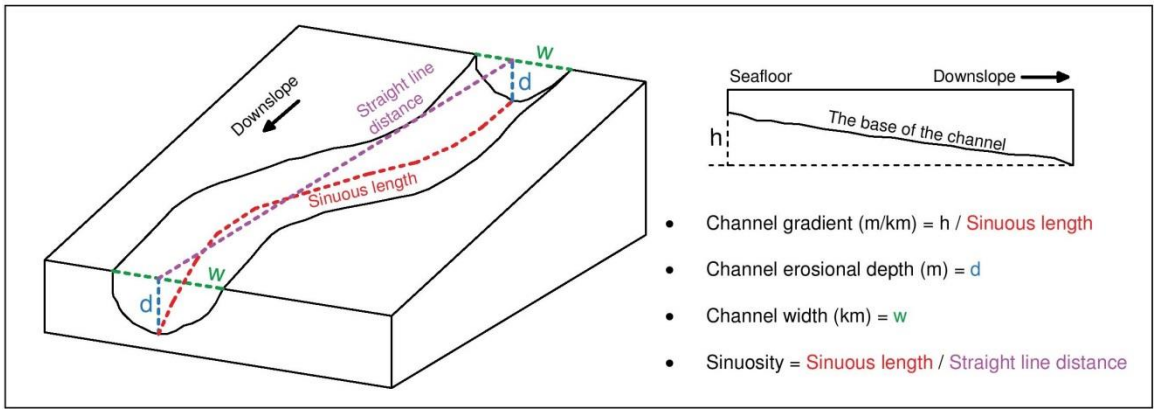

Figure 26: Diagram showing measured parameters for the characterization of channels.

Channel 1

Channel 1, the oldest channel within the system (Figure 25), is shown in blue in seismic cross sections represented in this study. The isochore map of the sequence between the base of Channel 1 and the base of Channel 2 shows thickness reaching up to approximately 320 m within salt-withdrawal basins and decreasing dramatically around the crests of salt-influenced structural highs (Figure 28).

Channel 1 is almost completely eroded by younger channels within the system, and it is rarely observable within the seismic-reflection dataset (Figure 27). Therefore, it is not possible to determine the channel width, channel erosional depth, sinuosity or gradient along the entire pathway of Channel 1. Remnants of the erosional base of Channel 1 can be seen only in the northwestern and northern parts of the study area, where the channel has an average width of 6.2 km and channel incision reaches as much as 170 m (Figure 28). Considering the flow direction of younger channels within the submarine channel system, I assume that the pathway of Channel 1 was sourced from the northwest and had a general NW-to-SE transport direction (Figures 39, 51 and 59).

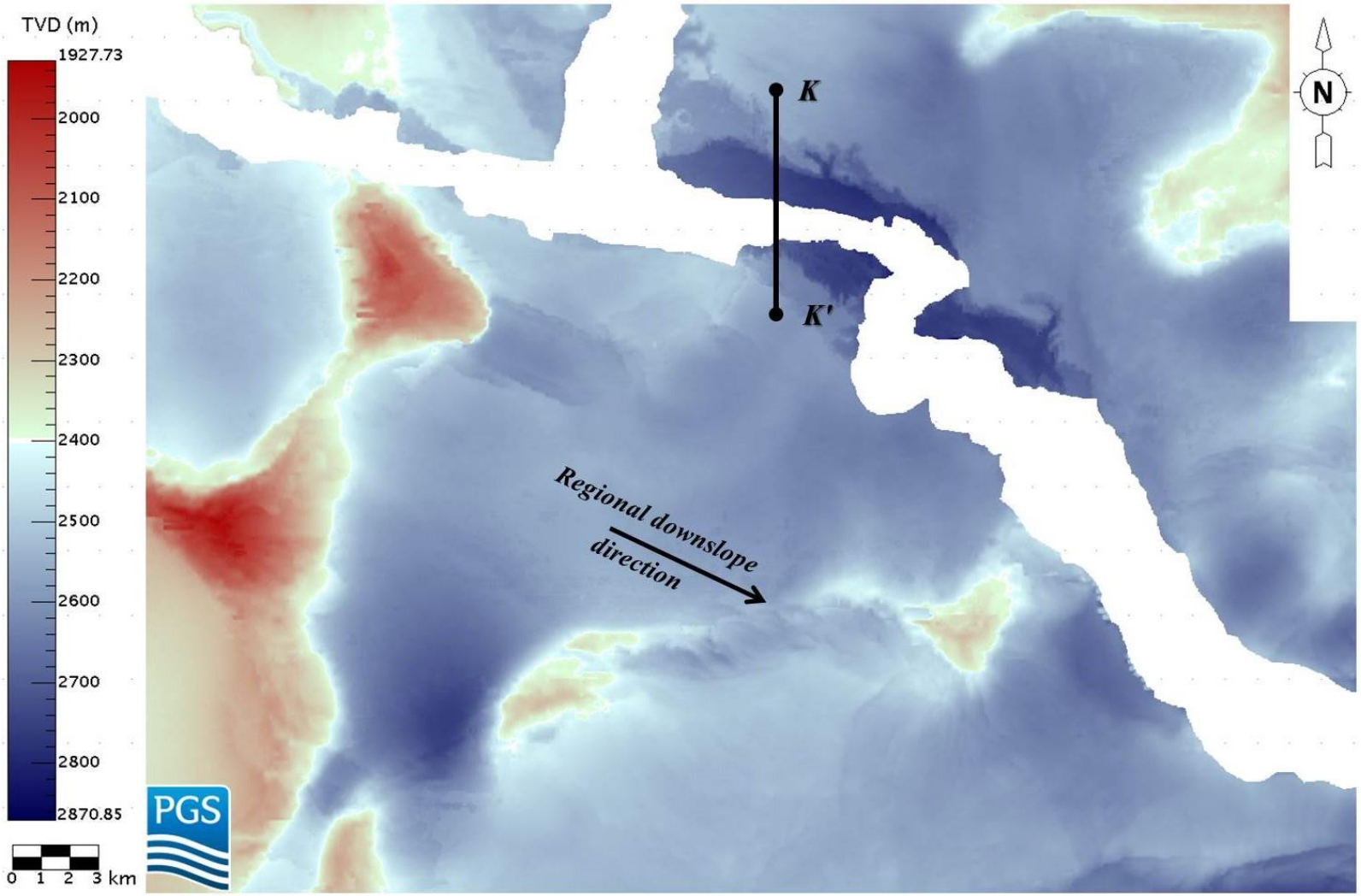

Figure 27: Structural map of the base of Channel 1. Map also shows the location of seismic cross section K-K′.

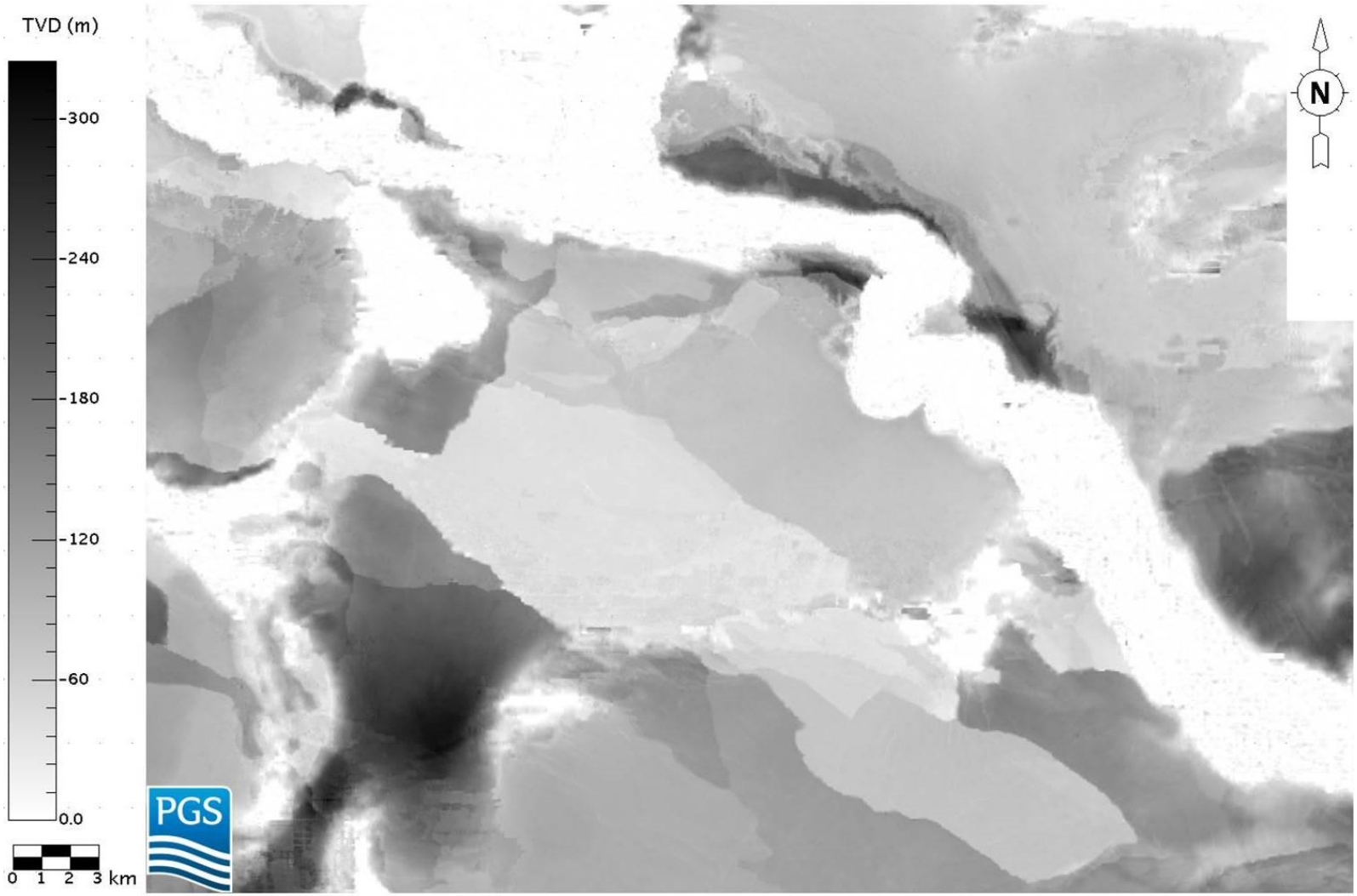

Figure 28: Isochore map showing the remnants of deposits filling Channel 1 and the sequence between Channel 2 and Channel 1.

Channel 2

The base erosional surface of Channel 2 is shown in red in seismic cross sections represented in this study. Channel 2 is younger than Channel 1, as it truncated Channel 1 (Figure 25). Channel 2 comprises two tributaries, identified as NW-2 (northwest tributary, Channel 2) and N-2 (north tributary, Channel 2) (Figure 39). Both tributaries have an average sinuosity of 1.12 and a maximum incision depth of 250 m (Figure 29 & Figure 32). The average gradients in the tributaries are similar, ranging from 8 m/km to 10 m/km (Figure 30). NW-2 and N-2 have an average channel width of 2.5 km and 3.8 km, respectively (Figure 31). Two tributaries converged into a single main channel in the northwestern part of the study area, joining at an angle of approximately 90° and at equal elevations at the confluence point (Figure 33). The N-2 tributary truncated the NW-2 tributary at the confluence point, so N-2 is younger than NW-2 (Figure 34). Compared to the NW-2 tributary, deposits filling the N-2 tributary are less preserved within the seismic-reflection dataset (Figure 40), as a result of higher amount of erosion by younger channels within the submarine channel system.

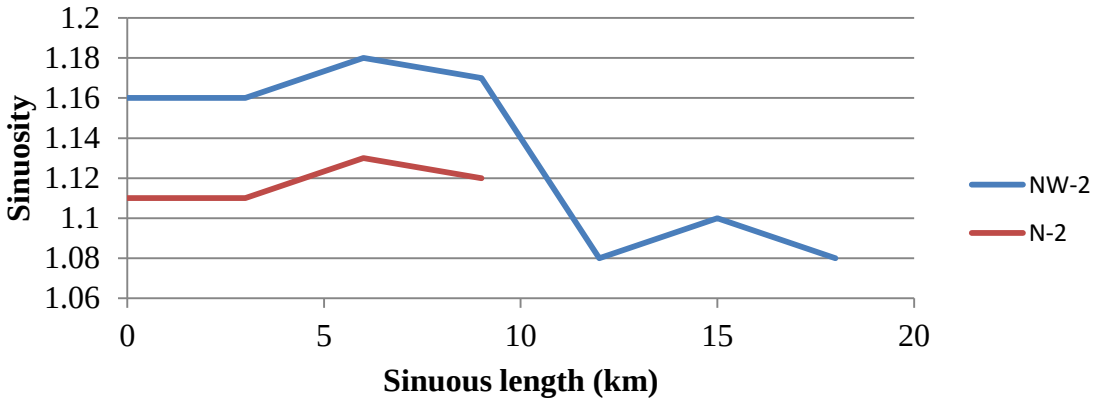

Figure 29: Graph showing sinuosity variations in the NW-2 and N-2 tributaries. Zero point is where tributaries entered the study area.

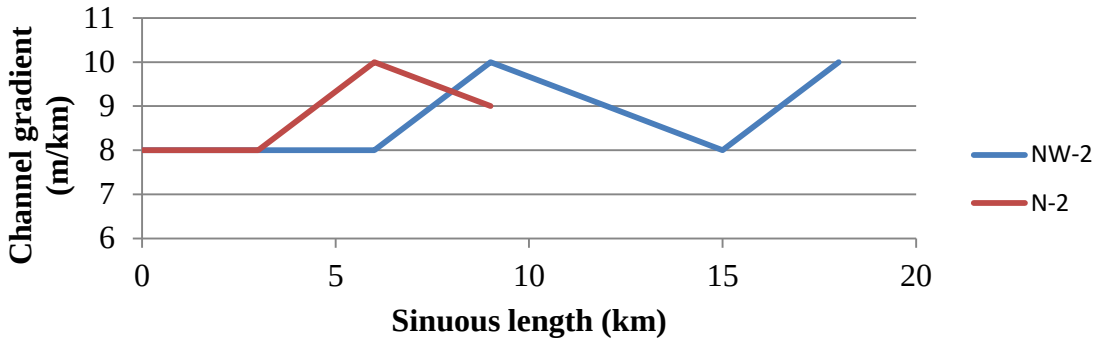

Figure 30: Graph showing gradient variations in the NW-2 and N-2 tributaries. Zero point is where tributaries entered the study area.

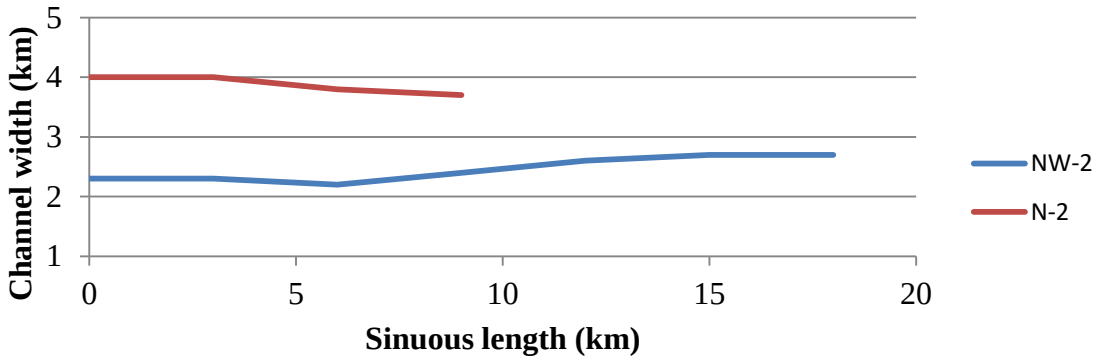

Figure 31: Graph showing width variations in the NW-2 and N-2 tributaries. Zero point is where tributaries entered the study area.

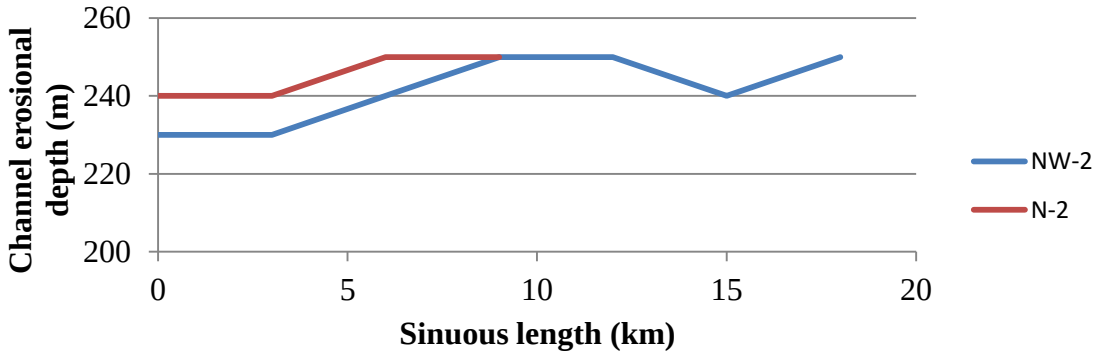

Figure 32: Graph showing erosional depth variations in the NW-2 and N-2 tributaries. Zero point is where tributaries entered the study area.

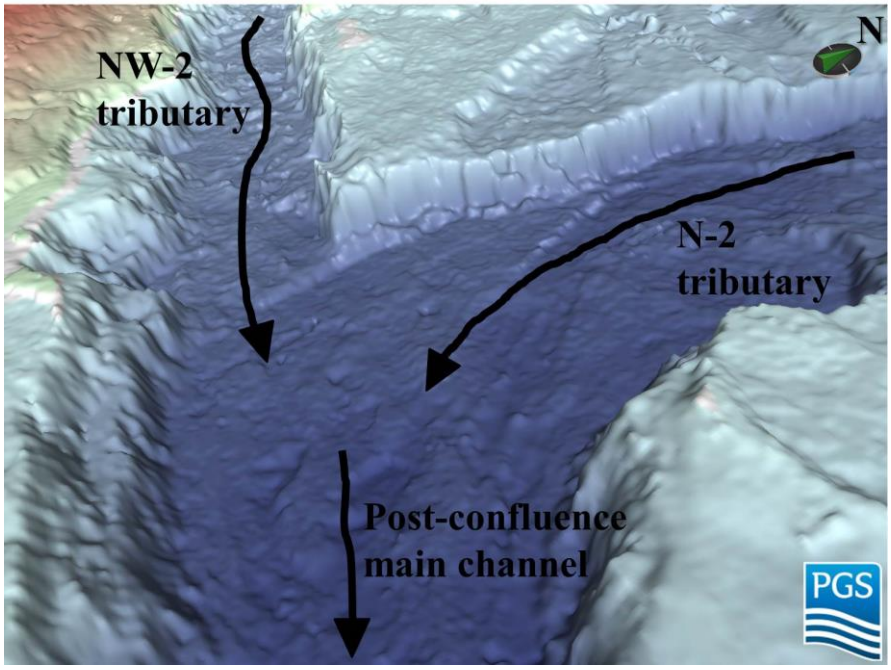

Figure 33: 3D view of the confluence geometry in Channel 2.

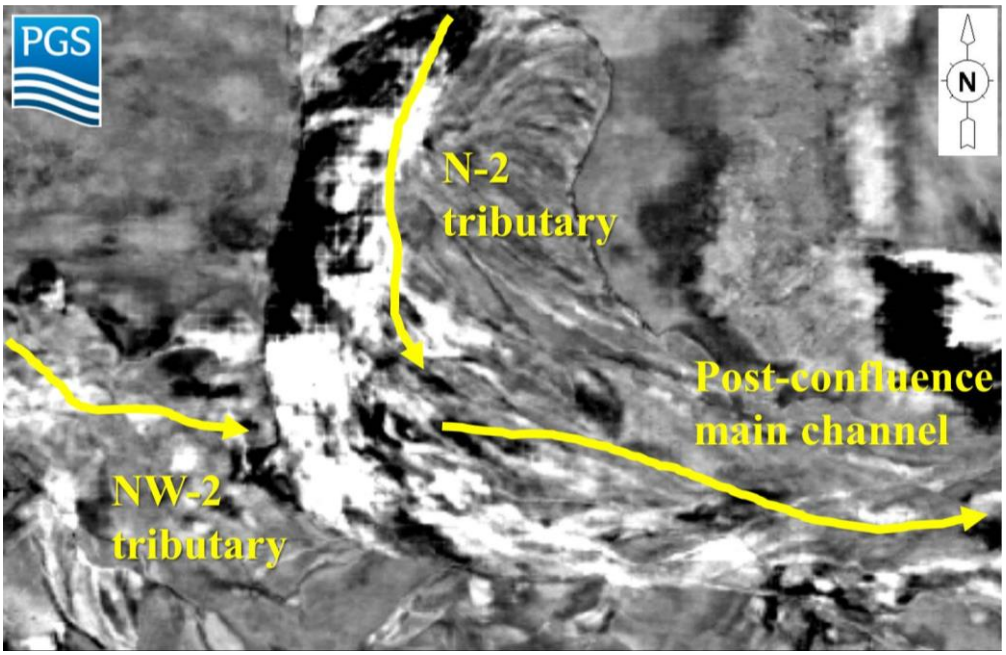

Figure 34: Horizontal slice at the depth of 2710 m showing N-2 tributary truncating NW-2 tributary.

Downslope of the confluence point, the flow direction of the single main channel continued to the east from WB-3 to WB-6 (Figure 39 & Figure 65) for 12 km as a straight channel (Figure 35), with an average width of 2.3 km and a maximum erosional depth of 340 m (Figure 37 & Figure 38). Within this part, Channel 2 has a gradient of 7 m/km (Figure 36). The channel was diverted to the southeast with a significant increase in its sinuosity to 1.73 (Figure 35 & Figure 39). This part of the channel has an average width of 3.6 km (Figure 37), a maximum incision depth of 320 m (Figure 38) and an average gradient of 3.7 m/km (Figure 36). Channel 2 maintained its flow in the same direction for 15 km after the section with high sinuosity, to pass through a depression between SD-6 and SD-8 (Figure 39 & Figure 65). The channel displays a sudden reduction in sinuosity to a value of 1.11 and an increase in its maximum erosional depth to 500 m (Figure 35 & Figure 38). Within this part, the channel has an average width of 3.5 km and average gradient of 2 m/km (Figure 36 & Figure 37). The channel reaches the modern seafloor within this section (Figure 7). After passing through a depression between SD-6 and SD-8, the channel changed its transport direction to the east, to flow directly on the top of SD-9 (Figure 39 & Figure 65). The sinuosity of the channel is again increased dramatically, to 1.79 (Figure 35). This section of the channel is characterized with a maximum incision depth of 530 m and an average width of 2.6 km (Figure 37 & Figure 38). Within this part of the channel, average gradient decreases to -4.5 m/km, which means that channel elevation is increasing downslope (Figure 36). This is probably caused by the uplift of SD-9 below the channel pathway (Figure 65). Deposits filling Channel 2 are highly condensed or almost absent within this area, as a result of erosion by younger channels within the system (Figure 40).

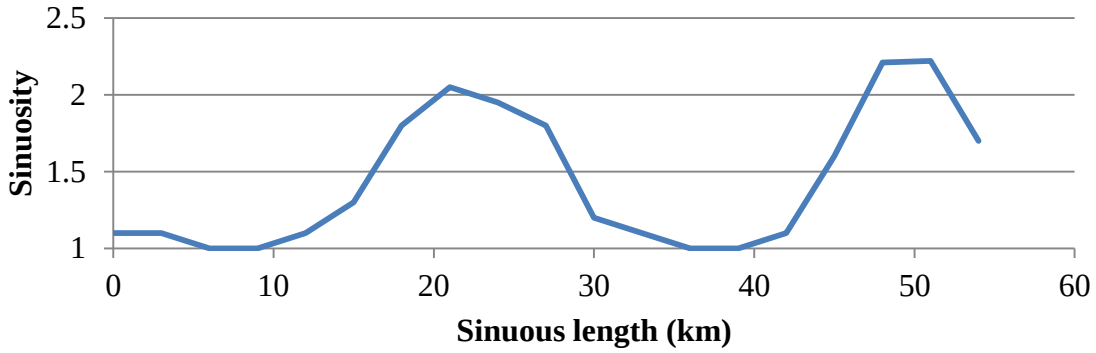

Figure 35: Graph showing sinuosity variations in the post-confluence section of Channel 2. Zero point is the confluence point.

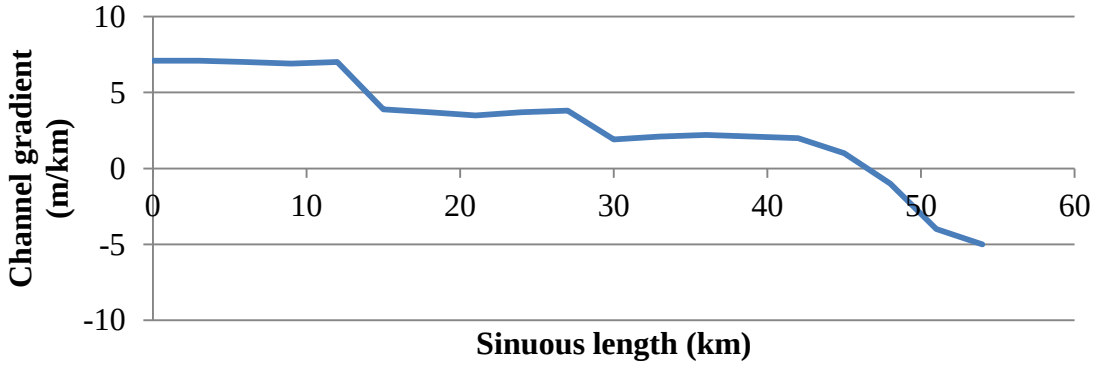

Figure 36: Graph showing gradient variations in the post-confluence section of Channel 2. Zero point is the confluence point.

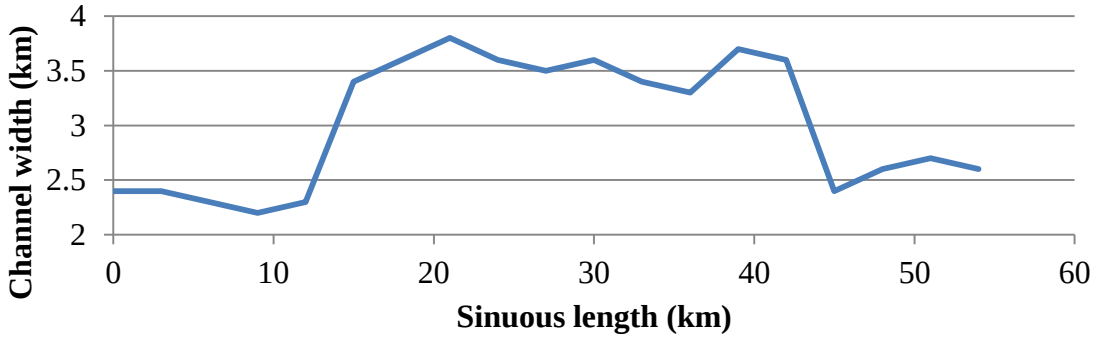

Figure 37: Graph showing width variations in the post-confluence section of Channel 2. Zero point is the confluence point.

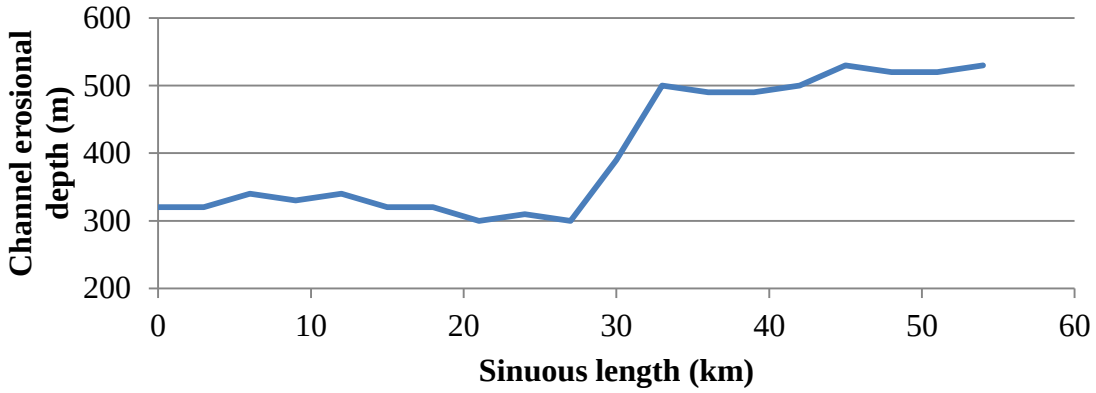

Figure 38: Graph showing erosional depth variations in the post-confluence section of Channel 2. Zero point is the confluence point.

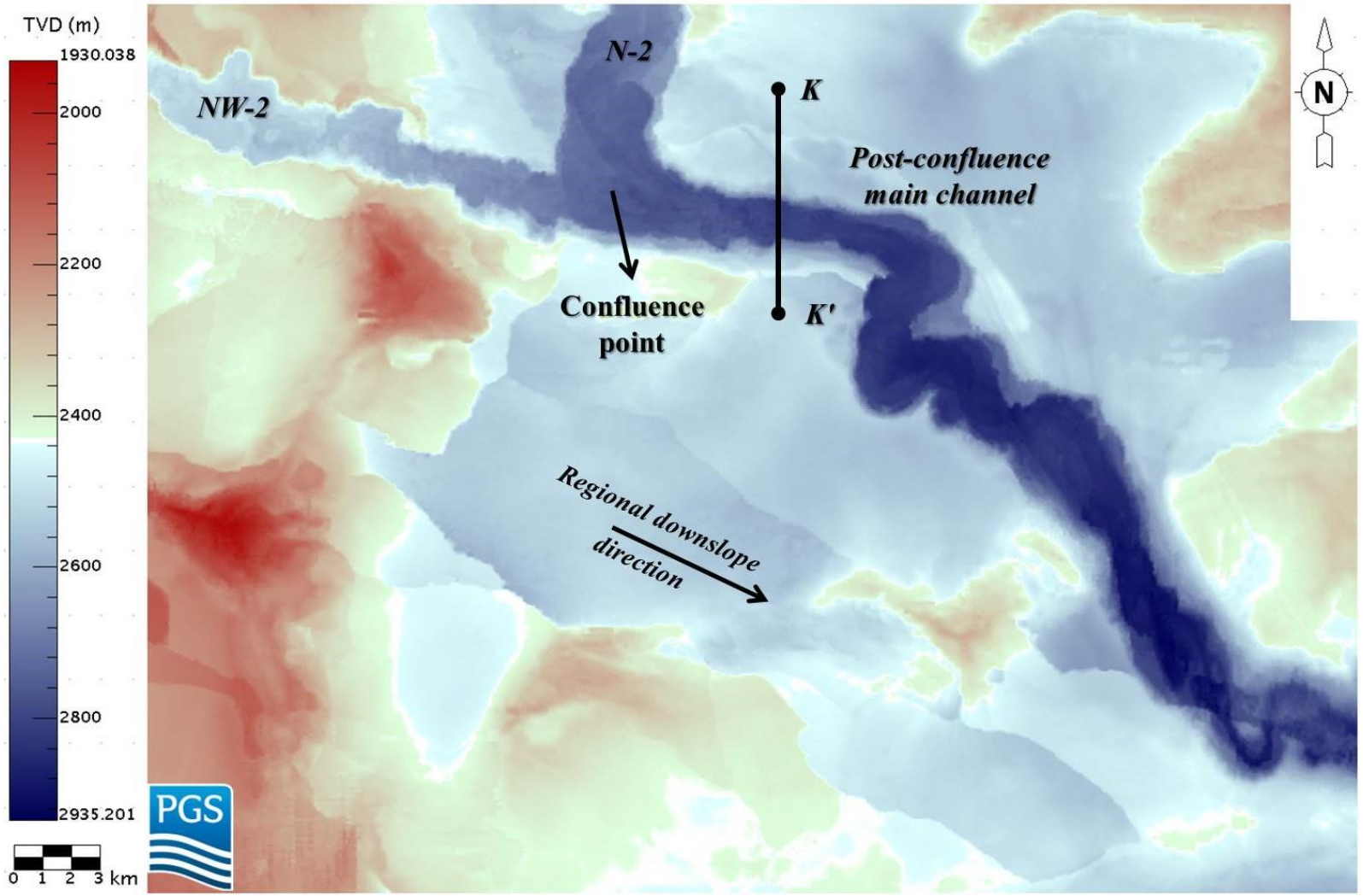

Figure 39: Structural map of the base of Channel 2. Map also shows the location of seismic cross section K-K′.

Figure 40: Isochore map of deposits filling Channel 2.

Channel 3

Within the seismic cross sections shown in this study, the base surface of Channel 3 is represented in yellow. Because Channel 3 cut Channel 2, it is younger than Channel 2 (Figure 25). As was Channel 2, Channel 3 was sourced with two tributaries, referred to as NW-3 (northwest tributary, Channel 3) and N-3 (north tributary, Channel 3) (Figure 51). Both tributaries have a similar maximum erosional depth, ranging from 160 m to 180 m (Figure 44). N-3 is more sinuous compared to NW-3, with sinuosity values of 1.22 and 1.12, respectively (Figure 41). NW-3 has a gradually increasing channel width downslope, from 1.2 km to 2.2 km, and N-3 has an average channel width of 1.6 km (Figure 43). Two tributaries of Channel 3 are characterized by significantly different gradient values, where NW-3 has an average gradient of 11.9 m/km and N-3 has an average gradient of 3.3 m/km (Figure 42). Similar to Channel 2, two tributaries of Channel 3 joined into a single main channel within the northwestern part of the study area, where they merged at an angle of approximately 90° (Figure 51). They met at different elevations, and there is a step of approximately 100 m where NW-3 joined the post-confluence channel (Figure 45). In contrast, N-3 joined the main channel at a similar depth (Figure 45). As observed in the horizontal slice obtained from the semblance volume, the N-3 tributary cut the NW-3 tributary at the confluence point, which demonstrates that NW-3 is older than N-3 (Figure 46). Compared to NW-3, deposits filling the N-3 tributary are more preserved within the seismic-reflection dataset (Figure 52).

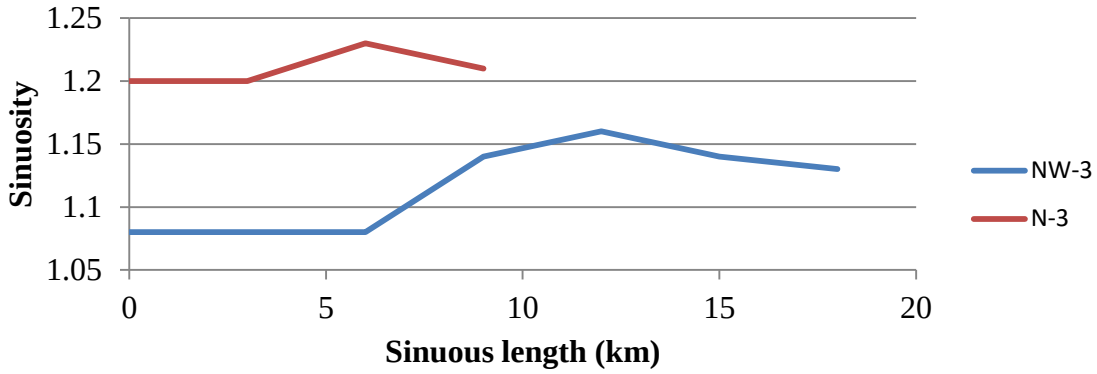

Figure 41: Graph showing sinuosity variations in the NW-3 and N-3 tributaries. Zero point is where tributaries entered the study area.

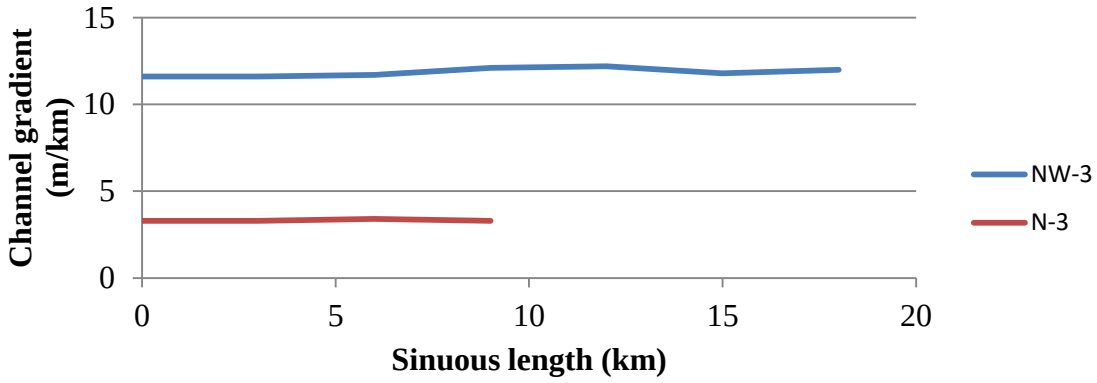

Figure 42: Graph showing gradient variations in the NW-3 and N-3 tributaries. Zero point is where tributaries entered the study area.

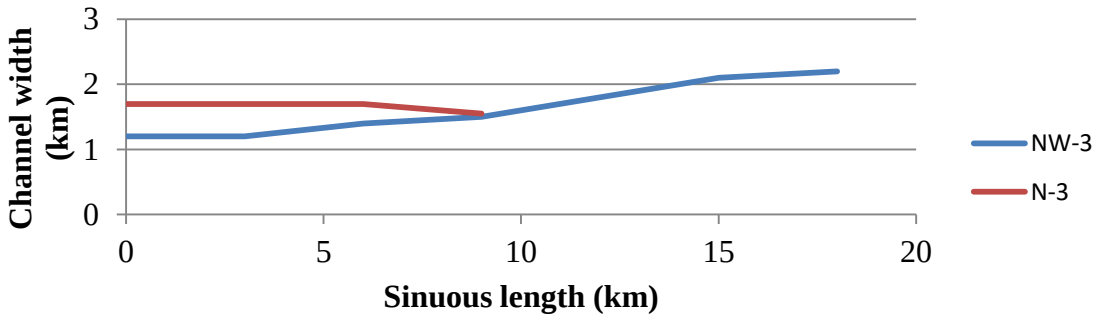

Figure 43: Graph showing width variations in the NW-3 and N-3 tributaries. Zero point is where tributaries entered the study area.

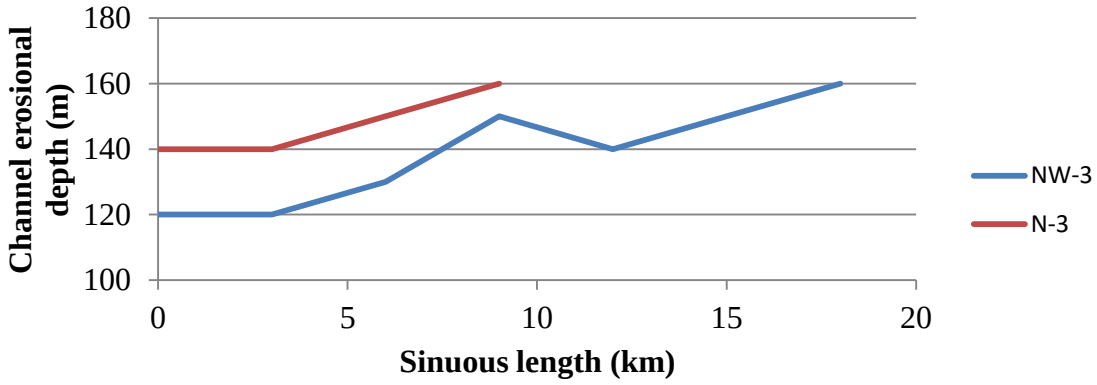

Figure 44: Graph showing erosional depth variations in the NW-3 and N-3 tributaries. Zero point is where tributaries entered the study area.

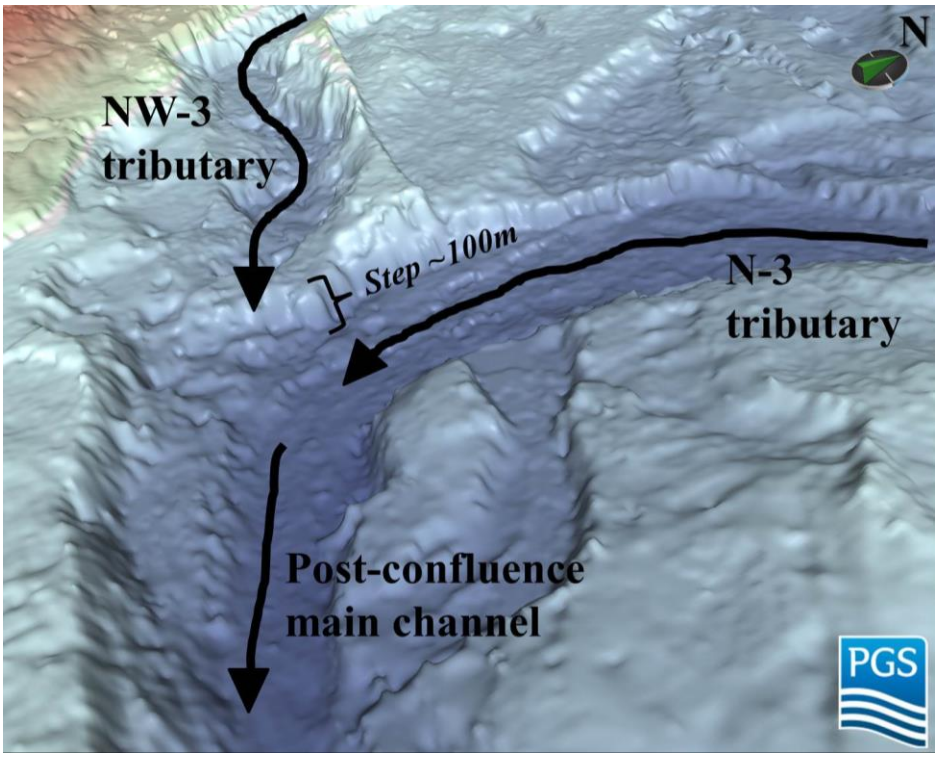

Figure 45: 3D confluence geometry in Channel 3.

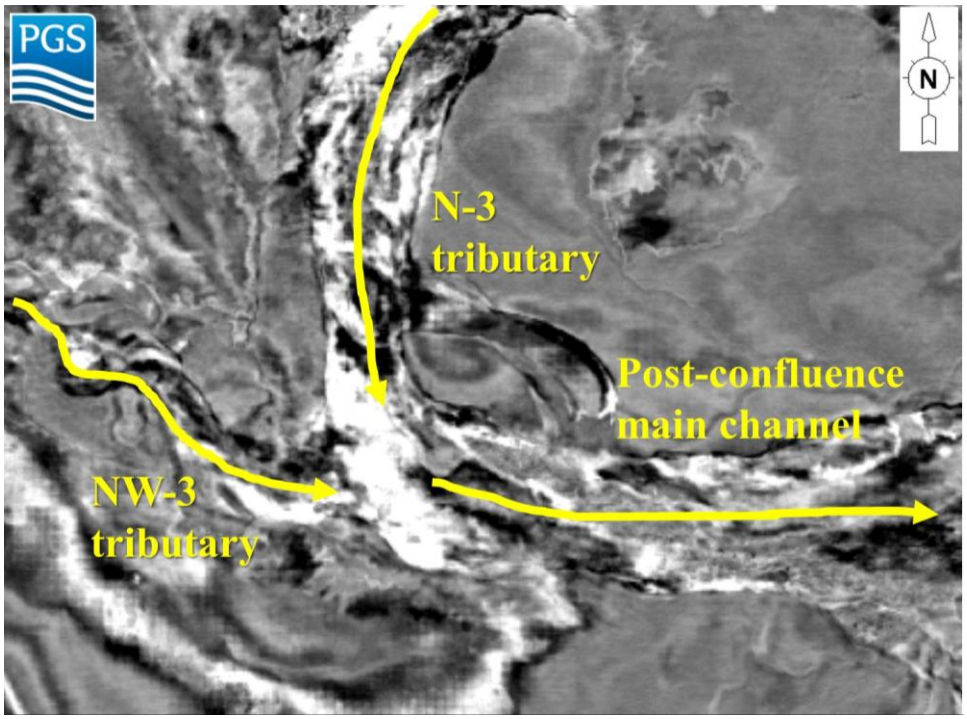

Figure 46: Horizontal slice at the depth of 2580 m showing N-3 tributary truncating NW-3 tributary.

The post-confluence main channel maintained its transport direction to the east from WB-3 to WB-6 (Figure 51 & Figure 66) for 12 km as a straight channel from the confluence point (Figure 47), with a maximum incision depth of 270 m (Figure 50) and an average width of 2.4 km (Figure 49). This part of the channel is characterized by a gradient of 5.4 m/km (Figure 48). The channel changed its flow direction to the southeast with a sudden increase in sinuosity to 1.98 (Figure 47 & Figure 51). The channel decreased its maximum erosional depth to 220 m (Figure 50), and it has an average width of 2.3 km (Figure 49) and an average gradient of 4.1 m/km within this part (Figure 48). Then, the channel followed the same transport direction for 12 km and passed through a depression between SD-6 and SD-8 (Figure 51 & Figure 66), with a significant decrease in sinuosity to 1.15 (Figure 47). Similar to Channel 2, the maximum incision depth

increased within this section to 400 m (Figure 50). This part of the channel is characterized by an average gradient of 5.2 m/km and an average width of 2.5 km (Figure 48 & Figure 49). Channel 3 reaches the modern seafloor within this section (Figure 7). After passing through a depression between SD-6 and SD-8, the channel was diverted to the east to flow directly on the top of SD-9 (Figure 51 & Figure 66). A significant increase in the channel sinuosity is observed within this part, as it reaches to a value of 1.74 (Figure 47). This part of the channel has an average width of 2.7 km and a maximum erosional depth of 420 m (Figure 49 & Figure 50). Average gradient decreases to 1.7 m/km, as a result of salt-influenced uplift (Figure 48). Compared to Channel 2, deposits filling Channel 3 are preserved more within this section (Figure 52).

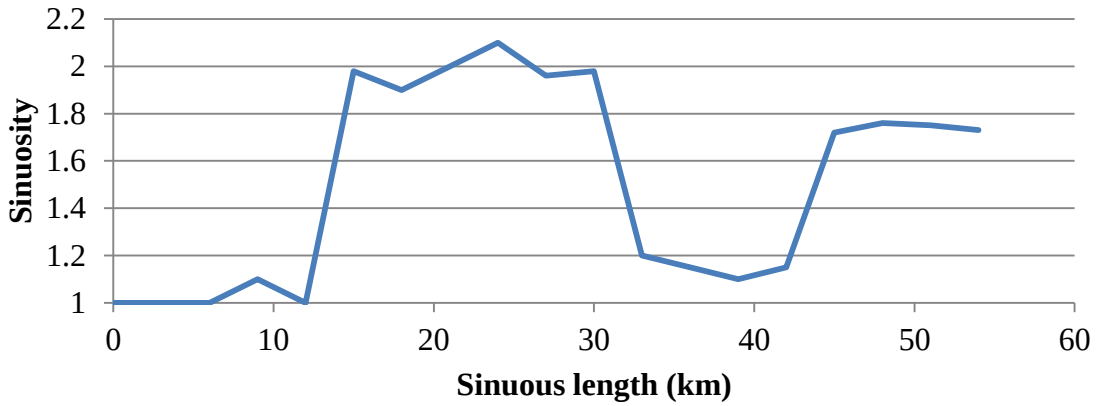

Figure 47: Graph showing sinuosity variations in the post-confluence section of Channel 3. Zero point is the confluence point.

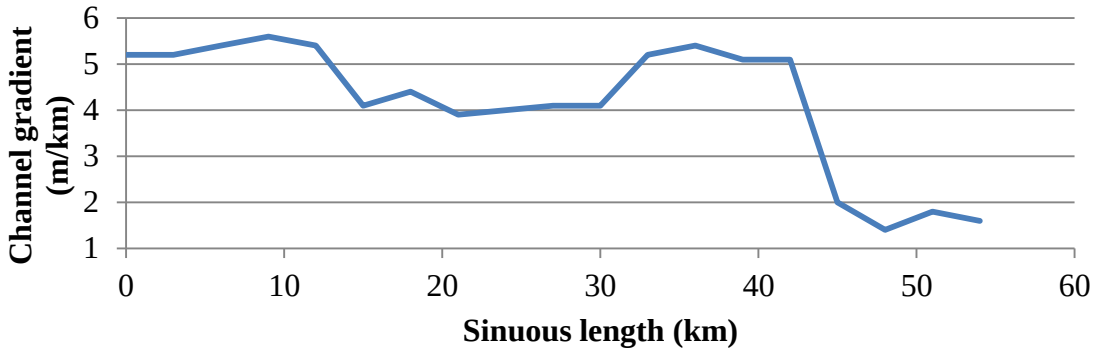

Figure 48: Graph showing gradient variations in the post-confluence section of Channel 3. Zero point is the confluence point.

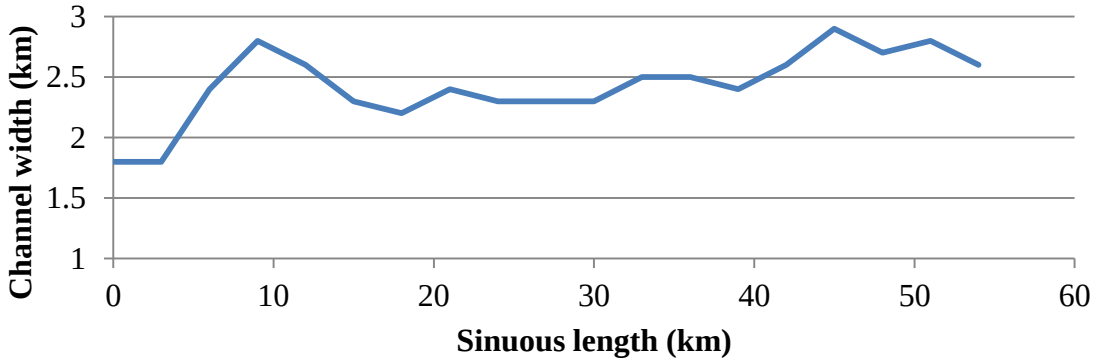

Figure 49: Graph showing width variations in the post-confluence section of Channel 3. Zero point is the confluence point.

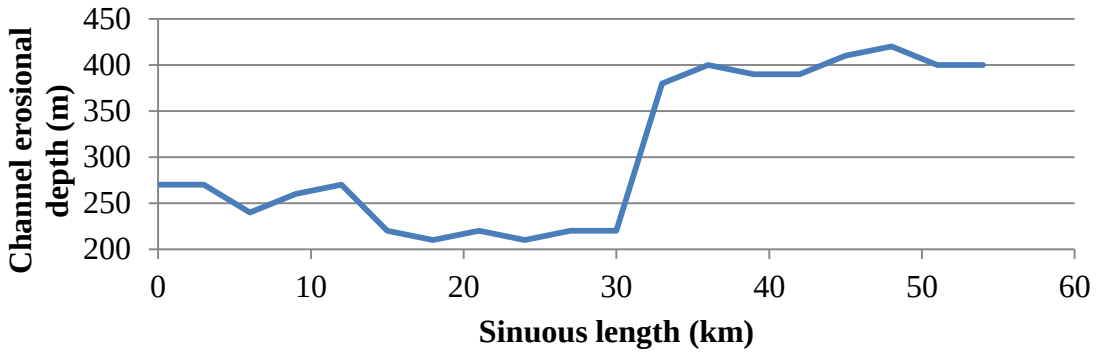

Figure 50: Graph showing erosional depth variations in the post-confluence section of Channel 3. Zero point is the confluence point.

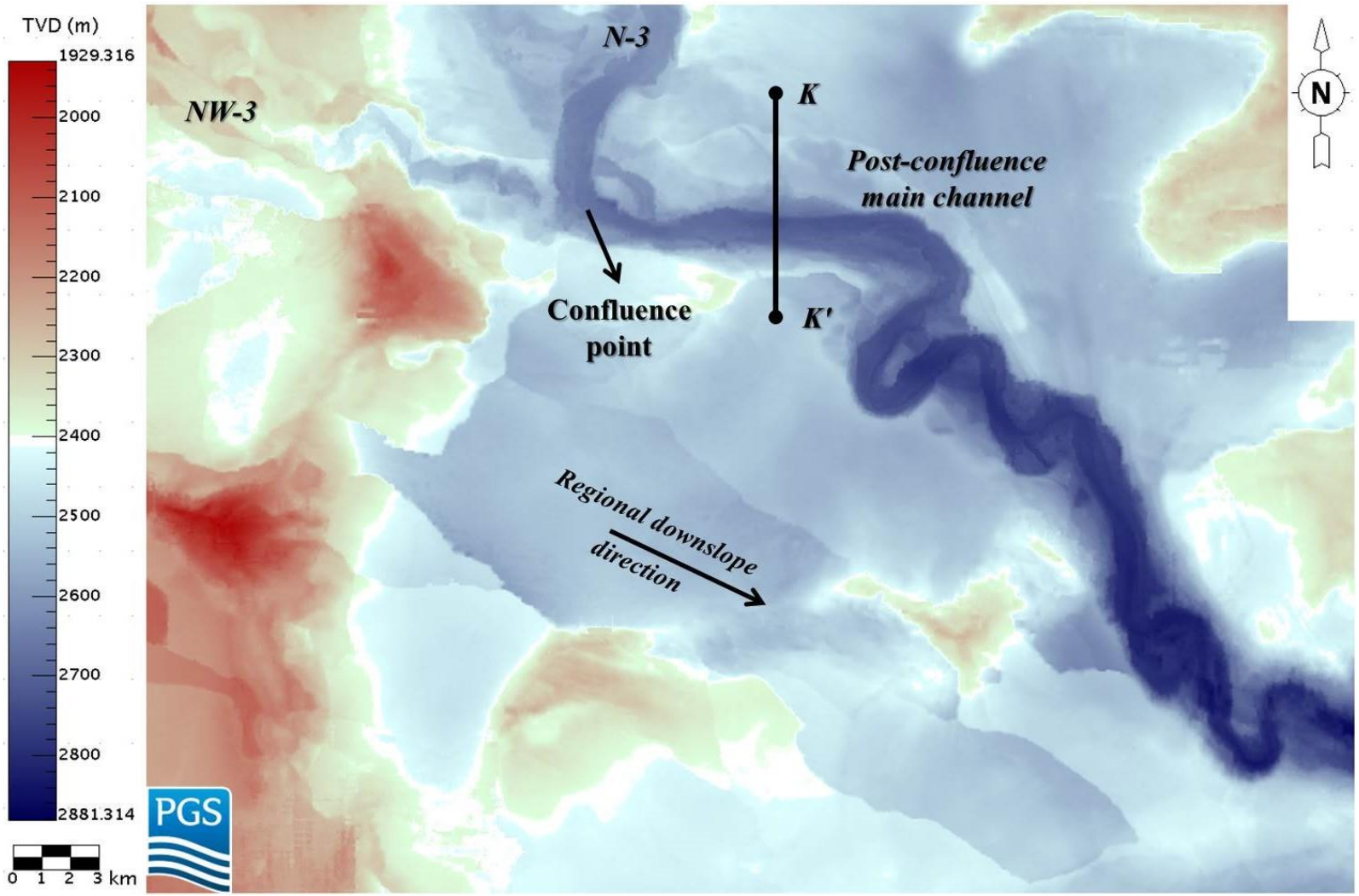

Figure 51: Structural map of the base of Channel 3. Map also shows the location of seismic cross section K-K′.

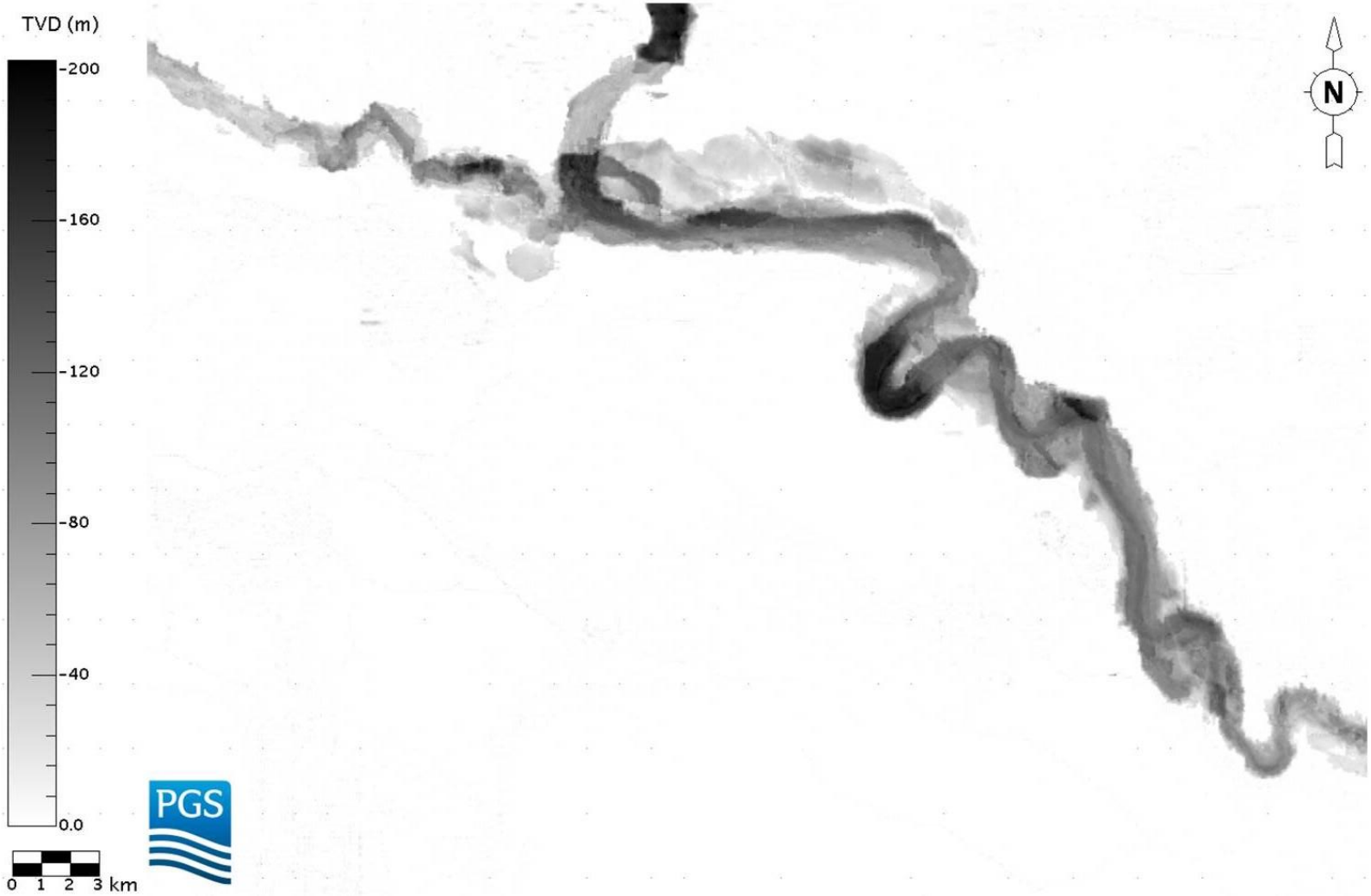

Figure 52: Isochore map of deposits filling Channel 3.

Mass Transport Complex 1

The base surface of Mass Transport Complex 1 (MTC-1) is shown in purple in seismic cross sections represented in this study (Figure 53). It entered the study area after the formation of Channel 3, and it was deposited at the northwestern part of the submarine channel system, between two tributaries of Channel 3. This unit eroded the western flank of the N-3 tributary and the northern flank of the NW-3 tributary of Channel 3. The thickness of MTC-1 reaches a maximum of 170 m within the study area, and it gradually decreases downslope (Figure 54).

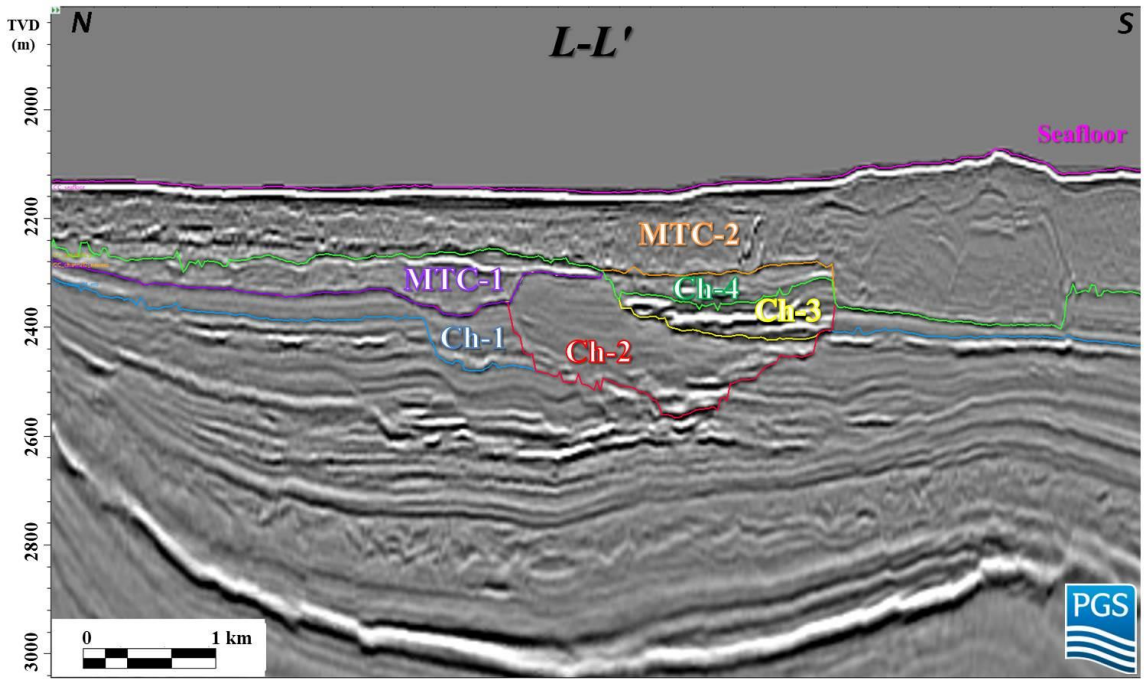

Figure 53: Seismic cross section L-L′ showing the relationship between Mass Transport Complex 1 and other individual units within the submarine channel system. Location of the cross section is shown in Figure 54.

Figure 54: Isochore map of Mass Transport Complex 1. Map also shows the location of seismic cross section L-L′.

Channel 4

Channel 4, the youngest channel within the submarine channel system, is shown in green in the seismic cross sections represented in this study (Figure 25). Unlike Channel 2 and Channel 3, seismic-reflection data show that Channel 4 does not have a northern tributary (Figure 59). This lack is probably a result of the complete erosion of the northern tributary of Channel 4, which should have been located above the N-2 and N-3 tributaries before being eroded by a younger mass transport complex. The channel entered the study area from the northwest within WB-2 and continued its pathway through the southeast for 18 km (Figure 59 & Figure 67), reaching a maximum erosional depth of 170 m (Figure 58). Within this part of the channel, it has an average width of 2.3 km (Figure 57), an average gradient of 11.7 m/km (Figure 56) and an average sinuosity of 1.11 (Figure 55). Then, the channel was diverted to the east to stay within WB-6 for 15 km (Figure 59 & Figure 67) as a straight channel (Figure 55). There are slight differences in channel parameters within this section, with a maximum incision depth of 160 m (Figure 58), an average width of 3.5 km (Figure 57) and an average gradient of 8.3 m/km (Figure 56). The channel changed its flow direction to the southeast again (Figure 59), with a dramatic increase in sinuosity, reaching to a value of 1.57 (Figure 55). In contrast, the channel displays sudden reduction in maximum erosional depth and channel gradient, where they decrease to values of 110 m and 2.4 m/km, respectively (Figure 56 & Figure 58). Within this part, the channel has an average width of 3.7 km (Figure 57). After the highly sinuous channel section, it followed the same transport direction for 9 km as a straight channel (Figure 55 & Figure 59), with an average width of 4 km and an average gradient of 1 m/km (Figure 56 & Figure 57). The channel passed through a depression between SD-6 and SD-8 (Figure 59 & Figure 67), and increased its maximum incision

depth to 290 m within this part (Figure 57). Channel 4 reaches the modern seafloor within this section (Figure 7). Then, the channel changed its flow direction to the east again to flow directly on the top of SD-9 (Figure 59 & Figure 67). The channel increased its sinuosity to 1.52 and its gradient to 5.3 m/km (Figure 55 & Figure 56). The channel has a maximum erosional depth of 310 m and an average width of 3.7 km within this section (Figure 57 & Figure 58).

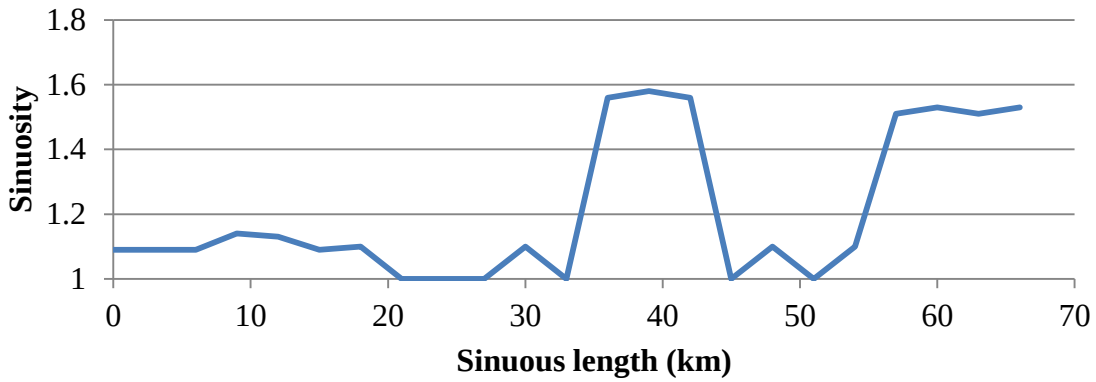

Figure 55: Graph showing sinuosity variations in Channel 4. Zero point is where the channel entered the study area.

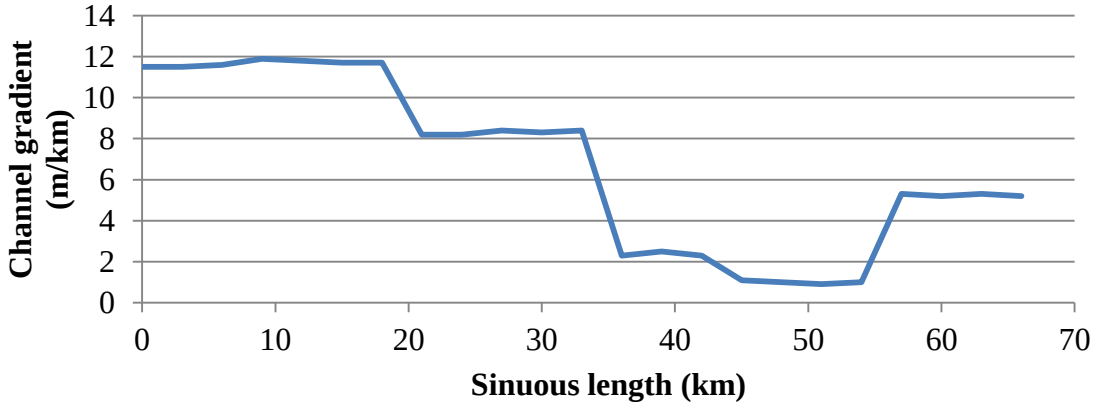

Figure 56: Graph showing gradient variations in Channel 4. Zero point is where the channel entered the study area.

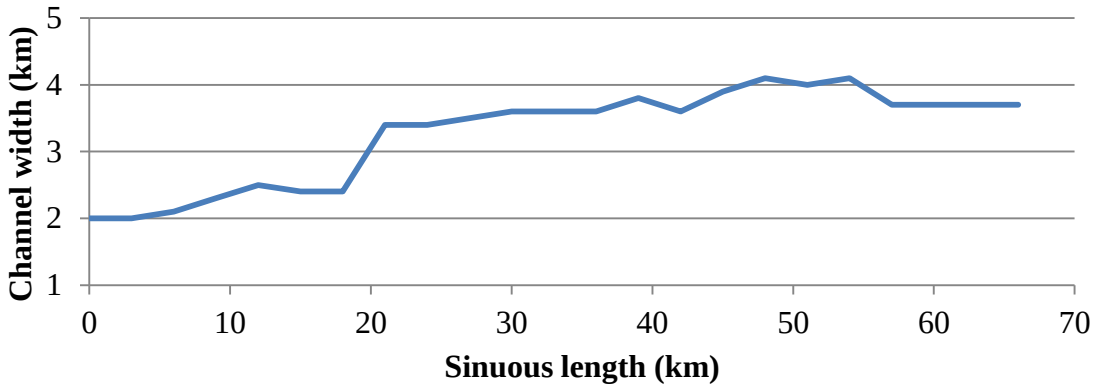

Figure 57: Graph showing width variations in Channel 4. Zero point is where the channel entered the study area.

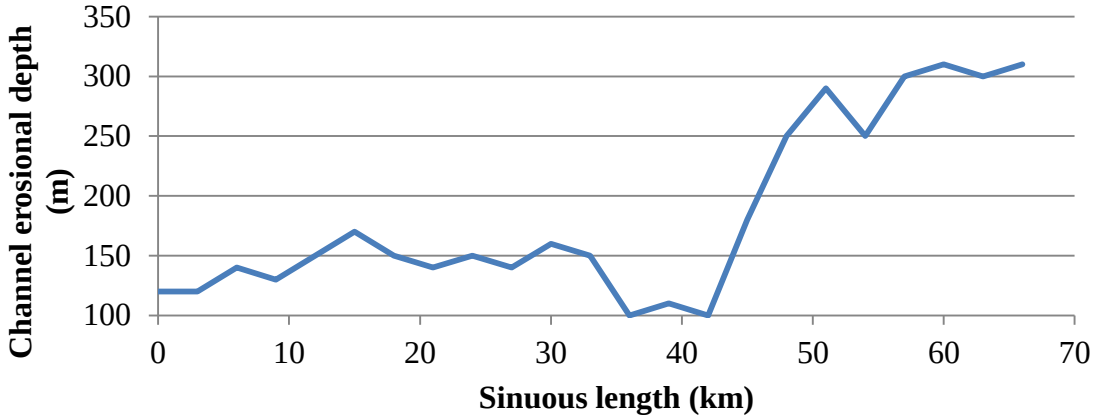

Figure 58: Graph showing erosional depth variations in Channel 4. Zero point is where the channel entered the study area.

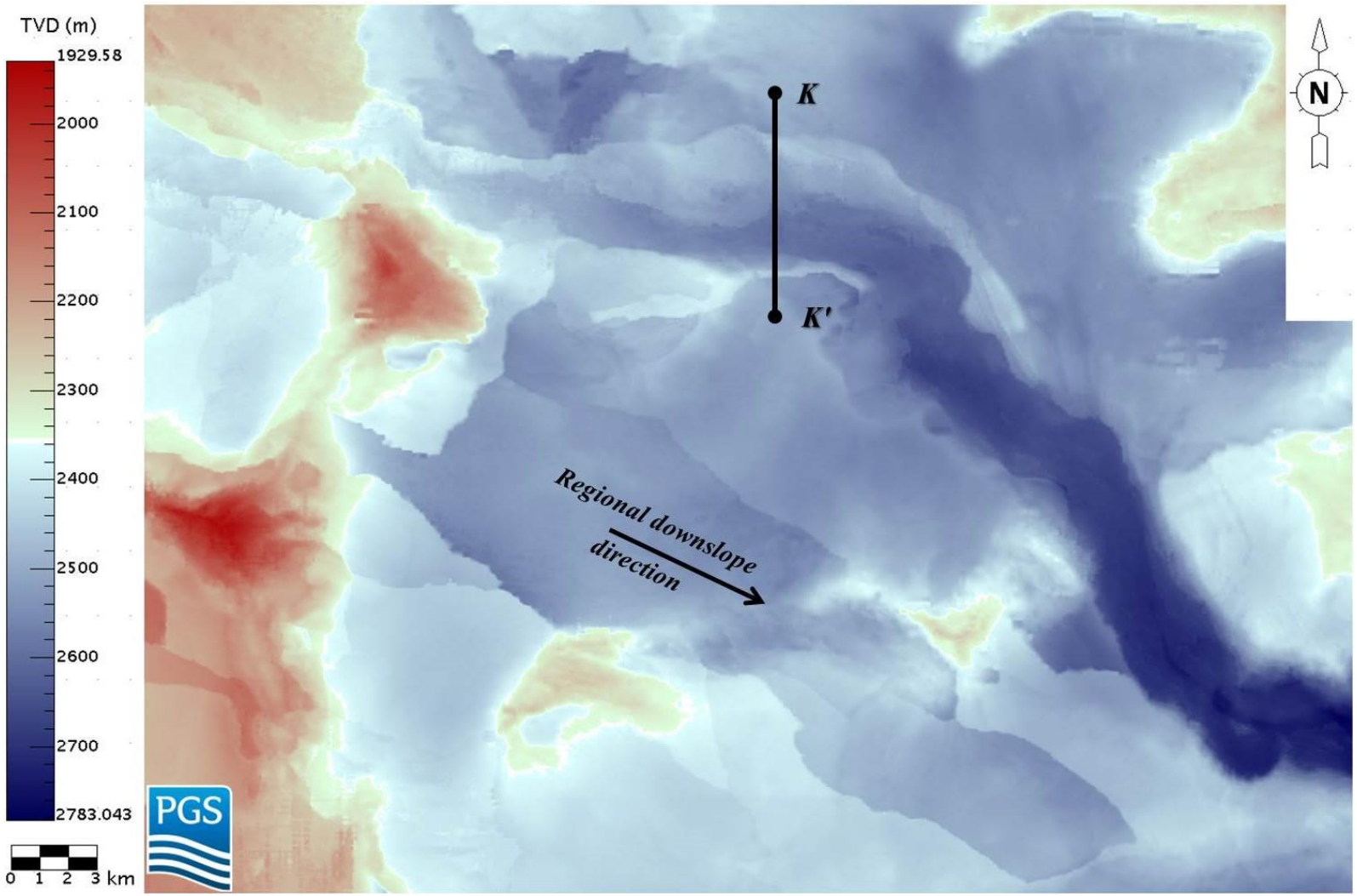

Figure 59: Structural map of the base of Channel 4. Map also shows the location of seismic cross section K-K′.

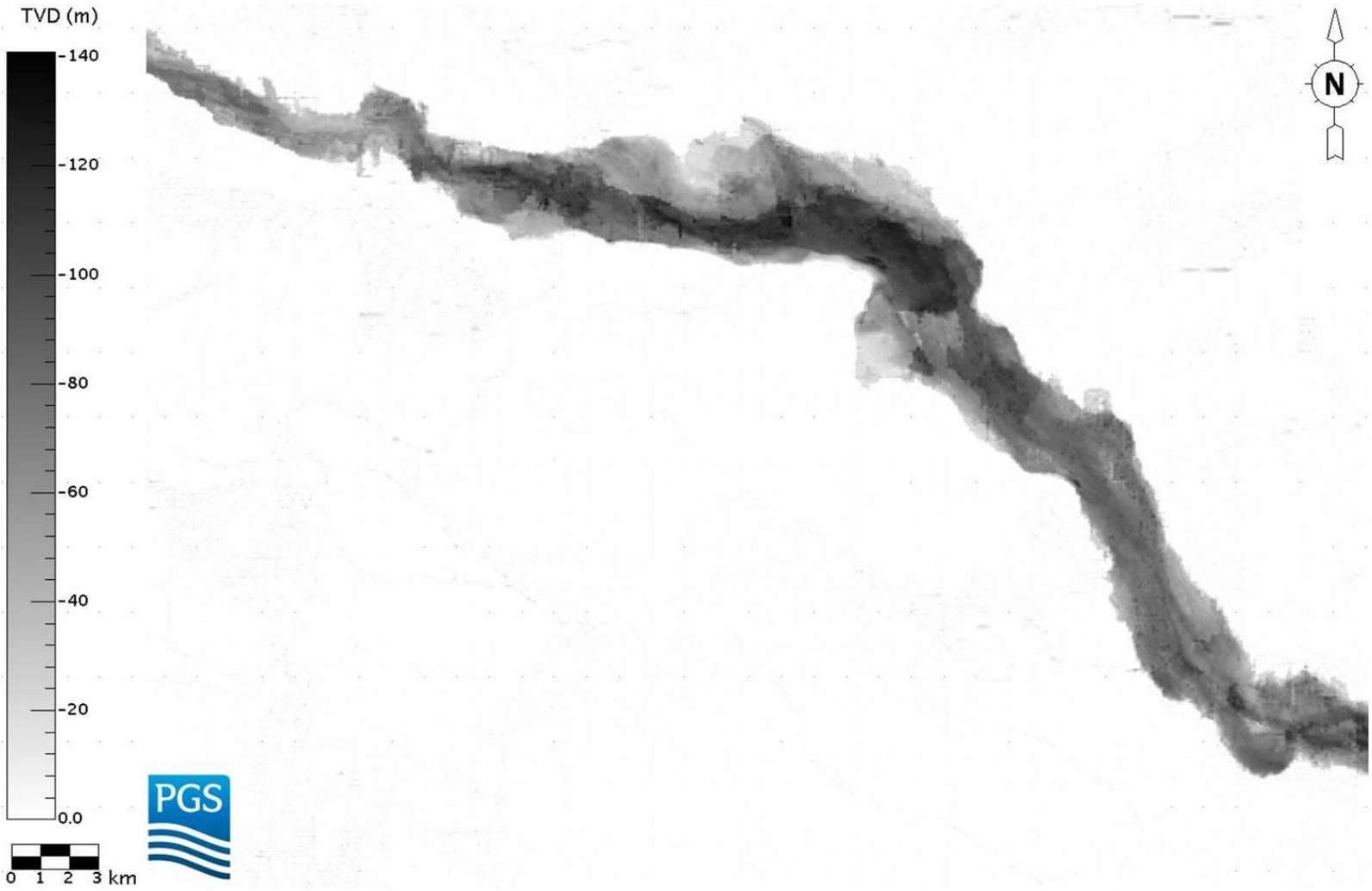

Figure 60: Isochore map of deposits filling Channel 4.

Mass Transport Complex 2

The base surface of Mass Transport Complex 2 (MTC-2) is shown in orange in seismic cross sections represented in this study (Figure 61). After the development of Channel 4, MTC-2 wiped out the entire study area, covered the whole submarine channel system pathway and reset the seafloor for a possible new phase of submarine channel evolution. It eroded both flanks of the westernmost section, and possibly the entire northern tributary of Channel 4. It is the youngest unit within the study area, and it mainly formed the shape of the modern seafloor. MTC-2 is significantly thick within salt-withdrawal basins, reaching a thickness of 390 m, and it becomes highly condensed or nearly absent on the top of salt-influenced structural highs (Figure 62).

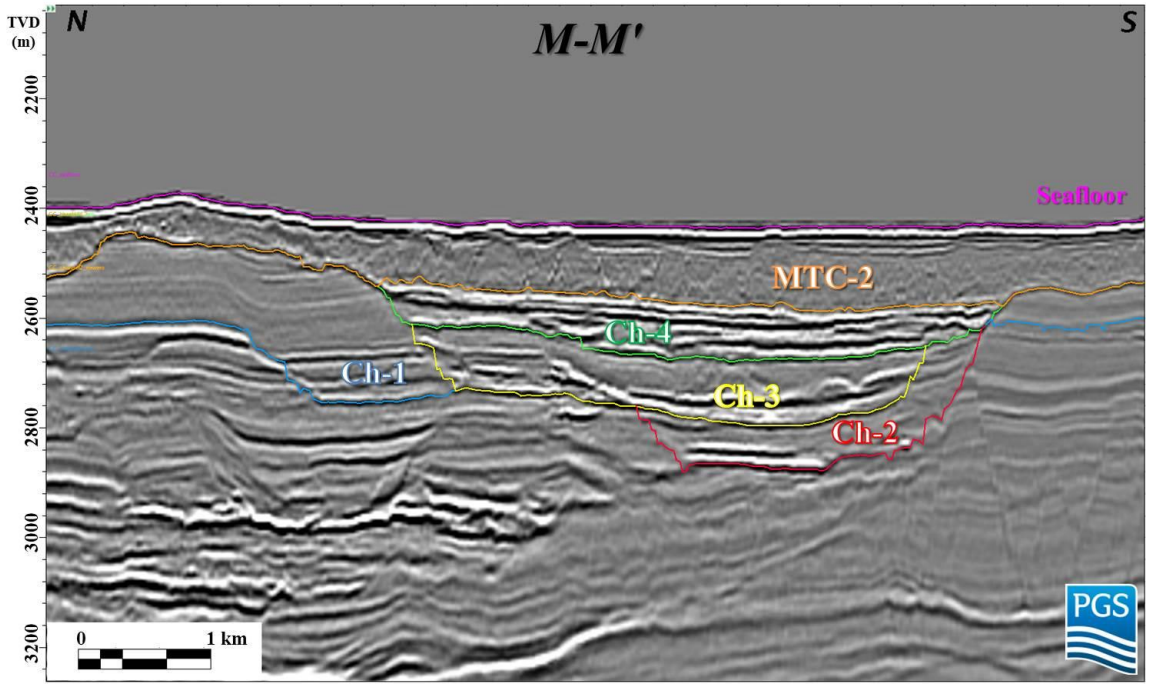

Figure 61: Seismic cross section M-M′ showing Mass Transport Complex 2 covering the entire submarine channel system. Location of the cross section is shown in Figure 62.

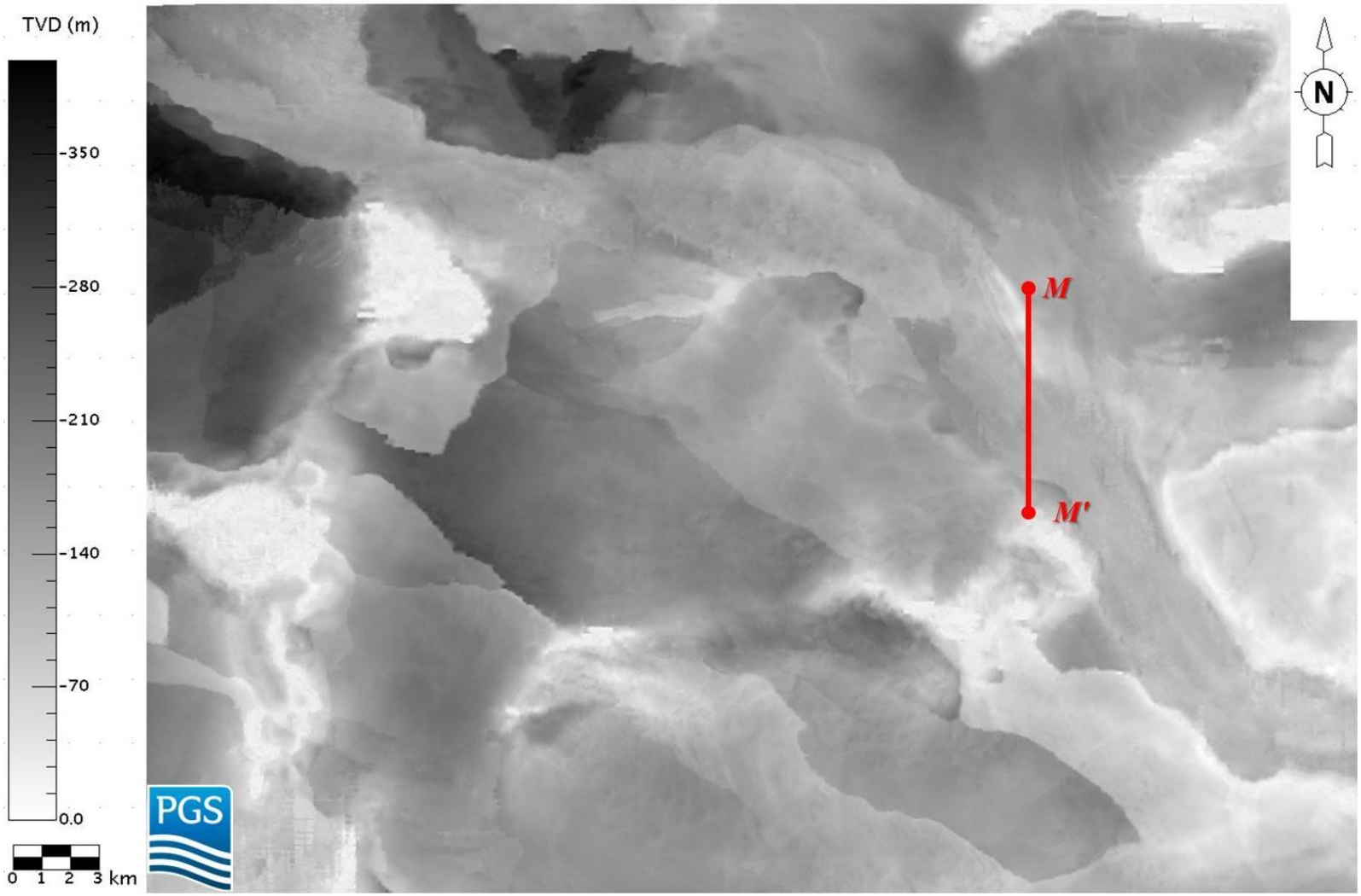

Figure 62: Isochore map of Mass Transport Complex 2. Map also shows the location of seismic cross section M-M′.

Structural Controls on Submarine Channel Development

The architecture of submarine channel systems is commonly complicated by the interaction between channel development and structures that shape the seafloor topography (Oluboyo et al., 2013). Structurally influenced topography, which predates channel development, can divert channels as they flow downslope (Mayall et al., 2010). Within basins that are rich in salt and sedimentation interaction, salt diapirism can complicate the bathymetric relief at the seafloor (Oluboyo et al., 2013). Salt-induced deformation affects the seafloor in the form of subsiding basins and bathymetric highs over salt diapirs (Oluboyo et al., 2013). Channels can be deflected by the seafloor expression of salt diapirism and may follow lows between bathymetric highs (Rowan & Weimer, 1998).

The transport pathway of the submarine channel system is mostly dictated by paleobathymetry. Channels within the system mainly avoided salt-influenced structural highs, and they converged into salt-withdrawal basins (Figures 64, 65, 66 and 67). The NW-3 tributary of Channel 3 and the northwestern section of Channel 4 made a clear deflection of approximately 1 km to the north to avoid the structural high associated with SD-3 (Figure 66 & Figure 67). Before reaching the confluence point, they maintained their flow direction to the southeast within WB-3 (Figure 66 & Figure 67). The N-2 and N-3 tributaries entered the study area from the north and continued their flow through WB-3, toward the confluence point (Figure 65 & Figure 66). The post-confluence channel system changed its flow direction to the east, and the system passed near the structural high associated with SD-5 (Figures 64, 65, 66 and 67). After reaching the central part of WB-6, the channel system was diverted to the southeast with increasing sinuosity, to stay within WB-6 and avoid the structural high associated with SD-7

(Figures 64, 65, 66 and 67). Then, the pathway of the system continued in the same direction with decreased sinuosity and exited WB-6, toward the small depression between SD-6 and SD-8 (Figures 64, 65, 66 and 67).

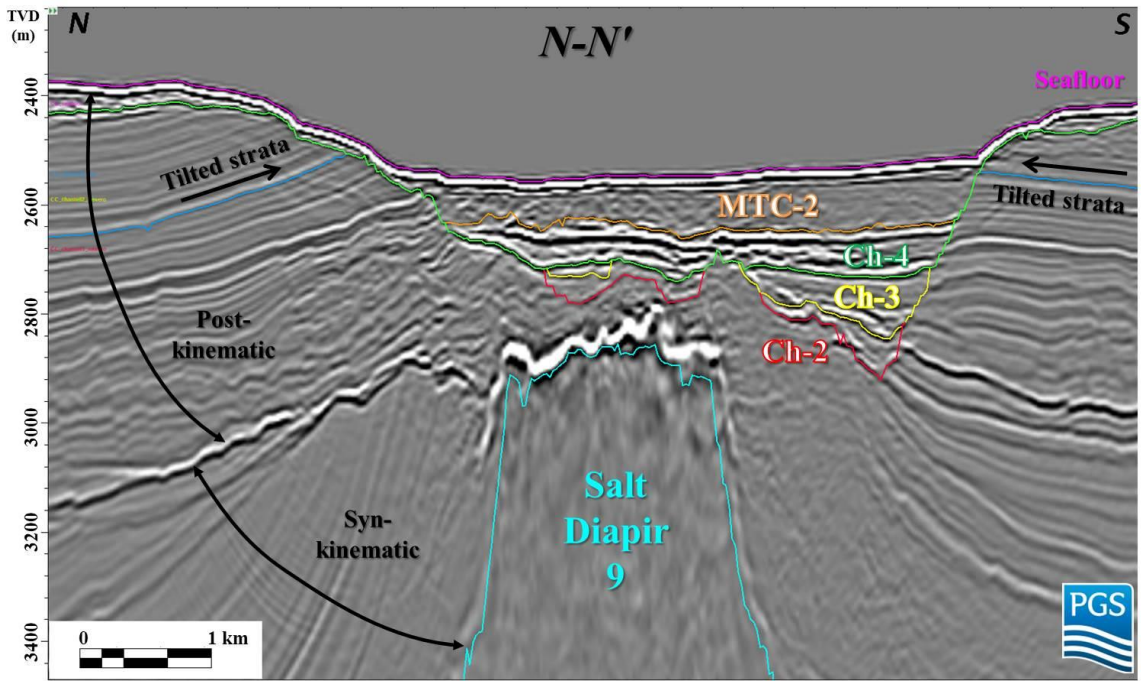

Figure 63: Seismic cross section N-N′ showing the timing relationship between the development of the submarine channel system and the growth of SD-9. Location of the cross section is shown in Figures 64, 65, 66 and 67.

After passing through a depression between SD-6 and SD-8, an anomaly appeared. The channel system was diverted to the east to flow directly on the top of SD-9, rather than staying within WB-7 or entering WB-8 (Figures 64, 65, 66 and 67). I explain this unexpected behavior by determining the timing of the growth of SD-9 relative to the development of the submarine channel system. SD-9 resulted in a paleobathymetric high within this area when the submarine channel system was formed, which indicates that SD-9 predates the development of the submarine channel system (Figure 14). However, the growth of SD-9 caused only a small amount of positive

paleobathymetric relief (~100 m) compared to other active salt diapirs. It was probably a result of aggradation within depressions next to the diapir that smoothed out much of the bathymetric expression associated with salt (Figure 14). This relatively small structural high on the paleobathymetry was unable to divert the submarine channel system (Figures 64, 65, 66 and 67).

I also investigated the architecture of nearby strata to determine the timing of the growth of SD-9. I interpret that the horizon that represents a stratigraphic surface approximately contemporaneous with the formation of the submarine channel system is within the post-kinematic strata (Figure 24). This indicates that SD-9 predates the formation of the submarine channel system. However, the time-equivalent strata with the submarine channel system are mainly tilted toward the salt diapir, and the basal surfaces of Channel 2 and Channel 3 are highly deformed (Figure 63). This deformation is most possibly due to the uplift of the salt diapir. This architecture suggests that another phase of salt movement started during the formation of the submarine channel system.

Deposits filling Channel 2 are mainly eroded by a subsequent younger channel (Figure 40), and there is a sudden decrease in the gradient of Channel 2 and Channel 3, even to a negative value for Channel 2 within the southeastern part of the study area (Figure 36 & Figure 48). These differences in channel parameters suggest that SD-9 was active again when Channel 2 started to form, as the architecture of these channels was affected by the growth of SD-9. However, the gradient of the youngest channel of the system (Channel 4) is increasing within this section (Figure 56). This suggests that the growth of SD-9 did not affect Channel 4, and SD-9 stopped growing before Channel 4 started to develop.

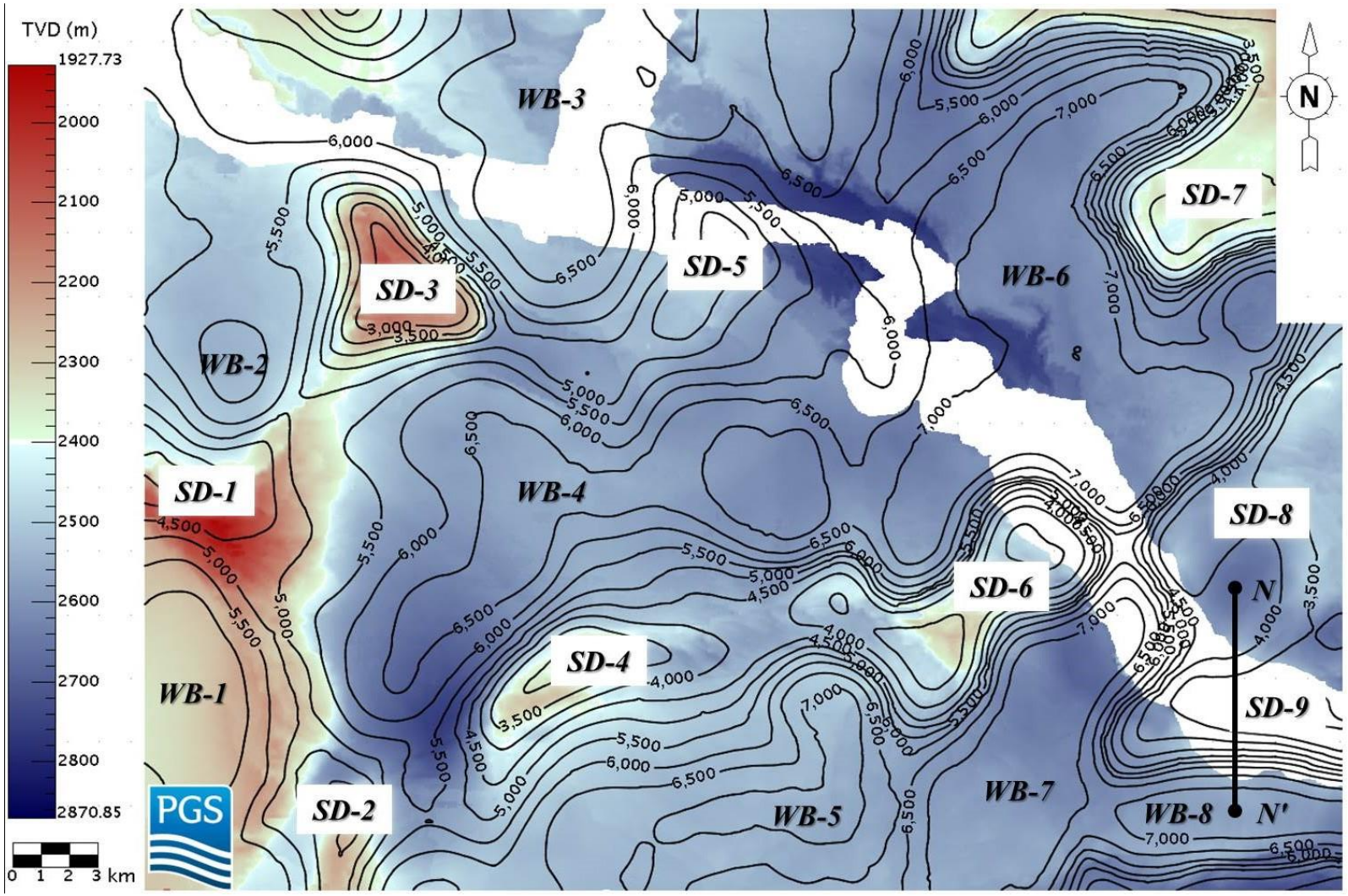

Figure 64: Structural map of the base of Channel 1 with contours of the top of salt unit. Map also shows the location of seismic cross section N-N′.

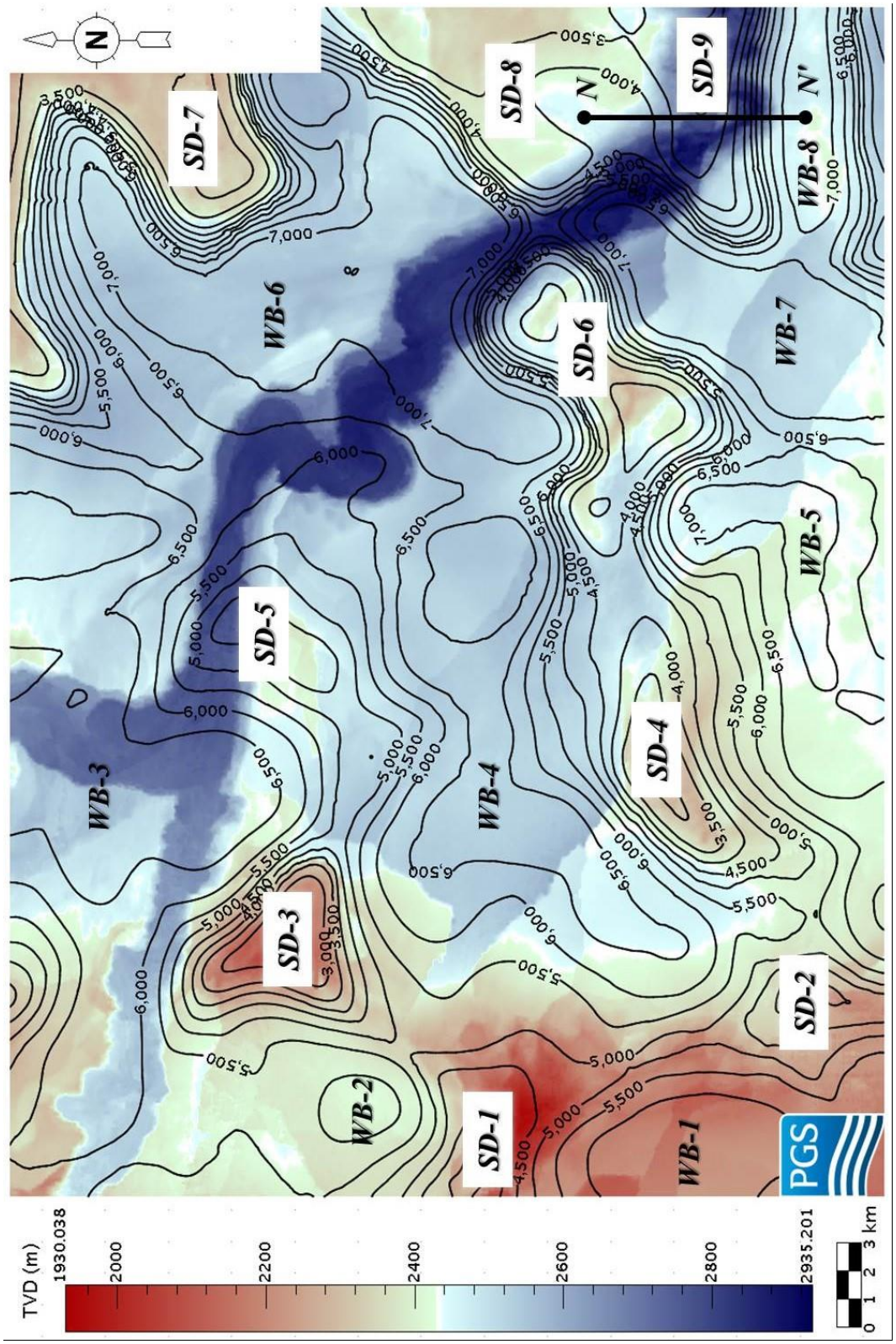

Figure 65: Structural map of the base of Channel 2 with contours of the top of salt unit. Map also shows the location of seismic cross section N-N'.

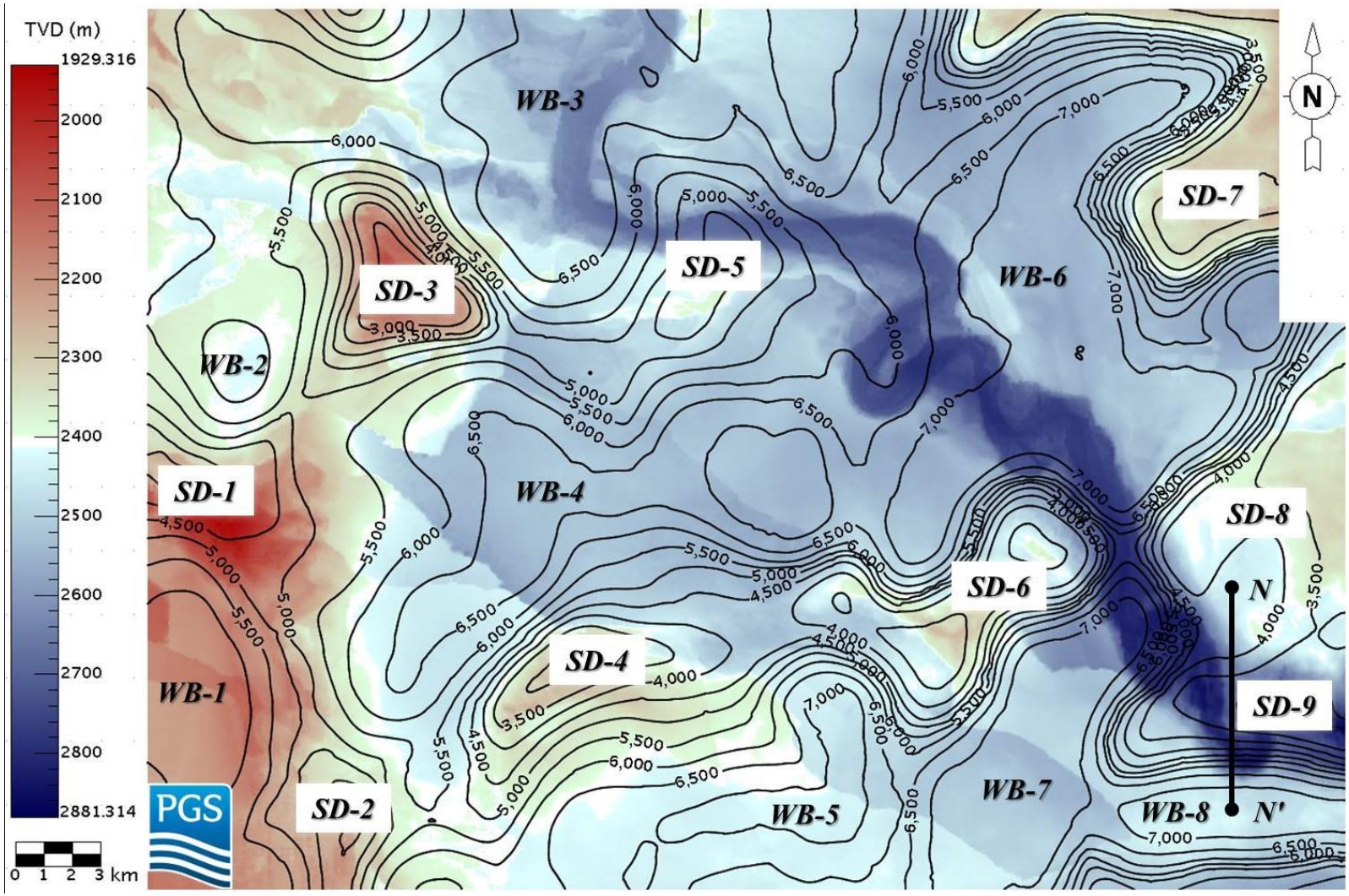

Figure 66: Structural map of the base of Channel 3 with contours of the top of salt unit. Map also shows the location of seismic cross section N-N′.

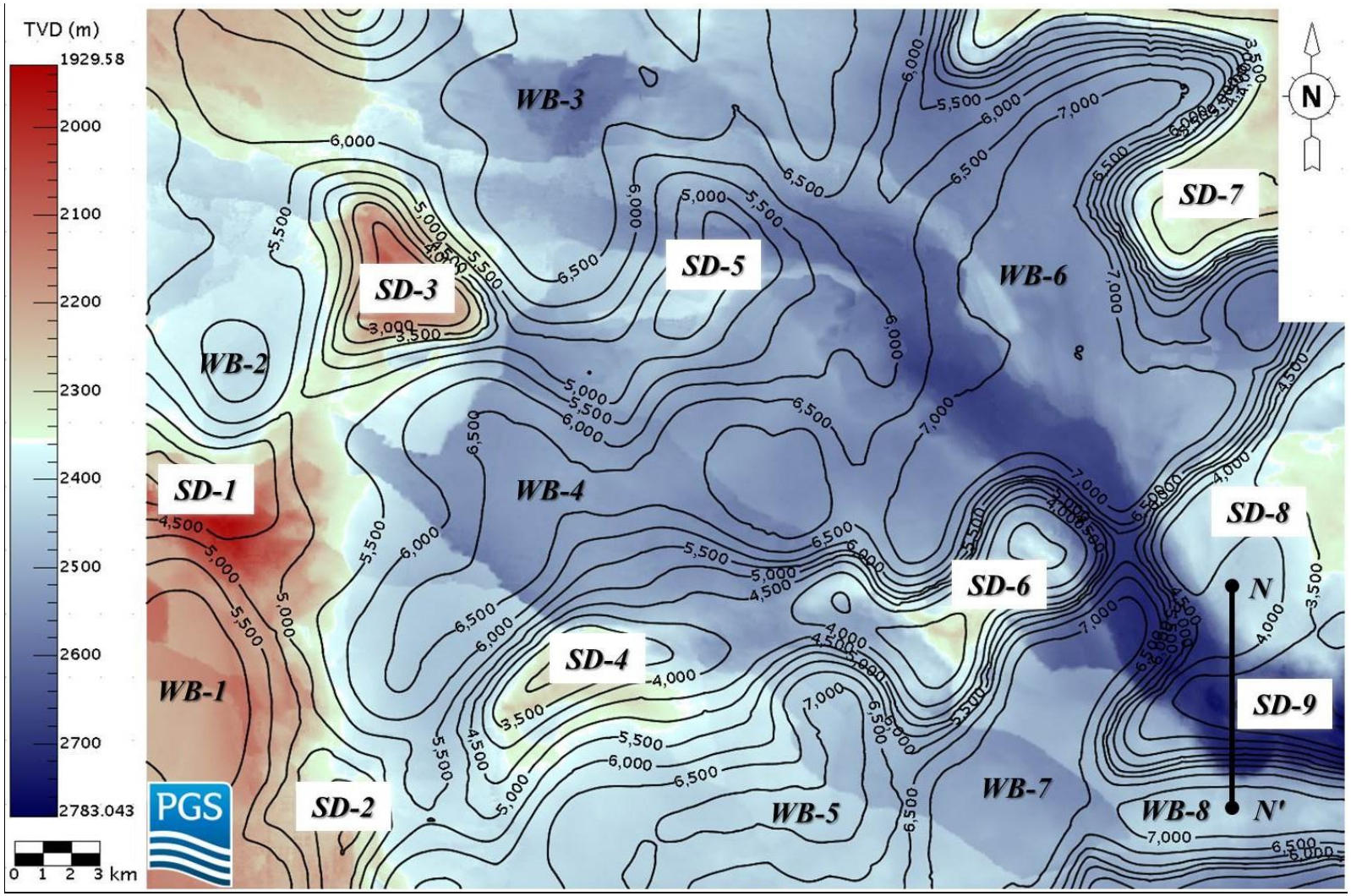

Figure 67: Structural map of the base of Channel 4 with contours of the top of salt unit. Map also shows the location of seismic cross section N-N′.

CHAPTER 4. SUMMARY AND CONCLUSIONS

The Campos Basin, located on the southeastern Brazil passive margin, is one of the most prolific basins in the South Atlantic (Mohriak et al., 1990). Sand-rich turbidite systems are the most productive reservoirs rocks within the basin (Bacoccoli & Toffoli, 1988). Submarine channels are one of the primary erosional and/or depositional elements within turbidite systems (Mutti & Normark, 1987, 1991; Normark et al., 1993; Piper & Normark, 2001). Understanding the controls on submarine channel evolution is crucial for establishing a model for the development of turbidite systems (e.g., Mayall et al., 2006).

Existing research about the development and evolution of submarine channels within the Campos Basin is focused on the controls of sediment supply, relative sea-level fluctuations and tectonic activity (e.g., Mohriak et al., 1990; Peres, 1993; Bruhn & Walker, 1995; Rangel et al., 2003; Fetter et al., 2009; Albertâo et al., 2011; De Gasperi & Catuneanu, 2014). Although there is extensive literature about the mechanisms controlling the development and evolution of submarine channel systems within the Campos Basin, few studies focus on the influence of salt-influenced structural deformation on submarine channel system evolution. The Campos Basin is structurally complex as a result of salt movement, and it is ideal setting in which to investigate the influences of structural deformation on channel evolution and architecture.

In this study, I interpreted the relationship between submarine channel development and structural deformation within the study area by focusing on a post-Miocene submarine channel system and investigating structural controls on each channel within the system. My study is entirely based on a 3D seismic-reflection volume, covering an area of approximately 1750 km^2 in the central part of the Campos Basin that

attains a depth of 9 km. The study area is within the translational domain and the middle slope portion of the basin, where both extensional and compressional salt-cored architectures can be observed.

I determined the structural configuration of the study area by mapping the top of the Aptian salt sequence, the modern seafloor and the horizon that I interpret to represent a stratigraphic surface approximately coeval with the formation of the submarine channel system. Salt movement controls the structural style of the study area by salt diapirism and by creating salt-withdrawal basins between these structural highs, as a result of the evacuation of deep salt. The entire study area is composed of nine salt diapirs (SD-1 to 9) and eight salt-withdrawal basins (WB-1 to 8) between these salt-influenced structural highs. I interpreted active and passive salt diapirs on the basis of whether the diapirs created a bathymetric relief. I also investigated the influence of salt structures on the architecture and the transport pathway of turbidite systems to determine the timing of salt diapirs. By using this approach, I demonstrated two uplift stages within the development of SD-9.

The development and evolution of the submarine channel system started after the Miocene, and the system reaches the modern seafloor in the southeastern section of the study area. From oldest to youngest, the system started with three consecutive channels. A mass transport complex entered the northwestern part of the study area. It was followed by the youngest channel within the system. Finally, another mass transport complex covered the entire submarine channel system and reset the seafloor. Paleobathymetry mainly dictated the transport pathway of the submarine channel system, as channels within the system mainly avoided salt-influenced structural highs, and stayed in salt-withdrawal basins. However, I observed an unexpected behavior within the southeastern part of the study area, as the submarine channel system was diverted to flow

directly on the top of SD-9. I interpreted the driving mechanism of this anomaly as consequent events of;

- SD-9 predates the development of the submarine channel system. However, the growth of this diapir caused only a relatively small amount of positive paleobathymetric relief, which was as a result of aggradation within depressions next to the diapir that smoothed out much of the bathymetric expression associated with salt. This relatively small structural high within the paleobathymetry was unable to divert the submarine channel system.
- Another phase of salt movement started during the formation of the submarine channel system, deforming the basal surfaces of channels.
- The youngest channel within the system (Channel 4) was not affected by the growth of this diapir, which suggests that the growth of SD-9 stopped when the youngest channel started to develop.

REFERENCES

Albertâo, G. A., T. Mulder, and R. Eschard, 2011, Impact of salt-related palaeotopography on the distribution of turbidite reservoirs: Evidence from well-seismic analyses and structural restorations in the Brazilian offshore. Marine and Petroleum Geology, v. 28, p. 1023–1046.

Anderson, J. E., J. Cartwright, S. J. Drysdall, and N. Vivian, 2000, Controls on turbidite sand deposition during gravity-driven extension of a passive margin: Examples from Miocene sediments in Block 4, Angola. Marine Petroleum Geology, v. 17, p. 1165–1203.

Bacoccoli, G., and L. C. Toffoli, 1988, Petrobras and Brazil's offshore exploration: 20 years-a review. 20th Annual Offshore Technology Conference (OTC 5668), no page numbers available.

Barros, M. C., 1980, Geologia e recursos petroliferos da Bacia de Campos. Anais do XXXI Congresso Brasileiro de Geologia, v. 1, p. 254–265.

Broucke, O., F. Temple, D. Rouby, C. Robin, S. Calassou, T. Nalpas, and F. Guillocheau, 2004, The role of deformation processes on the geometry of mud-dominated turbiditic systems, Oligocene and lower-middle Miocene of the lower Congo Basin (West African Margin). Marine Petroleum Geology, v. 21, p. 327–348.

Bruhn, C. H. L., and R. G. Walker, 1995, High-resolution stratigraphy and sedimentary evolution of coarse-grained canyon-filling turbidites from the upper-Cretaceous transgressive megasequence, Campos Basin, offshore Brazil. Journal of Sedimentary Research, v. 65, p. 426–442.

Bruhn, C. H. L., 1998, Deep-water reservoirs from the eastern Brazilian rift and passive margin basins. AAPG Course Notes 6, Part 2, p. 14–15.

Bruhn, C. H. L., J. A. T. Gomes, C. D. Lucchese Jr., and P. R. S. Johann, 2003, Campos Basin: Reservoir characterization and management-Historical overview and future challenges. 35th Annual Offshore Technology Conference (OTC 15220), p. 1–13.

Carminatti, M., and J. C. Scarton, 1991, Sequence stratigraphy of the Oligocene Turbidite Complex of the Campos Basin, offshore Brazil. Springer-Verlag, Berlin, p. 241–246.

Chang, H. K., R. O. Kowsmann, A. M. F. Figueiredo, and A. A. Bender, 1992, Tectonics and stratigraphy of the East Brazil rift system: an overview. Tectonophysics, v. 213, p. 97–138.

Clark, I. R., and J. Cartwright, 2009, Interactions between submarine channel systems and deformation in deepwater fold belts: Examples from the Levant Basin, Eastern Mediterranean sea. Marine Petroleum Geology, v. 26, p. 1465–1482.

Clark, I. R., and J. Cartwright, 2011, Key controls on submarine channel development in structurally active settings. Marine Petroleum Geology, v. 28, p. 1333–1349.

De Gasperi, A., and O. Catuneanu, 2014, Sequence stratigraphy of the Eocene turbidite reservoirs in Albacora field, Campos Basin, offshore Brazil. AAPG Bulletin, v. 98, p. 279–313.

Demercian, S., P. Szatmari, and P. R. Cobbold, 1993, Style and pattern of salt diapirs due to thin-skinned gravitational gliding, Campos and Santos basins, offshore Brazil. Tectonophysics, v. 228, p. 393–433.

Fetter, M., 2009, The role of basement tectonic reactivation on the structural evolution of Campos Basin, offshore Brazil: Evidence from 3D seismic analysis and section restoration. Marine and Petroleum Geology, v. 26, p. 873–886.

Gamboa, D., T. M. Alves, and J. Cartwright, 2012, A submarine channel confluence classification for topographically confined slopes. Marine Petroleum Geology, v. 35, p. 176–189.

Gee, M. J. R., and R. L. Gawthorpe, 2007, Early evolution of submarine channels offshore Angola revealed by three-dimensional seismic data. Geological Society of London, p. 223–235.

Guardado, L. R., L. A. P. Gamboa, and C. F. Lucchesi, 1990, Petroleum geology of the Campos Basin, Brazil: a model for producing Atlantic type basins. AAPG Memoir, v. 48, p. 3–80.

Guardado, L. R., A. R. Spadini, J. S. L. Brandâo, and M. R. Mello, 2000, Petroleum system of the Campos Basin. AAPG Memoir, v. 73, p. 317–324.

Hudec, M. R., and M. P. A. Jackson, 2007, Terra infirma: understanding salt tectonics. Earth-Science Reviews, v. 82, p. 1–28.

Huyghe, P., M. Foata, E. Deville, and G. Mascle, 2004, Channel profiles through the active thrust front of the southern Barbados prism. Geology, v. 32, p. 429–432.

Jackson, M. P. A., and C. J. Talbot, 1991, A glossary of salt tectonics. Bureau of Economic Geology. Geologic Circular 91–4, 44 p.

Jackson, M. P. A., and M. R. Hudec, 2017, Salt tectonics: principles and practice. Cambridge University Press, 498 p.

Mayall, M., E. Jones, and M. Casey, 2006, Turbidite channel reservoirs - key elements in facies prediction and effective development. Marine Petroleum Geology, v. 23, p. 821–841.

Mayall, M., L. Lonergan, A. Bowman, S. James, K. Mills, T. Primmer, D. Pope, L. Rogers, and R. Skeene, 2010, The response of turbidite slope channels to growth-induced seabed topography, AAPG Bulletin, v. 94, p. 1011–1030.

Middleton, G.V., and M. A. Hampton, 1973, Sediment gravity flows: Mechanics of flow and deposition. Los Angeles: Society of Economic Paleontologists and Mineralogists, p. 1–38.

Mohriak, W. U., M. R. Mello, J. F. Dewey, and J. R. Maxwell, 1990, Petroleum geology of the Campos Basin, offshore Brazil. Geological Society of London, Special Publication, v. 50, p. 119–141.

Mohriak, W. U., P. Szatmari, and S. Anjos, 2012, Salt: geology and tectonics of selected Brazilian basins in their global context. Geological Society of London, Special Publications, v. 363, p. 131–158.

Mutti, E., and W. R. Normark, 1987, Comparing examples of modern and ancient turbidite systems: problems and concepts. Marine Clastic Sedimentology, v. 1, p. 1–38.

Mutti, E., and W. R. Normark, 1991, An integrated approach to the study of turbidite systems. Springer, p. 75–106.

Normark, W. R., H. W. Posamentier, and E. Mutti, 1993, Turbidite systems: state of the art and future directions. Review of Geophysics, v. 31, p. 91–116.

Oluboyo, A. L., R. L. Gawthorpe, K. Bakke, and F. Hadler-Jacobsen, 2013, Salt tectonic controls on deep-water turbidite depositional systems: Miocene, southwestern lower Congo Basin, offshore Angola. Basin Research, v. 26, p. 592–620.

Palmigiani, F., 2017, Petrobras launches Campos Basin tender. Retrieved July 16, 2017, from http://www.upstreamonline.com/.

Peres, W. E., 1993, Shelf-fed turbidite system model and its application to the Oligocene deposits of the Campos Basin, Brazil. AAPG Bulletin, v. 77, p. 81–101.

Piper, D. J. W., and W. R. Normark, 2001, Sandy fans from Amazon to Hueneme and beyond. AAPG Bulletin, v. 85, p. 1407–1438.

Posamentier, H. W., and V. Kolla, 2003, Seismic geomorphology and stratigraphy of depositional elements in deep-water settings. Journal of Sedimentary Research, v. 73, p. 367–388.

Prather, B. F., 2003, Controls on reservoir distribution, architecture and stratigraphic trapping in slope settings. Marine Petroleum Geology, v. 20, p. 529–545.

Quirk, D. G., N. Schodt, B. Lassen, S. J. Ings, D. Hsu, K. K. Hirsch, and C. V. Nicolai, 2012, Salt tectonics on passive margins: examples from Santos, Campos and Kwanza basins. Geological Society of London, Special Publications, v. 363, p. 207–244.

Rangel, H. D., P. T. Guimarâes, and A. R. Spadini, 2003, Barracuda and Roncador giant oil fields, deep-water Campos Basin, Brazil. AAPG Memoir, v. 78, p. 123–137.

Rowan, M. G., and P. Weimer, 1998, Salt-sediment interaction, northern Green canyon and Ewing Bank (offshore Louisiana), northern Gulf of Mexico. AAPG Bulletin, v. 82, p. 1055–1082.

Rowan, M. G., and B. Vendeville, 2006, Foldbelts with early salt withdrawal and diapirism: Physical model and examples from the northern Gulf of Mexico and the Flinders Ranges, Australia. Marine Petroleum Geology, v. 23, p. 871–891.

Shipp, C., J. A. Nott, and J. A. Newlin, 2004, Physical characteristics and impact of mass transport complexes on deepwater jetted conductors and suction anchor piles. Offshore Technology Conference, Houston, TX, OTC Paper 16751, p. 11.

Sloss, L. L., 1964, Tectonic cycles of the North American Craton. Kansas Geological Survey, v. 169, p. 449–459.

Smith, R., 2004, Silled sub-basins to connected tortuous corridors: Sediment distribution systems on topographically complex sub-aqueous slopes. Geological Society of London, Special Publications, v. 222, p. 23–44.

Winker, C. D., and J. R. Booth, 2000, Sedimentary dynamics of the salt-dominated continental slope, Gulf of Mexico. SEPM 20th Annual Research Conference, p. 1059–1086.

Winter, W. R., R. J. Jahnert, and A. B. França, 2007, Bacia de Campos. Petrobras Geosciences Bulletin, v. 15, p. 511–529.